Manipulating Light with Metamaterials: Synchrotron Radiation from an Accelerating Light Pulse and On-Chip Devices

by

Meredith A. Henstridge

A dissertation submitted in partial fulfillment
of the requirements for the degree of
Doctor of Philosophy
(Applied Physics)
in the University of Michigan
2018

Doctoral Committee:

Professor Roberto D. Merlin, Chair
Professor Roy Clarke
Professor Anthony Grbic
Professor L. Jay Guo
Professor Jennifer Ogilvie
Professor Duncan G. Steel

Meredith A. Henstridge

mhenst@umich.edu

ORCID iD: 0000-0002-7561-0802

DEDICATION

For all of the people who have contributed to the remarkable silent film of memories that I often play in front of my eyes.

Mom and Dad, this is definitely for you. Thank you for your support.

For all of you whom I never truly got to know because time was not on our side – perhaps we can try again in the next lifetime. Be prepared; I am going to bring this with me for you to read.

ACKNOWLEDGMENTS

First, I sincerely thank my parents, Steve and Cecilia Henstridge for always pushing to provide none other than the best for their two children, which included access to the best high schools available in Cleveland, financial support and encouragement throughout my undergraduate education, constant cheerleading throughout graduate school, and always sending me back to Ann Arbor with at least a few days' worth of meals after visits to their home. These two people have truly lived for their children, and I am fortunate to be their daughter.

I would like to extend a bouquet of eternal gratitude to my advisor, Prof. Roberto Merlin. Roberto has showed me a profound amount of care throughout the years, which has included perpetual encouragement, kicks in the you-know-what when I needed it, and profound concern during times of trouble. Through both, his conception of clever projects and his guidance, Roberto provided me a remarkable toolbox for success, one that I gladly accepted, held dearly, and used extensively. None of the accomplishments presented in this work would have been possible without him. I only wish to have more time with him, whether in Ann Arbor or elsewhere. The relationship we have is one that I will treasure for the rest of my days.

Both, Prof. Steven Herbert and Prof. Heidrun Schmitzer from the Xavier University Physics Department saw within me the soul of a talented scientist and encouraged me accordingly, even throughout the times when I did not quite see such a thing in myself. Their constant mentoring and support throughout my college years has undoubtedly made my career as a physicist possible. The entire department: Dr. Steven Herbert, Dr. Heidrun Schmitzer, Marca Kasselmann, Amy

Bosch, Dr. Justin Link, Dr. Marco Fatuzzo, Dr. Stephen Yerian, Dr. Greg Braun, Jeff Stapleton, Dr. Terry Toepker, and *of course*, Dennis Tierney have all been family to me. Dennis prepares students for life, gives hell to any breathing entity that may deserve it, and will proudly and irreverently make the stodgy and the stuffy types uncomfortable. The world needs more people like Dennis.

My friends in Ann Arbor and Cincinnati have been like family to me, and their mere existence is a big part of what makes life worth living and science worth doing. Matthew Shergy, Sarah Bucher, Nora Tighe, Alex Ampleman, Fabiola Arce, Patrick Albaugh, and Chris Anderson are people with whom I was quite close throughout my college years, and I certainly did not visit them as much as I would have liked during my time in Ann Arbor. Labmates from the Merlin Lab, in particular, Prashant Padmanabhan, Alex Tolouse, and Ibrahim Boulares, and Steve Young have been brothers to me. Jessica Ames, who graduated from Prof. Ted Norris's lab and shared the OPA room with us, has been a remarkable friend, and I only wish I had spent more time with her. The same goes for Heather Ferguson, also of the Norris Lab and a fellow OPA room member. Heather likely witnessed the unpleasant conversations I often had with uncooperative optics in my setup. Heather, I regret that I was so grouchy at times, I can only strive to be as kind as you, and I wish we got to hang out more. Alex Sklyar, Dani Hochfellner, Christian Shively, and Lucas Joel have become particularly close friends with whom I often spent time in Ann Arbor, and they are certainly people with whom I will be friends for the rest of my days. During my last two semesters, I had the privilege of serving as a graduate student instructor alongside Prof. Dante Amidei, an experience which has undoubtedly changed me for the better and will leave me with another friend for life. As acknowledged later on in this work, Dr. Pilar Herrera-Fierro from the Lurie Nanofabrication Facility has also had a profoundly positive impact upon my life.

I would like to thank the members of my thesis committee: Prof. Roberto Merlin, Prof. Roy Clarke, Prof. Anthony Grbic, Prof. L. Jay Guo, Prof. Jennifer Ogilvie, and Prof. Duncan Steel for taking the time to review my thesis and participate in my oral defense.

All of this said, this is certainly not everyone who has made my time here a blessing. Not even close.

" What a beautiful face

I have found in this place

That is circling all 'round the sun

What a beautiful dream

That could flash on the screen

In a blink of an eye and be gone from me

Soft and sweet

Let me hold it close and keep it here with me

- Neutral Milk Hotel, *"In an Aeroplane Over the Sea"*

TABLE OF CONTENTS

LIST OF FIGURES

ABSTRACT

Metamaterial devices which manipulate light over length scales that are not achievable with conventional optics are investigated. First, a sub-wavelength-slotted waveguide, which exhibits *extraordinary transmission* at a frequency near each of its Fabry-Perot resonances, is considered. We use THz-time domain spectroscopy to measure the transmission of a broadband test pulse through a structure designed to exhibit resonances in the 1-2 THz range. We demonstrate that light is transmitted at only a few frequencies which are determined by the tunable separation of the slotted plates. The wavelength-size of the structure makes it a candidate for on-chip THz spectroscopy platforms, which can allow for new applications in areas such as microfluidics and remote sensing. Limitations arising from the requirement for strict plate alignment are discussed, and future work entails the achievement of near-perfect (< 0.1°) parallelization of the plates. The next problem pursued in this work concerns the acceleration of light over hundred micron length scales in materials. Conventional methods for generating such accelerating beams involve setups which require length scales of at least several centimeters. Furthermore, Snell's Law limits the ability of light incident from free space to bend at steep angles inside materials. For certain nonlinear crystals with high refractive indexes, it then becomes impossible to generate light beams that propagate along non-paraxial circular arcs. The use of metasurfaces to accelerate light eliminates all of these difficulties. We demonstrate the acceleration of light over length scales of one hundred microns inside a glass chip using metasurfaces consisting of plasmonic V-antennas. Future work involves the consideration of designs such as Huygens surfaces that would eliminate drawbacks associated with the V-antennas, but increase fabrication difficulty. This metasurface-approach is then used to accelerate a sub-picosecond light pulse over a hundred micron-scale circular arc inside a $LiTaO_3$ crystal. Through mixing with the second order nonlinear susceptibility, the accelerating pulse produces a nonlinear polarization which emits synchrotron radiation. We image the evolution of the difference-frequency component of the synchroton field, which is at THz frequencies. This demonstration of synchrotron radiation over a scale of 100 μm is the smallest to-date. Calculations of the radiated power spectrum for a circulating charge suggest that

synchrotron radiation produced from a continuously-revolving light pulse has implications for on-chip continuous-wave THz sources. One possible avenue for future work involves the use of whispering gallery resonators constructed from nonlinear crystals for the realization of monochromatic THz synchrotron radiation. Thus, each of the metamaterial devices presented in this thesis allow for both, the observation of physics that is interesting in its own right and the possibility of applications which benefit the broader scientific community.

CHAPTER 1
INTRODUCTION

"Thanne longen folk to goon on pilgrimages,

And palmeres for to seken straunge strondes,

To ferne halwes, kowthe in sondry londes;

And specially from every shires ende

Of engelond to caunterbury they wende"

- Geoffrey Chaucer, "*Canterbury Tales"*

My doctoral studies have consisted of four projects, three of which I will discuss in detail throughout this dissertation.

The very first project on which I worked was led by Prashant Padmanabhan, who was my senior in the Merlin Lab. We studied the excitation of acoustic plasmon (AP) modes that were confined within optically thin slabs of GaAs. APs have been known for a long time to exist in photoexcited bulk GaAs [1], but the confined AP modes we observed had yet to be reported. We studied the coherent excitation of these modes using impulsive stimulated Raman scattering (ISRS) experiments, and our work was reported in [2]. In addition, we saw evidence of confined acoustic plasmons in spontaneous Raman scattering measurements. I built the Raman setup used to perform these measurements, which also entailed revamping an old continuous-wave dye laser that was likely on its way to property disposition. This laser was tuned to the $E_0 + \Delta_0$ bandgap

and was then used to photoexcite an electron-hole plasma in the GaAs sample. The spontaneous Raman scattering data we obtained, which shows evidence of confined AP modes, has yet to be published. I won't be discussing these results in this thesis; nevertheless, working on this project was vital for my development as a researcher.

All three of the projects discussed in this thesis concern the use of metamaterials to manipulate light over length scales that are not possible with conventional optics systems consisting of components such as lenses, mirrors, polarizers, and waveplates. In addition to the unique physics exhibited by these metamaterial devices, they have profound applications for the on-chip manipulation of light. Specifically, I will present demonstrations of an on-chip THz spectrometer, a metasurface which accelerates light over hundred-micron scales inside a glass chip, and the generation of synchrotron radiation over a one hundred micron length scale. In the remainder of this chapter, I will present the need for such devices and summarize the advantages they have to offer.

1.1. The Demand for On-Chip THz Spectrometers

Terahertz (THz) imaging and spectroscopy provide a wealth of information to researchers from a wide range of disciplines. Filling the gap between the microwave and infrared range, THz radiation has shown to be extremely useful to probe molecular dynamics [3,4,5], distinguish between cancerous and benign tissue [6,7], and for the identification of contraband concealed within packages and clothing that are opaque at visible frequencies [8,9]. Efforts have also focused on the collection of extraterrestrial far-infrared and THz emissions, the analysis of which provides information regarding planetary atmospheres, the life cycle of interstellar clouds, and other phenomena of interest to astronomers and cosmologists [10,11,12].

One of the oldest and best-known methods for measuring THz spectra is Fourier Transform Infrared (FTIR) Spectroscopy, in which radiation is spectrally resolved with the use of, say, a Michelson interferometer [13]. A more modern technique, Terahertz Time Domain Spectroscopy (THz-TDS), is a coherent method sensitive to the electric field. In most THz-TDS setups, the emission and detection processes rely on an ultrafast laser to excite either a photoconductive antenna [14,15,16] nonlinear crystal [17,18] or air plasma [19,20]. Another coherent THz method involves tuning the frequency of a continuous-wave source and detecting the field transmitted or reflected from a sample [21,22]. THz applications are often limited by the relatively large size of the available systems. However, a highly compact THz spectrometer can allow for applications such as on-chip spectroscopy for integration with microfluidics platforms [23,24], and can easily be incorporated into any given optical setup to quickly characterize a THz source. Also, integrating a chip-sized THz spectrometer with a remotely-controlled device could allow for fast remote characterization of hazardous environments through the spectral fingerprinting of substances such as toxic gasses [25,26] and air-borne weapons [27].

1.2. An On-Chip THz Spectrometer based on Extraordinary Transmission

The sub-wavelength slotted waveguide structure considered in Chapter 3 is shown through both, experiment and theory, to exhibit long-lived resonances with tunable frequencies in the THz part of the spectrum. These resonances belong to a certain class known to give enhanced transmission through ordinarily weakly-transmitting sub-wavelength apertures, or rather, *extraordinary transmission*. Using terahertz time-domain spectroscopy, we show that the few frequencies of the THz pulse transmitted by the slotted plates are determined by the separation of the slotted plates. The wavelength of the first order resonance is almost exactly

twice the plate separation, as dictated by the Fabry-Perot Condition. Thus, the tunable, long-lived resonances of this wavelength-sized structure make it a suitable candidate for on-chip THz-spectroscopy systems.

1.3. New Opportunities by Accelerating Light With Metasurfaces

Non-diffracting solutions to Maxwell's equations other than plane waves, such as Bessel [28,29] and Mathieu [30] beams, which propagate indefinitely along linear trajectories without transverse distortions, have been known for a long time. There is a lesser-known and particularly unique group of diffraction-free solutions for which the intensity maximum follows a curved trajectory. In contrast to beams that accelerate due to refractive index gradients, such as those that form mirages [31] or those inside a gradient-index (GRIN) system [32], these solutions to Maxwell's equations propagate along curved trajectories in vacuum. Applications of accelerating beams to microparticle manipulation [33,34], micromachining [35], optical circuits [36] and nonlinear optics [37-42] have been reported. In addition, the concept of accelerating waves has been extended to surface plasmon polaritons [43-48].

Current methods for generating accelerating solutions to Maxwell's equations require setups consisting of a spatial light modulator and lenses. The bulkiness of these setups requires spaces of several centimeters in order to bend light at steep angles, eliminating the possibility of using highly-curved beams for on-chip applications. Furthermore, Snell's Law limits the bending of light from free space to an angle of $\theta_{max} = \sin^{-1}(1/n)$ inside a material of index *n*. As illustrated in Chapter 4, the generation of beams with substantially curved trajectories requires the ability to bend light at angles of at least ~ 45°. For a typical glass substrate with n = 1.45, $\theta_{max} =$ 44°, and it reduces to 41° if an optic with numerical aperture of 0.95 is used to focus the light

inside the glass. Using metasurfaces to accelerate light eliminates both of these difficulties associated with free-space-based setups and thus open new opportunities for the use of non-paraxial accelerating beams in applications such as optical circuits and lab-on-a-chip devices. This is first demonstrated in Chapter 4, in which we use metasurfaces consisting of plasmonic V-antennas to accelerate light over a scale of 100 μm inside a glass chip. This was the first step toward the introduction of non-paraxial accelerating light beams to the realm of nonlinear optics.

1.4. Synchrotron Radiation from a Metasurface-Produced Accelerating Light Pulse

$LiTaO_3$, a crystal which exhibits a large second-order nonlinear susceptibility for incident light polarized parallel to its optic axis, has a refractive index of 2.16 for wavelengths of 800 nm [49]. This corresponds to $\theta_{max} = 28°$. GaP and ZnTe, nonlinear crystals that have been used extensively for the difference frequency generation of THz radiation, have refractive indexes of respectively 3.18 [49] and ~ 2.9 [49] at 800 nm. This corresponds to, respectively, $\theta_{max} = 18°$ and $\theta_{max} = 20°$. Thus, the inability of free-space setups to bend light at steep angles in such nonlinear crystals severely limits the application of accelerating beams to nonlinear optics.

We use a metasurface to accelerate a sub-picosecond light pulse over the scale of 100 μm inside a $LiTaO_3$ crystal. Through mixing with the second order nonlinear susceptibility, the accelerating light pulse generates a nonlinear polarization which emits *synchrotron radiation*; details are discussed in Chapter 5. This is the first demonstration of synchrotron radiation from an accelerating nonlinear polarization, and the 100 μm scale over which this radiation is produced is the smallest to date. This work involved the design and execution of a spatially-resolved orthogonal pump-probe experiment in order to obtain images of the difference frequency component of the synchrotron field, which is at THz frequencies. Calculations which predict the

spectrum of the radiated synchrotron power for a continuously circulating charge suggest that the ability to continuously propagate a light pulse along a closed circular trajectory has profound implications for on-chip continuous wave THz sources.

CHAPTER 2
EXPERIMENTAL METHODS

"The highway is for gamblers, you better use your sense,

Take what you have gathered from coincidence"

- Bob Dylan, *"It's All Over Now, Baby Blue"*

2.1. Introduction to Pump-Probe Methods

A sufficiently short laser pulse has the ability to coherently excite modes in certain materials. These excitations lead to a time-dependent change in the refractive index, which can be determined by using a second *probe* pulse as a stroboscope. When the probe pulse arrives at a time t_d after the arrival of the *pump* pulse, it experiences the change in refractive index at time t_d and a concomitant change in intensity ΔI. By measuring the change in probe intensity ΔI at each delay step, a trace of the excitation amplitude can be obtained. Figure 2.1(a) illustrates the idea.

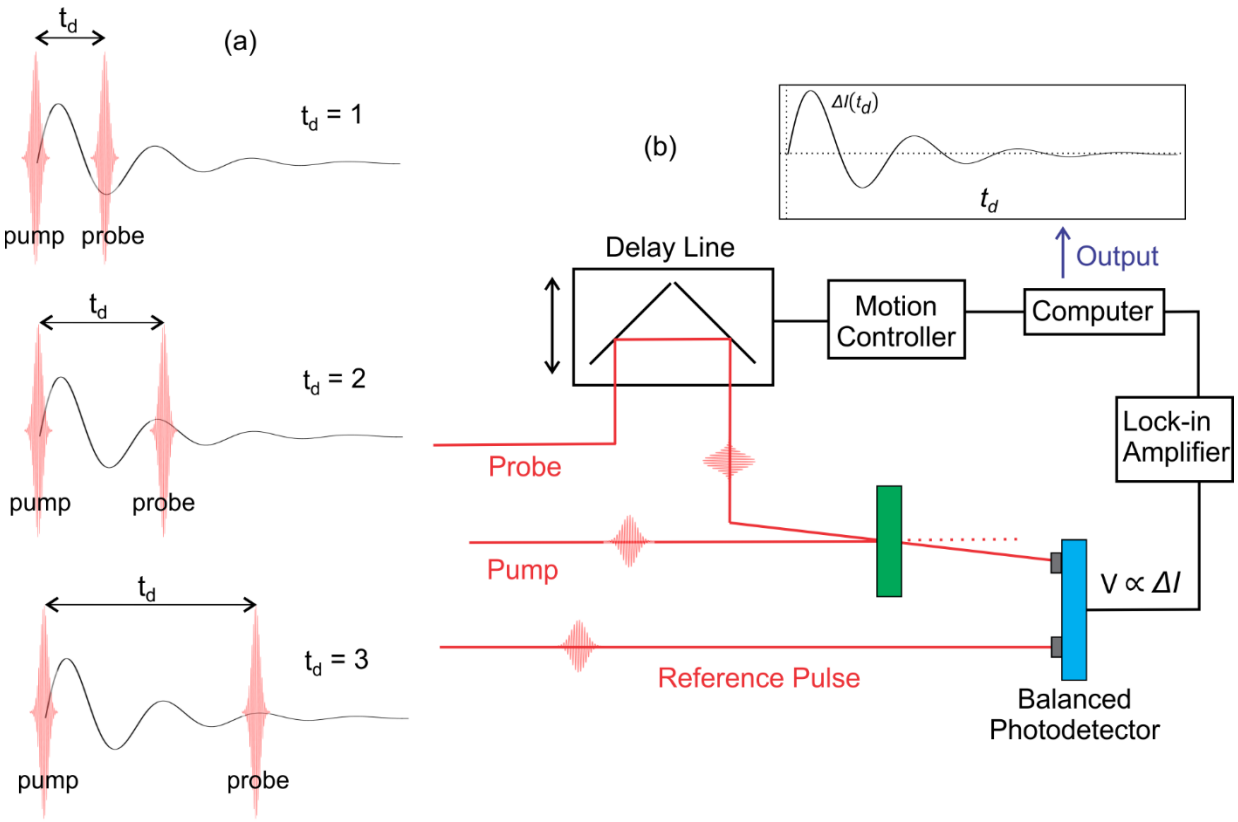

Figure 2.1. Illustration and general schematic of a pump-probe measurement. (a) An excitation resulting from the arrival of the pump pulse creates a time-dependent change in the refractive index of the material. The instantaneous change in refractive index at a given time t_d, relative to the start of the excitation, can be determined by measuring the change in intensity ΔI of a probe pulse. Sampling ΔI for several values of t_d results in a trace of the time-dependent amplitude of the excitation. (b) The general setup required to carry out pump-probe measurements. The intensity of the pump beam is modulated to allow for lock-in detection of the weak ΔI signal. A computer-controlled program automates the scanning of the delay line in steps of t_d and the subsequent writing of the lock-in amplifier output to file.

The changes in the probe transmission (or reflection) are typically quite small, in the range of 10^{-7} to 10^{-4}. Thus, it is important to reduce the noise in the measurement as much as possible. One of the primary noise culprits is the ultrafast laser used in the experiment. Generally speaking, intensity fluctuations can result from beam-pointing jitter, vibrating cavity optics, mode-locking instabilities, fluctuations in the pump laser, temperature gradients, elusive dust particles, and likely a myriad of other sources. Balanced detection schemes (discussed in detail in the later sections), which involve subtracting the intensity of the probe beam transmitted through the sample from

that of a reference beam, are typically good methods for cancelling out laser noise, as fluctuations in the average intensity will be present in both beam paths. It is important to make sure that the optical path from the laser to the sample is entirely unobstructed (i.e. there is no clipping of the beam on an aperture or the edge of a variable attenuator, etc.). Otherwise, the combination of beam pointing jitter from the laser and jitter from the optic itself will increase the noise floor considerably.

Lock-in detection is a vital method for isolating weak signals buried in the noise floor. The basic idea is that we modulate the signal of interest at a given frequency and analyze it with an amplifier that has the ability to detect signals within a very narrow bandwidth about the modulation frequency. This filters out noise sources present at other frequencies.

By modulating the pump intensity with a reference frequency ω_r, the pump-induced changes in the differential probe intensity ΔI will also be modulated at ω_r. For simplicity, let's assume this modulation is of the form $\sin(\omega_r t + \phi_r)$, although in many cases, the modulation is of the form of a square wave. When a voltage signal proportional to the differential probe intensity is input into the lock-in amplifier, a component inside the lock-in called a phase sensitive detector (PSD) multiples the input signal by a sine wave of frequency ω_L and phase ϕ_L that is produced by the lock-in amplifier's internal function generator. The resulting signal, denoted as V_X is:

$$V_X \propto \frac{1}{2}\cos((\omega_L - \omega_r)t + \phi_L - \phi_R) - \frac{1}{2}\cos((\omega_L + \omega_r)t + \phi_L + \phi_R) \quad (2.1)$$

Now, if we sync the lock-in's function generator to that of the reference frequency so that $\omega_r = \omega_L$, then the signal becomes:

$$V_X \propto \frac{1}{2}\cos(\phi_L - \phi_R) - \frac{1}{2}\cos(2\omega_r t + \phi_L + \phi_R) \quad (2.2)$$

The output of the PSD is then sent through a low pass filtering stage. The final signal is then:

$$V_X \propto \frac{1}{2}\cos(\phi_L - \phi_R) \quad (2.3)$$

The signal input into the lock-in is also sent to a second PSD which multiplies the input by a signal proportional to $\sin(\omega_L t + \phi_L + \pi/2)$. After low-pass filtering, the output from the second PSD is:

$$V_Y \propto \frac{1}{2}\sin(\phi_L - \phi_R) \quad (2.4)$$

For the SR830 digital lock-in used in all pump-probe experiments, we often use the "auto-phase" feature which adjusts ϕ_L so that all of the signal is measured in the X channel. However, there could be other signals present in the data that may not necessarily have the same phase as the reference frequency. Thus, a careful measurement involves recording the output from both X and Y channels.

Of course, a real lock-in amplifier cannot detect a signal at a single discrete frequency; the detection is carried out over a small bandwidth which is determined by the low pass filtering stages. The bandwidth of the low pass filters is determined by the inverse of the time constant *T* of the amplifier. Namely, the -3dB frequency of the filter is given by $f_{3dB} = 1/(2\pi T)$. The time constant can also be thought of in terms of averaging – a longer time constant results in averaging the input signal for a longer period of time. It's important to note that when the input to the lock-in amplifier is changed (which happens when we change the arrival time of the probe pulse), it takes approximately 5 time constants for the analyzed output signal to stabilize.

The pump-probe measurements conducted in this thesis use a mechanical delay line to vary the path length of the probe pulse and thus control its arrival time at the sample. The delay line consists of a retroreflector attached to a motor-controlled stage that can be displaced in increments of 1 μm. The positioning of the stage is determined by an electronic motion controller, which can

be remotely operated from a computer. A Labview program automates the process of scanning the delay stage, reading the output of the lock-in amplifier, and storing the data to file for each delay step. Figure 2.1(b) illustrates the general form of a pump-probe setup.

2.2. THz Time Domain Spectroscopy (THz-TDS)

2.2.1 Introduction

THz time domain spectroscopy (THz-TDS) involves the generation of THz-frequency radiation and its subsequent use for characterization of a sample, typically through transmission or reflection measurements. Several methods exist for the generation and detection of THz fields. Earlier methods for generation involve the use of a mode-locked Ti:Sapphire oscillator to excite a photoconductive antenna [15,50] or produce difference-frequency radiation inside a nonlinear crystal [51,52]. The advent of amplified Ti:Sapphire oscillators that produce pulses with mJ energies has allowed for both, generation and detection of ultra-broadband THz radiation using laser filamentation [19]. Electro-optic sampling, which involves focusing the THz field inside a nonlinear crystal and measuring the resulting change in refractive index with a visible or near-IR probe field, is frequently used for detection in THz-TDS.

I will present some theoretical details concerning the generation of THz radiation using a photoconductive emitter and its subsequent detection via electro-optic sampling, as these are the methods used in my experiments.

2.2.2 THz Generation with a Photoconductive Emitter

Here, we will focus on understanding the basic mechanism behind the emission of THz radiation from an optically-switched photoconductive emitter. Let's take an ultrafast laser pulse to

be incident upon a gap between a DC-biased pair of electrodes that lie upon a semiconductor substrate. An illustration is shown in Figure 2.2

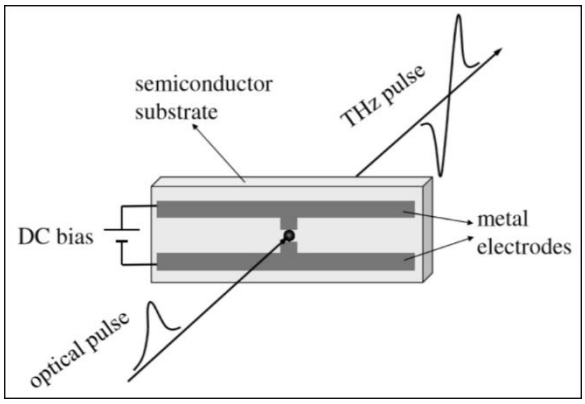

Figure 2.2. Schematic taken from [53] showing the excitation of a photoconductive emitter that contains a single dipole antenna. An incident laser pulse is focused tightly between two electrodes separated by a gap of dimensions w_0 ~ 5 – 10 μm. The resulting carrier density is accelerated by the bias field, producing THz radiation.

The pulse, which has an energy above the semiconductor bandgap, creates a carrier density in the gap between the electrodes which then accelerates due to the bias field E_{dc}. The resulting photocurrent $I_{pc}(t)$ is a convolution of the optical pulse intensity $I_{opt}(t)$ with the impulse response of the photocurrent [53]:

$$I_{pc}(t) = \int I_{opt}(t - t') \times qn(t')v(t')dt' \quad (2.5)$$

where q is the electron charge and

$$n(t) = e^{-t/\tau_c}\,;\ (t > 0) \quad (2.6)$$

is the carrier density which results from impulsive excitation by the optical pulse, and τ_c is the carrier lifetime. Also:

$$v(t) = \frac{q\tau_s}{m} E_{dc}\left[1 - e^{-t/\tau_s}\right]\,;\ (t > 0) \quad (2.7)$$

is the average electron velocity as determined by the electron mobility τ_s and the electron mass *m*. The gap length w_0 (~ 5 – 10 μm) is much smaller than the wavelength near 1 THz (λ ~ 300 μm), so we can model the antenna as an ideal dipole. Given that we are only concerned with the radiation in the far field, we can write the expression for the emitted THz field as [53]:

$$\boldsymbol{E}_{THz}(t) = \frac{\mu_0}{4\pi}\frac{\sin(\theta)}{r}\frac{d}{dt_r}\Big(I_{pc}(t_r)\Big)\widehat{\boldsymbol{\theta}} \quad (2.8)$$

Thus, $\boldsymbol{E}_{THz}(t)$ is proportional to the time-derivative of the photocurrent $I_{pc}(t)$, which is determined by both, the duration of the optical pulse and the intrinsic material properties of the semiconductor, namely τ_s and τ_c. If we assume that the intensity envelope of the incident optical pulse is of the form:

$$I_{opt}(t) = e^{-(t/\tau_p)^2} \quad (2.9)$$

then evaluating eq. (2.5) gives us:

$$I_{pc}(t) \propto \exp\left[\left(\frac{\tau_p}{2\tau_c}\right)^2 - \frac{t}{\tau_c}\right] \times \operatorname{erfc}\left[\frac{\tau_p}{2\tau_c} - \frac{t}{\tau_p}\right]$$

$$- \exp\left[\left(\frac{\tau_p}{2\tau_{cs}}\right)^2 - \frac{t}{\tau_{cs}}\right] \times \operatorname{erfc}\left[\frac{\tau_p}{2\tau_{cs}} - \frac{t}{\tau_p}\right] \quad (2.10)$$

where $1/\tau_{cs} = 1/\tau_c + 1/\tau_s$ and $\operatorname{erfc}(x) = 1 - \frac{2}{\sqrt{\pi}}\int_x^\infty e^{-y^2}dy$. Figure 2.3 shows plots of $I_{pc}(t)$ and the corresponding THz field for typical parameters $\tau_c = 0.5$ ps and τ_s = 0.03 ps taken from [53], for two different optical pulse widths.

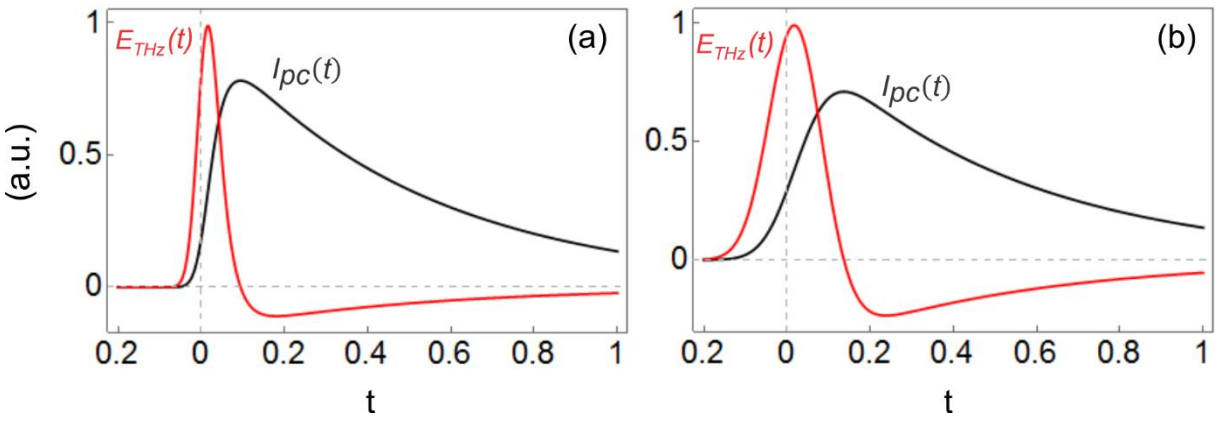

Figure 2.3. Evaluation of eq. (2.5) for (a) τ_p = 0.03 ps and (b) τ_p = 0.085 ps. $\boldsymbol{E}_{THz}(t)$ was found by taking the time-derivative of eq. (2.5). The material parameters used for both plots are τ_c = 0.5 ps and τ_s = 0.03 ps, taken from [53].

The photoconductive emitter used in this work was a Tera-SED3 emitter from Laser Quantum which was designed to be excited with the output of a Ti:Sapphire oscillator of repetition rate ~ 80 MHz. Schematics of the emitter are shown in Figure 2.3. Here, the emitter consists of interdigitated electrode fingers of spacing ~ 10 μm, which form an array of several excitable gaps [15]. Each individual gap functions based on the principle described in the previous paragraph. Optimal sizes of the illuminating beam spot are on the order of the wavelength of the radiated THz field (~ 100 μm – 300 μm) [54]. As shown in Figure 2.4, alternating gaps between electrodes are filled with an insulator followed by a metallization layer [15,54]. This forces each gap to emit a THz field of the same phase, allowing for constructive interference in the far-field. The interdigitated electrode design allows for both, a large photo-excited area and a large bias field across each individual gap. As a result, the radiated THz power is considerably greater than that from a single photoconductive dipole antenna.

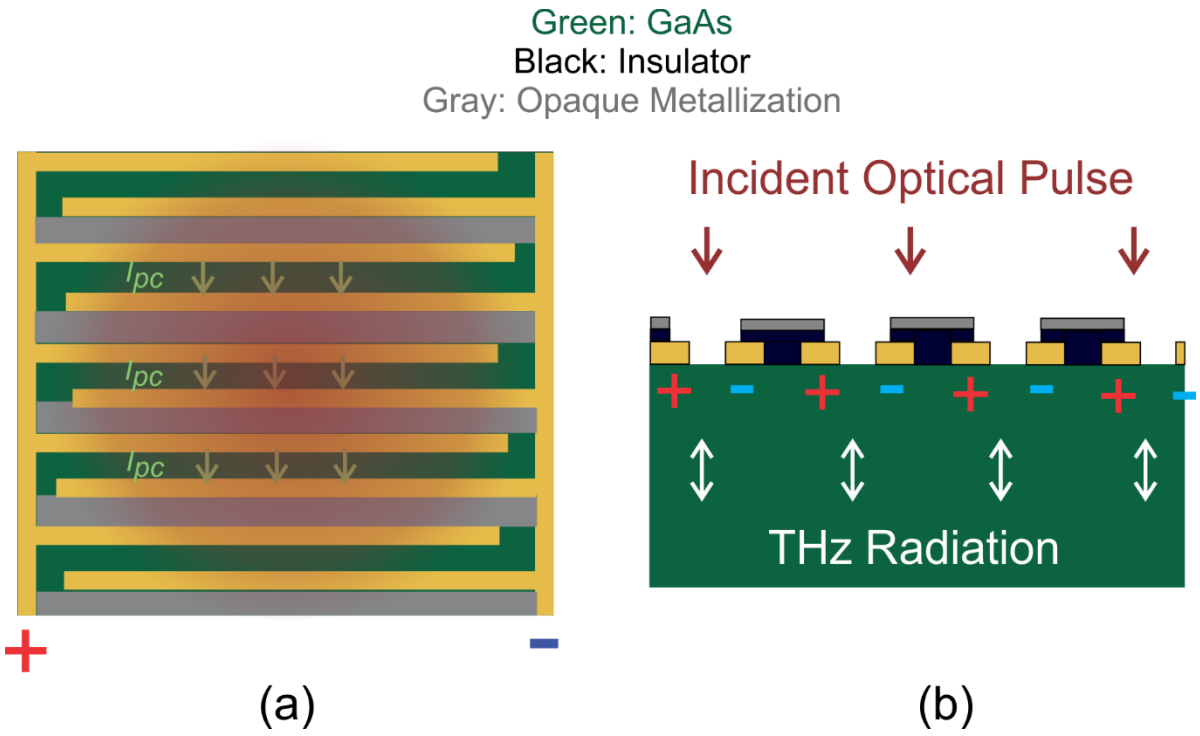

Figure 2.4. Schematics describing the geometry and excitation of the TeraSED3 emitter. (a) Top-down view. (b) Side-view. THz radiation is emitted into both, the air and GaAs half-spaces.

2.2.3 Electro-Optic Sampling

2.2.3.1 Derivation of Selection Rules for a $\bar{4}$3m crystal

The THz field transmitted or reflected from a sample can be detected by spatially overlapping it with a visible or near-IR probe field, and then focusing the two beams together inside a crystal with a second order nonlinear susceptibility. The presence of the THz field alters the crystal's permittivity tensor, and the probe field will experience a corresponding change in polarization if it has the correct orientation. In this section, we will derive the selection rules for electro-optic sampling using a $\bar{4}$3m (zincblende) crystal. We will find that for the correct crystal orientation and incident polarizations, the measured change in the probe polarization is proportional to the THz field amplitude experienced by the probe at a given delay, t_d.

Implementing these selection rules with the pump-probe technique presented in Figure 2.1, we can thus measure a trace of the THz field.

We start by writing the equation for the optical indicatrix, or the ellipsoid that defines the refractive index *n* for a given material [55]:

$$\left(\frac{1}{n^2}\right)_{xx} x^2 + \left(\frac{1}{n^2}\right)_{yy} y^2 + \left(\frac{1}{n^2}\right)_{zz} z^2 + 2\left(\frac{1}{n^2}\right)_{yz} yz + 2\left(\frac{1}{n^2}\right)_{xz} xz + 2\left(\frac{1}{n^2}\right)_{xy} xy = 1 \quad (2.11)$$

where $\eta_{ij} = \left(\frac{1}{n^2}\right)_{ij}$ is the second-rank impermeability tensor. For the linear electro-optic effect, η_{ij} is defined as:

$$\eta_{ij} = {\eta_{ij}}^{(0)} + \sum_k r_{ijk} E_k \quad (2.12)$$

where E_k is the k^{th} component of the applied THz field, ${\eta_{ij}}^{(0)}$ is the impermeability tensor in the absence of the applied field, and r_{ijk} is the third-rank electro-optic tensor. We can take $h = ij$ and express r_{ijk} as a two-dimensional matrix r_{hk}. Using this notation, we write:

$$\begin{array}{cc} h & ij \\ 1 & 11 = xx \\ 2 & 22 = yy \\ 3 = & 33 = zz \\ 4 & 13,31 = xz, zx \\ 5 & 23,32 = yz, zy \\ 6 & 12,21 = xy, yx \end{array} \quad (2.13)$$

The impermeability then can be written as:

$$\begin{bmatrix} \left(\frac{1}{n^2}\right)_1 \\ \left(\frac{1}{n^2}\right)_2 \\ \left(\frac{1}{n^2}\right)_3 \\ \left(\frac{1}{n^2}\right)_4 \\ \left(\frac{1}{n^2}\right)_5 \\ \left(\frac{1}{n^2}\right)_6 \end{bmatrix} = \begin{bmatrix} r_{11} & r_{12} & r_{13} \\ r_{21} & r_{22} & r_{23} \\ r_{31} & r_{32} & r_{33} \\ r_{41} & r_{42} & r_{43} \\ r_{51} & r_{52} & r_{53} \\ r_{61} & r_{62} & r_{63} \end{bmatrix} \begin{bmatrix} E_1 \\ E_2 \\ E_3 \end{bmatrix} \quad (2.14)$$

For $\bar{4}3m$ (zincblende) crystals such as GaAs, GaP, and ZnTe, r_{hk} has the form:

$$\begin{bmatrix} 0 & 0 & 0 \\ 0 & 0 & 0 \\ 0 & 0 & 0 \\ r_{41} & 0 & 0 \\ 0 & r_{41} & 0 \\ 0 & 0 & r_{41} \end{bmatrix} \quad (2.15)$$

Now, we will consider the following situation. We have a THz field E_{THz} that is incident upon a $\bar{4}3m$ crystal with a field that is polarized along the ($\bar{1}$10) crystal axis, or equivalently, has a polarization defined by the vector (-$\frac{\hat{X}}{\sqrt{2}}$, $\frac{\hat{Y}}{\sqrt{2}}$,0). The optical indicatrix (eq. 2.11) becomes:

$$\frac{(X^2 + Y^2 + Z^2)}{{n_0}^2} - \frac{E_{THz} r_{41} YZ}{{n_0}^2} + \frac{E_{THz} r_{41} XZ}{{n_0}^2} = 1 \quad (2.16)$$

Here, *X*, *Y*, and *Z* are the principal axes of the crystal when $E_{THz} = 0$, parallel to the (100), (010), and (001) directions, respectively. Following the approach presented in [55], we will need to find the principal axes for the case of $E_{THz} \neq 0$. To do this, we have to perform a few rotations. I found that the necessary transformation is:

$$\begin{pmatrix} X \\ Y \\ Z \end{pmatrix} = \begin{pmatrix} \frac{1}{\sqrt{2}} & -\frac{1}{\sqrt{2}} & 0 \\ \frac{1}{\sqrt{2}} & \frac{1}{\sqrt{2}} & 0 \\ 0 & 0 & 1 \end{pmatrix} \begin{pmatrix} 0 & 0 & 1 \\ 0 & 1 & 0 \\ -1 & 0 & 0 \end{pmatrix} \begin{pmatrix} \frac{1}{\sqrt{2}} & \frac{1}{\sqrt{2}} & 0 \\ -\frac{1}{\sqrt{2}} & \frac{1}{\sqrt{2}} & 0 \\ 0 & 0 & 1 \end{pmatrix} \begin{pmatrix} x \\ y \\ z \end{pmatrix} = \begin{pmatrix} \frac{z}{\sqrt{2}} + \frac{x-y}{2} \\ \frac{z}{\sqrt{2}} + \frac{-x+y}{2} \\ \frac{-x-y}{\sqrt{2}} \end{pmatrix} \quad (2.17)$$

where $x \parallel (\bar{1}11)$, $y \parallel (\bar{1}1\bar{1})$, z ∥ (110). After inserting the transformation, eq. 2.16 becomes:

$$\frac{z^2}{{n_0}^2} + x^2\left(\frac{1}{{n_0}^2} - r_{41}E_{THz}\right) + y^2\left(\frac{1}{{n_0}^2} + r_{41}E_{THz}\right) = 1 \quad (2.18)$$

Thus, for a zincblende crystal with <110> orientation, the refractive indexes parallel to the *x* and *y* directions are:

$$\frac{1}{{n_x}^2} = \left(\frac{1}{{n_0}^2} - r_{41}E_{THz}\right) \quad (2.19)$$

$$\frac{1}{{n_y}^2} = \left(\frac{1}{{n_0}^2} + r_{41}E_{THz}\right) \quad (2.20)$$

which gives us:

$$n_x = n_0(1 - {n_0}^2 r_{41}E_{THz})^{-1/2} \approx n_0 + \frac{1}{2}{n_0}^3 r_{41}E_{THz} \quad (2.21)$$

$$n_y = n_0(1 + {n_0}^2 r_{41}E_{THz})^{-1/2} \approx n_0 - \frac{1}{2}{n_0}^3 r_{41}E_{THz} \quad (2.22)$$

The phase difference $\Delta\phi$ between the y-component and x-component of an incident probe polarization as it passes through the crystal is given by:

$$\Delta\phi = (n_x - n_y)\frac{\omega_{pr}L}{c} = {n_0}^3 r_{41}E_{THz}\frac{\omega_{pr}L}{c} \quad (2.23)$$

Figure 2.5 shows the crystal axes that lie in the (110) plane. Let's assume that the probe pulse is polarized parallel to the THz pulse, that is, parallel to the $(\bar{1}10)$ axis (polarization vector = $(\frac{\hat{x}+\hat{y}}{\sqrt{2}})$).

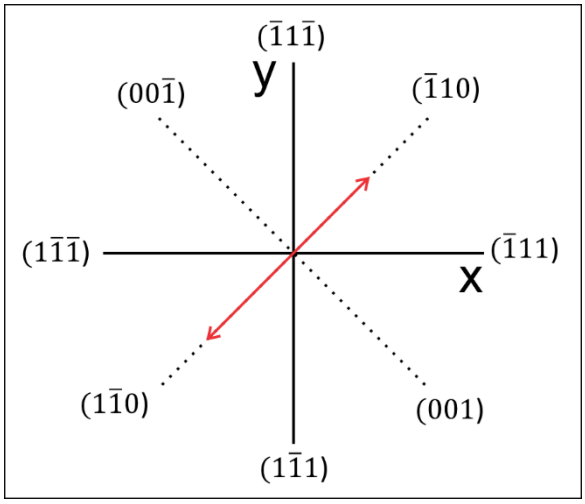

Figure 2.5. Crystal axes that lie in the (110) plane. Both, the probe pulse and the THz pulse are polarized parallel to the $(\bar{1}10)$ axis.

In order to detect a change in the probe beam that is linear with E_{THz}, we must do two additional things. First, we send the probe beam transmitted through the crystal though a quarter waveplate that has its fast and slow axes aligned parallel to the *x* and *y* crystal directions. This adds an additional $\pi/2$ phase between n_y and n_x:

$$\Delta\phi' = \Delta\phi + \frac{\pi}{2} \quad (2.24)$$

Now, using a Wollaston prism (or some other type of polarizing beam-splitter), we separate the components of the polarization that are parallel to the $(\bar{1}10)$ and (001) axes (or respectively, the $(\frac{\hat{x}+\hat{y}}{\sqrt{2}})$ and $(\frac{\hat{x}-\hat{y}}{\sqrt{2}})$ vectors). Mathematically, this is equivalent to:

$$E_{\bar{1}10} = E_0\left(\frac{\hat{x} + \hat{y}e^{i\Delta\phi'}}{\sqrt{2}}\right) \cdot \left(\frac{\hat{x} + \hat{y}}{\sqrt{2}}\right) = \frac{E_0}{2}\left(1 + e^{i\Delta\phi'}\right) \quad (2.25)$$

$$E_{001} = E_0\left(\frac{\hat{x} + \hat{y}e^{i\Delta\phi'}}{\sqrt{2}}\right) \cdot \left(\frac{\hat{x} - \hat{y}}{\sqrt{2}}\right) = \frac{E_0}{2}\left(1 - e^{i\Delta\phi'}\right) \quad (2.26)$$

Note that when $\Delta\phi' = 0$, E_{001} = 0. The corresponding intensities are:

$$I_{\bar{1}10} = |E_{\bar{1}10}|^2 = \left|\frac{E_0}{2}\left(1 + e^{i\Delta\phi'}\right)\right|^2 = \frac{I_0}{2}\left(1 + \cos(\Delta\phi')\right) = \frac{I_0}{2}\left(1 - \sin(\Delta\phi)\right) \approx \frac{I_0}{2}(1 - \Delta\phi)$$

$$(2.27)$$

$$I_{001} = |E_{001}|^2 = \left|\frac{E_0}{2}\left(1 - e^{i\Delta\phi'}\right)\right|^2 = \frac{I_0}{2}\left(1 - \cos(\Delta\phi')\right) = \frac{I_0}{2}\left(1 + \sin(\Delta\phi)\right) \approx \frac{I_0}{2}(1 + \Delta\phi)$$

$$(2.28)$$

$$\Delta I = I_{\bar{1}10} - I_{001} \approx I_0\Delta\phi = I_0 {n_0}^3 r_{41} E_{THz} \frac{\omega_{pr} L}{c} \quad (2.29)$$

Thus, after sending the transmitted probe through a properly aligned quarter waveplate and a Wallaston prism (or other polarizing beam splitter), we can measure a differential intensity ΔI that is proportional to the THz field.

2.2.3.2. Choice of Detection Crystal

The efficiency of the electro-optic sampling process is highly frequency-dependent; it depends strongly on the matching between the group velocity of the probe pulse at the probe carrier frequency ω_{pr} and the THz phase velocity as well as the frequency-dependent nonlinear susceptibility. Thus, the spectrum of the detected signal also has a strong dependence on the length L of the crystal. Other effects, such as frequency-dependence in the crystal's Fresnel coefficients as well as the probe pulse duration, also contribute. If one wished to calculate the response function of the crystal $R(\omega_{THz}; L; \omega_{pr})$ to high accuracy, then all of these items must certainly be considered. The expression for the detected THz field, $E_{THzDet}(\omega_{THz}; L; \omega_{pr})$, is then given by [53,55]:

$$E_{THzDet}(\omega_{THz}; L; \omega_{pr}) = E_{THz}(\omega_{THz}) R(\omega_{THz}; L; \omega_{pr}) \quad (2.30)$$

Depending on the needs of the experiment, certain crystals and thicknesses may be more suitable choices than others. Figure 2.6 illustrates this point.

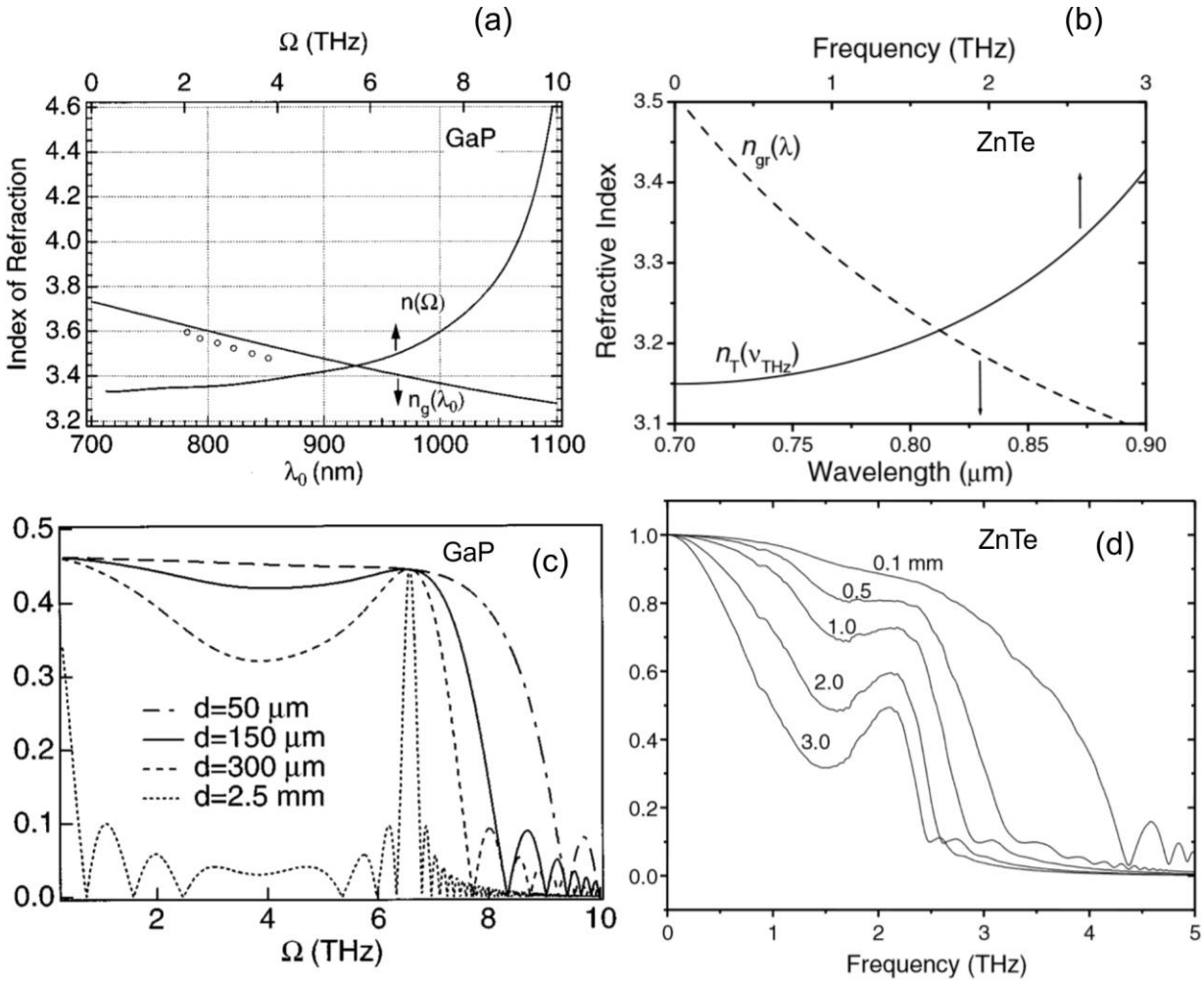

Figure 2.6. Plots of the group refractive index of the probe pulse and phase index of the THz pulse for (a) GaP and (b) ZnTe. The crystal responses $R(\omega_{THz}; L; \omega_{pr})$ are shown in (c) for GaP and (d) for ZnTe. The figures in (a) and (c) were taken from [56], and the figures in (b) and (d) were taken from [53].

If the THz pulse is narrowband and consists of frequencies that are very well phase-matched to the group velocity of the probe pulse, then a thicker crystal (~ 1 mm) is likely more beneficial, as ΔI is proportional to the length of propagation in the case of perfect phase-matching.

If detection bandwidth is more critical than efficiency, then thinner (< 1 mm) crystals should be used. The first TO phonon of GaP is located near 11 THz [56], which makes it a more suitable choice for broadband THz detection than ZnTe, which has a TO phonon at 5.3 THz [53]. However, for probe wavelengths near 800nm, ZnTe allows for considerably better phase-matching at frequencies near 1THz than GaP. In addition, the electro-optic coefficient of ZnTe (r_{41} =4 pm/V) is greater than that of GaP (r_{41} = 1 pm/V) [56]. As discussed below, a <110> ZnTe crystal of 1 mm thickness was the best choice for my measurements.

2.2.4. The THz-TDS Setup

The THz-TDS setup was built for the purpose of performing transmission measurements on the sub-wavelength-slotted waveguide and related structures discussed in Ch 3. The integrated power transmission through these structures is on the order of a few percent. Thus, in my case, a highly efficient THz-TDS system with a high signal-to-noise ratio was far more important than being able to perform measurements across a large bandwidth. I started out with a setup that I inherited from Ilya Vugmeyster, who had just recently graduated from the Merlin Lab. The setup was very remarkably and carefully built to perform reflection measurements over a range that extended from ~ 1THz up to ~ 8 THz [18]. For my own measurements, I found it best to rearrange the setup so that I can characterize the THz radiation transmitted through the sample. Figure 2.7 shows a schematic of the setup.

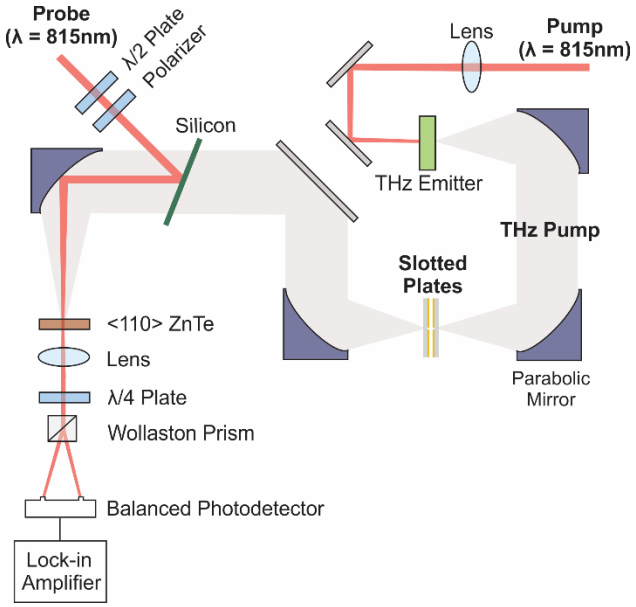

Figure 2.7. THz-TDS Setup used to conduct measurements on the slotted plates discussed in Ch.3. THz pulses were generated by focusing the output of a Ti:Sapphire oscillator, tuned to 815nm with a repetition rate of 82MHz, onto the biased TeraSED3 emitter which was modulated at 15 KHz. The path of the THz radiation was sealed inside a plexiglass enclosure filled with nitrogen gas in order to eliminate absorption by water vapor. A high-resistivity silicon wafer with an anti-reflective coating for near-IR wavelengths is used to combine the paths of the THz pump and the near-IR probe. As discussed in section 2.2.3.1, the THz field induces birefringence in the ZnTe crystal, causing the incident linear probe polarization to become elliptical. Upon transmission through a quarter wave plate, the vertical and horizontal polarization components of the probe are separated by a Wollaston prism. The difference in their intensities at a given time delay is proportional to the THz electric field.

I switched the detection crystal from the original <110> 340 μm-thick GaP crystal to a <110> 1 mm-thick ZnTe crystal which allowed for about an order of magnitude increase in the peak THz signal. The drawback, as discussed in the preceding section, is that this also had the effect of limiting the measurable bandwidth. In addition, I found that I was able to increase the overall signal by collecting the THz radiation emitted by the photoconductive antenna in the transmission geometry rather than the original reflection geometry. For the case of the transmission geometry, the THz radiation passes through the emitter's GaAs substrate, which also limits the bandwidth due to absorption from a TO phonon near ~ 8 THz. However, after making all of these

changes, I was able to increase the peak signal of the reference THz trace by nearly a factor of 1000, which was vital for obtaining high quality measurements on the slotted plates. Figure 2.8 shows the final THz trace I used for measurements on the slotted plates and the first trace I measured with the setup in its initial configuration. The changes in the spectrum of the reference pulse for different setup configurations are also shown.

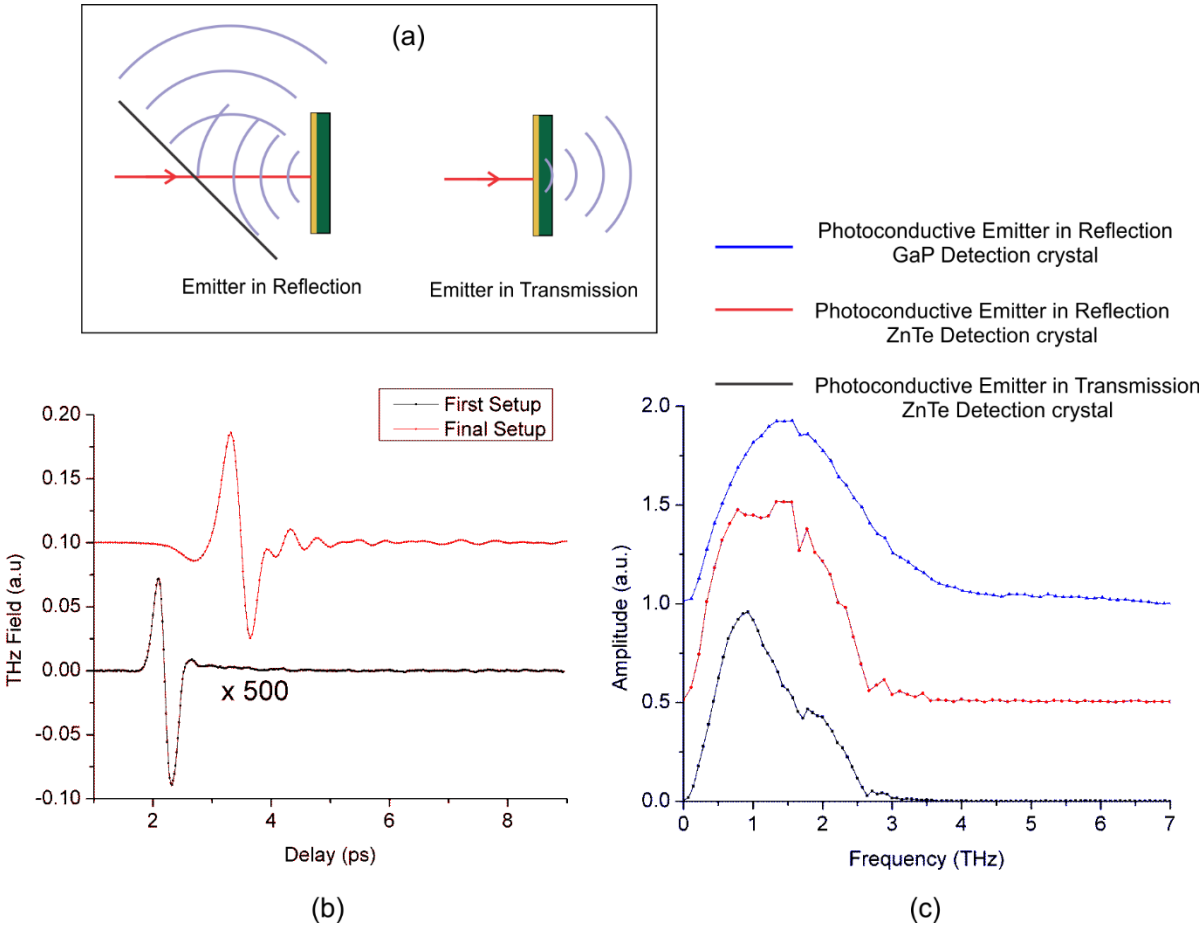

Figure 2.8. Evolution of the THz-TDS setup. (a) Schematics describing the emission of THz radiation. The radiation emitted into the air or transmitted through the GaAs substrate can be collected for a given experiment. (b) Plots showing the reference signal used to perform measurements on the slotted plates, along with the reference trace obtained from the setup in its first configuration. (c) Plots of the detected reference spectrum for different setup configurations. The peak of each spectrum is normalized to 1. The configuration which used a photoconductive emitter in the transmission geometry along with a ZnTe crystal for detection provided the largest peak signal, despite the reduction in bandwidth.

2.3. Frequency Shift Detection of THz Radiation

2.3.1. Introduction

In the previous section, we discussed a method for detecting THz radiation that takes advantage of the change in polarization of the probe pulse when it interacts with the THz field through the second order nonlinear susceptibility. Here, I will present a slightly different method for detecting the THz field that is useful in the case of group 3m crystals such as $LiTaO_3$ and $LiNiO_3$, which have static birefringence that makes the detection of THz radiation using a polarization-based technique more difficult. Experiments which use polarization-based techniques and compensate for this birefringence have been reported [57]. However, the method described here, which is an adaptation of a technique used to detect coherent phonons [58,59] is far easier to implement. This detection method is used to probe the THz-frequency synchrotron radiation generated inside $LiTaO_3$, discussed in Chapter 5.

2.3.2. Frequency-Shift Detection with a Transform-Limited Probe Pulse

We can safely assume that the energy of the probe beam is not depleted by from interaction with the THz field. Here, for the sake of understanding the detection process, we are going to assume that the probe pulse and THz field propagate co-linearly and are perfectly phase-matched. Putting these things together, the inhomogeneous equation which describes the scattered field $E_{sc}(z,t)$ resulting from the interaction of the THz field E_{THz} and probe field E_{pr} is:

$$\frac{\partial^2}{\partial z^2}E_{sc}(z,t) - \frac{n^2}{c^2}\frac{\partial^2}{\partial t^2}E_{sc}(z,t) \approx \frac{\chi_2}{\epsilon_0 c^2}\frac{\partial^2}{\partial t^2}\Big(E_{pr}(z,t)E_{THz}(z,t)\Big) \quad (2.31)$$

where E_{pr} is the incident probe field, E_{THz} is the THz field, and E_{sc} is field scattered from the mixing of E_{pr} and E_{THz}. Now, if we change variables and write eq. (2.31) in terms of the retarded time $t' = t - zn/c$, then we have:

$$\frac{\partial^2}{\partial z^2}E_{sc}(z,t') - \frac{2n}{c}\frac{\partial^2}{\partial t'\partial z}E_{sc}(z,t') = \frac{1}{\epsilon_0 c^2}\frac{\partial}{\partial t'}\left(\chi_2 E_{pr}(z,t')E_{THz}(z,t')\right) \quad (2.32)$$

The general solutions is [58]:

$$E_{sc}(z,t') = E_{pr}(t') - \frac{\chi_2 z}{2\epsilon_0 cn} \times \frac{\partial}{\partial t'}\left(E_{pr}(t')E_{THz}(t')\right) \quad (2.33)$$

Now, we assume that the THz field has the form of a Gaussian pulse:

$$E_{THz}(t') = e^{-(t'/2T_t)^2}e^{-i\omega_t t'} + c.c. \quad (2.34)$$

We do likewise for the probe field. In addition, we assume that the probe's arrival time can be delayed by a time t_d. This gives us:

$$E_{pr}(t') = e^{-((t'+t_d)/2T_{pr})^2}e^{-i\omega_{pr}(t'+t_d)} + c.c \quad (2.35)$$

If we input these fields into (2.33) and take the Fourier transform, we get:

$$\hat{E}_{sc}(\omega;t_d) = \hat{E}_{pr}(\omega;t_d) - i\omega\frac{\chi_2 z}{2\epsilon_0 cn}\int\left(E_{pr}(t')E_{THz}(t')\right)e^{i\omega t'}dt' \quad (2.36)$$

which then becomes:

$$\hat{E}_{sc}(\omega;t_d)=\left[e^{\left(-\frac{{t_d}^2}{2{T_{pr}}^2}-i\omega_{pr}t_d\right)}e^{\frac{{T_{pr}}^2}{2}\left(\frac{{t_d}^2}{{T_{pr}}^4}+\frac{i2t_d}{{T_{pr}}^2}(\omega_{pr}-\omega)-(\omega_{pr}-\omega)^2\right)}\right.$$

$$\left.+\,e^{\left(-\frac{{t_d}^2}{2{T_{pr}}^2}+i\omega_{pr}t_d\right)}e^{\frac{{T_{pr}}^2}{2}\left(\frac{{t_d}^2}{{T_{pr}}^4}-\frac{i2t_d}{{T_{pr}}^2}(\omega_{pr}+\omega)-(\omega_{pr}+\omega)^2\right)}\right]$$

$$-\;i\omega\frac{\chi_2 z}{2\epsilon_0 cn}\left\{e^{\left(-\frac{{t_d}^2}{2{T_{pr}}^2}-i\omega_{pr}t_d\right)}\right.$$

$$\times\left[e^{\frac{\frac{1}{2}\left(\frac{{t_d}^2}{{T_{pr}}^4}+\frac{i2t_d}{{T_{pr}}^2}(\omega_{pr}-\omega_t-\omega)-(\omega_{pr}-\omega_t-\omega)^2\right)}{\left(\frac{1}{{T_{pr}}^2}+\frac{1}{{T_t}^2}\right)}}\right.$$

$$\left.+\;e^{\frac{\frac{1}{2}\left(\frac{{t_d}^2}{{T_{pr}}^4}+\frac{i2t_d}{{T_{pr}}^2}(\omega_{pr}+\omega_t-\omega)-(\omega_{pr}+\omega_t-\omega)^2\right)}{\left(\frac{1}{{T_{pr}}^2}+\frac{1}{{T_t}^2}\right)}}\right]+e^{\left(-\frac{{t_d}^2}{2{T_{pr}}^2}+i\omega_{pr}t_d\right)}$$

$$\times\left[e^{\frac{\frac{1}{2}\left(\frac{{t_d}^2}{{T_{pr}}^4}-\frac{i2t_d}{{T_{pr}}^2}(\omega_{pr}-\omega_t+\omega)-(\omega_{pr}-\omega_t+\omega)^2\right)}{\left(\frac{1}{{T_{pr}}^2}+\frac{1}{{T_t}^2}\right)}}\right.$$

$$\left.\left.+\;e^{\frac{\frac{1}{2}\left(\frac{{t_d}^2}{{T_{pr}}^4}-\frac{i2t_d}{{T_{pr}}^2}(\omega_{pr}+\omega_t+\omega)-(\omega_{pr}+\omega_t+\omega)^2\right)}{\left(\frac{1}{{T_{pr}}^2}+\frac{1}{{T_t}^2}\right)}}\right]\right\}\qquad(2.37)$$

Thus, the scattered field contains delay-dependent frequency shifts.

Now, let's calculate the integrated intensity of the scattered field and subtract it from the integrated intensity of a reference probe field, just as we would do in a balanced detection scheme:

$$\Delta I_{calc}(t_d) = \int \left| \hat{E}_{sc}(\omega; t_d) \right|^2 d\omega - \int \left| \hat{E}_{pr}(\omega) \right|^2 d\omega \quad (2.38)$$

It has been shown for the case of coherent phonons that the differential intensity trace $\Delta I_{calc}(t_d)$ is proportional to the time-derivative of the amplitude of the excited phonon [58,59]. We find that this is also true for a THz pulse; Figure 2.9 shows the results of the numerical evaluation of eq. (2.38).

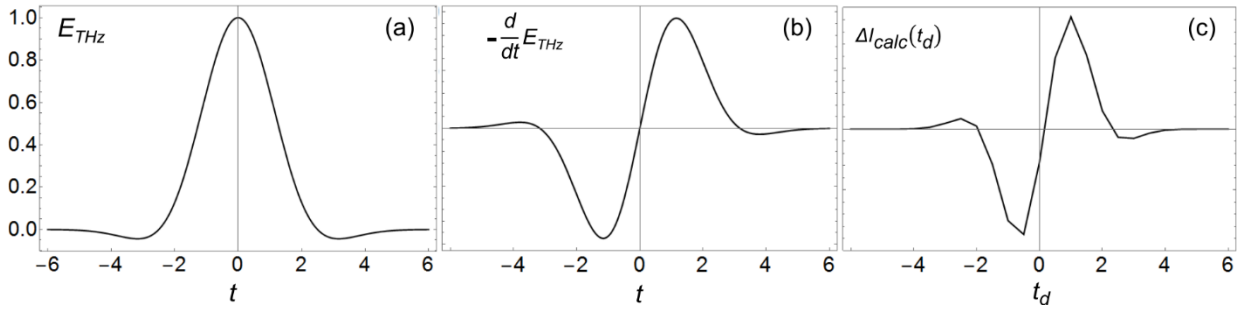

Figure 2.9. (a) Plot of eq. (2.34) for $\omega_t/2\pi = 1$THz and $T_t = 0.15$ ps and (b) the negative of its time-derivative. (c) Numerical evaluation of eq. (2.38) for the parameters in (a) and (b) and for a probe beam with $\omega_{pr}/2\pi = 3.75 \times 10^{14}$ Hz (wavelength, $\lambda = 800$ nm) and $T_{pr} = 65$ fs. $\Delta I_{calc}(t_d)$ is proportional to the time-derivative of the THz field.

The balanced photodetector used in the lab has a frequency-dependent response $R(\omega)$. Taking this into consideration, eq. (2.38) then becomes:

$$\Delta I_{det}(t_d) = \int \left| \hat{E}_{sc}(\omega; t_d) \right|^2 R(\omega) d\omega - \int \left| \hat{E}_{pr}(\omega) \right|^2 R(\omega) d\omega \quad (2.39)$$

For the silicon photodiodes used in the experiment, the response was modelled as [60]:

$$R(\omega) = (-1.00931 + 3.387(2\pi \times 3 \times 10^{14}/\omega) - 1.7133(2\pi \times 3 \times 10^{14}/\omega)^2) \quad (2.40)$$

When we evaluate eq. (2.39) using eq. (2.40), we find that $\Delta I_{det}(t_d)$ is less than $\Delta I_{calc}(t_d)$ by a factor of 10, as shown in Figure 2.10(a). We can actually increase the value of ΔI_{calc} considerably by detecting only half of the scattered field spectrum and balancing the signal with the integrated intensity of an unfiltered reference pulse. This is also equivalent to:

$$\Delta I_{detB}(t_d) = \int_{\omega_{pr}}^{\omega_{max}} \left| \hat{E}_{sc}(\omega; t_d) \right|^2 R(\omega) d\omega - \int_{\omega_{pr}}^{\omega_{max}} \left| \hat{E}_{pr}(\omega) \right|^2 R(\omega) d\omega \quad (2.41)$$

and

$$\Delta I_{detR}(t_d) = \int_{\omega_{min}}^{\omega_{pr}} \left| \hat{E}_{sc}(\omega; t_d) \right|^2 R(\omega) d\omega - \int_{\omega_{min}}^{\omega_{pr}} \left| \hat{E}_{pr}(\omega) \right|^2 R(\omega) d\omega \quad (2.42)$$

Figure 2.10(b) shows the results. Clearly, there is a factor of 400 increase the calculated detected signal when detecting only half the probe spectrum. This behavior is also observed in collinear pump-probe measurements that I performed on $LiTaO_3$, shown in Figure 2.10(c).

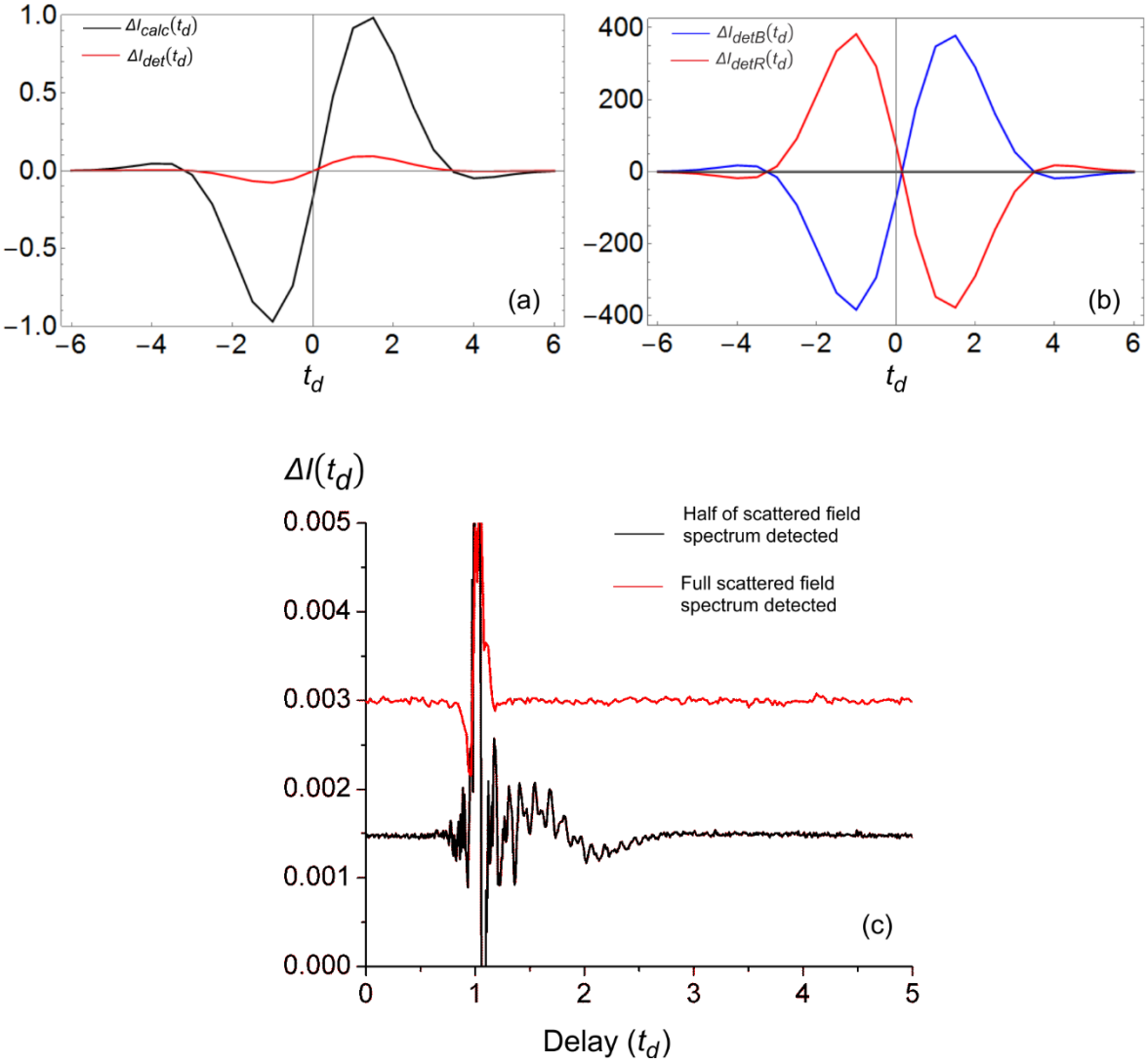

Figure 2.10. (a) Plots of $\Delta I_{calc}(t_d)$ and $\Delta I_{det}(t_d)$. Parameters for the THz field and the probe field are the same as those used in Figure 2.8. (b) Plots of $\Delta I_{detB}(t_d)$ and $\Delta I_{detR}(t_d)$, which are both normalized to the maximum of $\Delta I_{det}(t_d)$. By detecting only half of the probe spectrum, the peak differential intensity signal for a detector with a response given by eq. (2.40) increases by roughly a factor of 400. (c) Results of a differential transmission pump-probe measurement on $LiTaO_3$ for pump and probe pulses of wavelength 800 nm and pulse durations of 50 fs. Here, the pump and probe propagate collinearly and share some spatial overlap. The large signal at $t_d = 1$ ps indicates the simultaneous arrival of the pump and probe pulses. For the black trace, the beam transmitted through the sample was sent through a long-pass filter that had a cut-off wavelength of 800 nm. The signal that has a period of ~ 2 ps is the THz radiation that results from the difference-frequency mixing of the pump field with itself though the second order nonlinear susceptibility χ_2. The higher frequency signals are associated with coherent phonons. These signals disappear when the full spectrum of the transmitted probe is sent to the balanced photodetector, as shown in the red trace.

2.3.3. Detection with a Chirped Probe Pulse

In the orthogonal pump-probe measurements that are used to obtain the data on $LiTaO_3$ presented in Ch. 5, the probe pulse passes through several millimeters of the $LiTaO_3$ crystal before interacting with the difference-frequency THz field generated by the pump. As a result, the pulse acquires chirp, which affects the detection process; this was discussed in the thesis of Greg Garrett for the detection of coherent phonons [60]. Figure 2.11 summarizes the result.

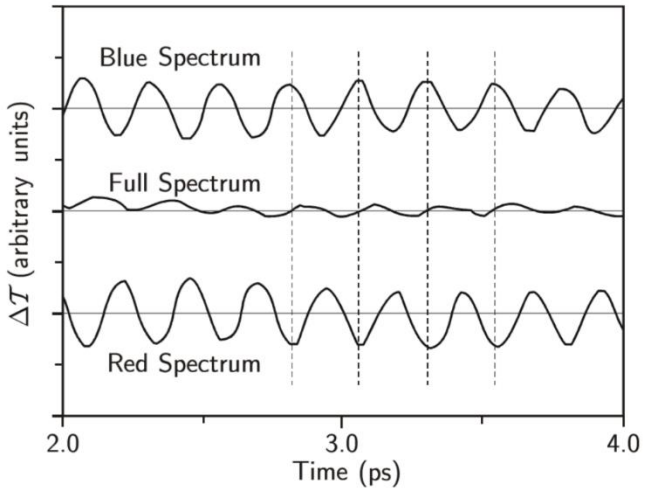

Figure 2.11. Pump-probe data for ϵ-GaSe, which illustrates the effects of pulse chirp on the detection process. The signal obtained when detecting the full probe spectrum is on the same order of magnitude as those obtained when detecting half of the spectrum. In addition, the full-spectrum signal has a $\pi/2$ phase shift relative to the other two signals. The figure was taken from [60].

When detecting the full probe spectrum, we will now observe a signal that has a magnitude comparable to the signals obtained when detecting half of the probe spectrum. I observed this in my orthogonal pump-probe measurements, but not in the collinear pump-probe measurements (Figure 2.10). In the latter, I used a prism compressor that successfully compensated for group velocity dispersion in both, the pump and probe pulses. Thus, the probe pulse interacting with the THz radiation was very close to being transform-limited, and the experiment behaves as predicted in section 2.3.1. In the orthogonal measurements, I was only able to compensate for dispersion in

the pump pulse, and the probe pulse that interacted with the THz radiation after propagating through ~ 6 mm of $LiTaO_3$ was chirped considerably.

In pnnciple, we can model this effect using the approach described above. The second term in eq. (2.33) can be written as:

$$i\omega\frac{\chi_2 z}{2\pi cn}\int\left(E_{pr}(t')E_{THz}(t')\right)e^{i\omega t'}dt' = i\omega\frac{\chi_2 z}{2\pi cn}\hat{E}_{pr}(\omega)\otimes\hat{E}_{THz}(\omega)$$

$$= i\omega\frac{\chi_2 z}{2\pi cn}\int\hat{E}_{pr}(\omega')\hat{E}_{THz}(\omega-\omega')d\omega' \quad (2.43)$$

If we take $\hat{E}_{pr}(\omega')$ to now have a quadratic phase shift that is associated with a linear chirp in the time domain, then we have:

$$\hat{E}_{pr}(\omega') = e^{\frac{-{T_{pr}}^2}{2}(\omega_{pr}-\omega)^2+i\beta(\omega_{pr}-\omega)^2} + c.c. \quad (2.44)$$

Then, we should be able to evaluate eq. (2.33) using eqns. (2.43) and (2.44). Unfortunately, I was not able to obtain calculations of ΔI that were consistent with the results shown in Figure 2.10 and discussed in [60] Thus, the ability to simulate the effect of a chirped probe pulse on the measurement of ΔI when detecting a THz pulse remains to be done for future work.

2.4. Edge-Polishing for Imaging and Orthogonal Pump-Probe Measurements

2.4.1. Introduction

In the experiments described in Ch. 4 and Ch. 5, it was necessary to polish the 1 mm-wide edges of both glass and $LiTaO_3$ substrates. In the case of the former, it was only necessary to polish one edge. In the case of the latter, it was necessary to polish all four of the edges for reasons presented in Ch 5. Figure 2.12 shows partial schematics of the experimental geometries which required the

samples to undergo the edge polishing process. Unless distinctions are made, the processes discussed in this section apply to both, the glass and $LiTaO_3$ substrates.

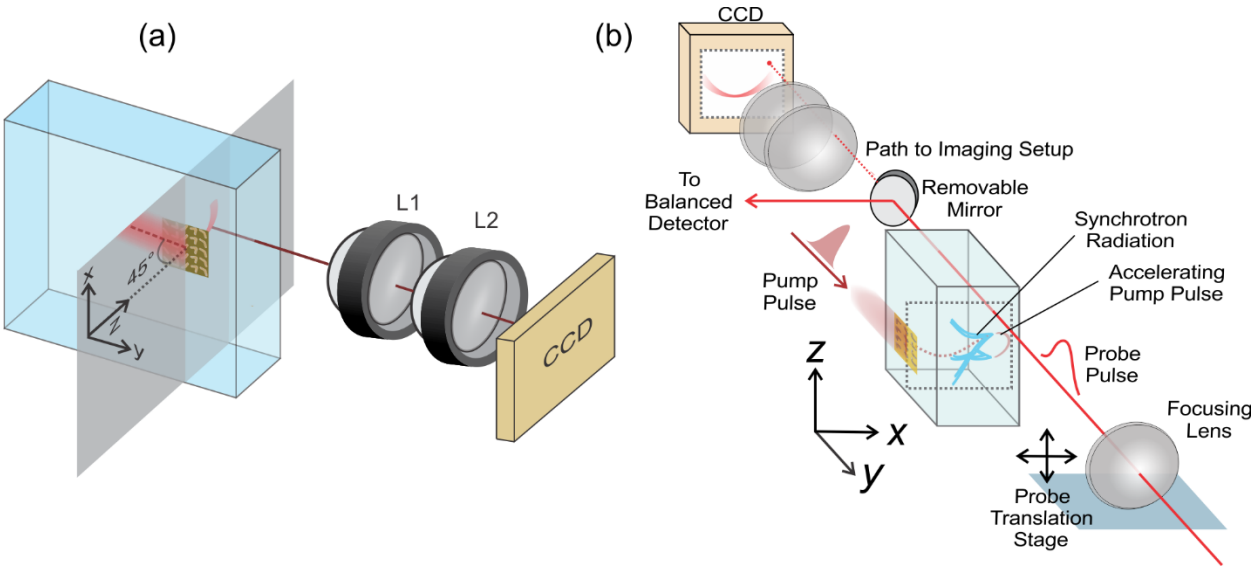

Figure 2.12. The setups which require edge polishing of the sample substrates. (a) Setup for imaging the metasurface-produced accelerating light generated inside a glass substrate. The lens L1 collects light that is Rayleigh-scattered inside the glass from the curved trajectory. To facilitate the imaging, the side of the glass was polished down to optical quality. (b) Joint-imaging and orthogonal pump-probe setup. As discussed in Ch. 5, it was necessary to polish all four sides of 1 mm thickness (the x-y and x-z crystal planes) down to optical quality.

There is the experience of Sisyphys, who in retribution for his earthly crimes, was sentenced to push a rock to the top of a hill. Each time he got close, the rock would slip and roll to the bottom, and the process repeated for eternity. The fate of Sisyphys resembles greatly that of a person such as myself who embarks upon the journey of polishing samples. You finish the process, obtain a beautiful final product, and then when dismounting the sample, some 10 µm-sized particle comes along and scratches some other surface of your sample that you certainly did not want scratched. Luckily, in my case, I was able to produce samples with a minimal number of collateral

scratches, and Di at Purdue had no problems performing fabrication on the processed substrates I sent. So, contrary to the story of Sisyphys, my toil did evenutally come to an end.

I would like to thank someone who was absolutely indispensable for the success of this portion of my projects: Dr. Pilar Herrera-Fierro. Pilar showed me methods for mounting the substrates, trained me on all necessary equipment, and her advice was tantamount to success. Pilar is a very smart, talented, and stunningly beautiful person, inside and out. I clearly remember the day I met her: April 1st, 2015 at the LNF training session. On this day, I realized that by knowing Pilar, my life was going to change for the better in a number of ways. Not surprisingly, it turns out that I was right. Pilar, thank you. This portion of my thesis is dedicated to you.

2.4.2. Lapping and Polishing System

All samples were polished using the Logitech PM5 Lapping and Polishing System located at the University of Michigan Lurie Nanofabrication Facility (LNF). A picture of the system is shown in Figure 2.13.

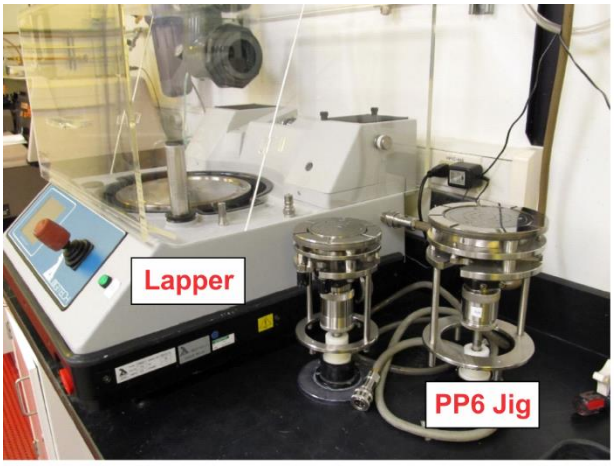

Figure 2.13. Logitech PM5 Lapping and Polishing System at the University of Michigan LNF. The photo (without annotations) is courtesy of the LNF Wiki page for the PM5.

The PP6 jig shown in Figure 2.13 holds a sample in place via the application of a vacuum. It has an adjustable spring that allows the user to adjust the force applied to the sample. The spring's displacement is also measured with a micrometer, which allows the user to monitor how much material is being removed from the sample during the lapping processes.

The mixture of water and abrasive particles used to lap/polish a sample is known as slurry. The PM5 lapper has an automated slurry-delivery system (not shown in the photo). Basically, the slurry bottle, which has an especially-engineered opening, rotates continuously on a set of rollers. This keeps the slurry homogeneous while allowing it to fall out of the opening and onto the rotating lapping platform. The unique bottle opening can be tweaked to adjust the slurry flow. Too little slurry can destroy the sample that is being polished, as the water in the slurry also serves as a lubricant for the samples and the lapping platform. However, too much slurry can cause the sample to hydroplane on the platform, leading to an inefficient process. So, it's like Goldilocks and the porridge – it has to be just right. Of course, as the rotational speed of the lapping platform increases, the user has to increase the slurry flow accordingly. There is no considerable quantitative metric for determining the right amount of slurry -- I found that keeping the platform consistently wet, but not obviously overburdened with slurry, is sufficient.

Also not shown in the photo is a mechanical arm that keeps the PP6 jig in place while the lapping platform rotates, and this arm also can sweep the jig's position along a small arc. This sweeping motion is important for achieving a uniformly polished surface once the sample reaches the final polishing stages.

2.4.3. Substrate Cutting

Glass Substrates. Glass substrates of dimensions 2.54 × 2.54 × 0.1 cm that had a thin layer of indium tin oxide (ITO) coated on one side were purchased from Sigma-Aldrich. As discussed

later, the PP6 polishing jig has a height constraint – the top of the mounted sample cannot exceed 1.7 cm from the surface of the jig. Thus, the samples needed to be cut. Using a diamond scribe and wafer cleaver, the substrates were cut to dimensions of 1.25 × 2.54 × 0.1 cm.

X-Cut $LiTaO_3$ Substrates. Rectangles of dimensions 7 mm x 13 mm were cut from a 2" diameter X-cut $LiTaO_3$ wafer of 1 mm thickness using a dicing saw. The longer 13 mm side made it easier for Di to mount the substrates for fabrication, and the 7 mm dimension allows for a focused probe pulse propagating parallel to the crystal's y-axis to enter and exit without obstruction. Prior to cutting, both sides of the wafer were covered with a protective layer of photoresist, as discussed in the next section. Since it was necessary to polish all four of the 1 mm-wide sides of the $LiTaO_3$ crystal, the mounting and polishing process discussed below was applied to these substrates four times.

2.4.4. Substrate Preparation

To protect the large area surfaces of the substrates, a protective layer of SPR 220-3.0 positive photoresist (Shipley Corporation) was deposited onto both sides of the substrate. To complete the deposition on one side, the resist was spin-coated at a speed of 3000 RPM, which gave a uniform coating of resist with a thickness of approximately 3 μm. Then, the substrate was placed onto a hot plate at which it was soft-baked at a temperature of 115° C for a time duration of 90 s. The process was then repeated for the second side.

2.4.5. Sample Mounting

Several substrates were securely mounted to a glass disk using beeswax, and the disk was then attached to the PP6 jig. During the mounting process, the substrates and glass disk were continuously heated to a temperature between 100° C and 110 ° C. The substrates were stacked together, and a layer of beeswax was placed between each set of surfaces. With the surfaces to be

polished facing upward, the substrate stack was mounted onto the glass plate, supported between two stacks of glass slides which were also mounted together using beeswax. Figure 2.14 shows a photo of the mounted substrates.

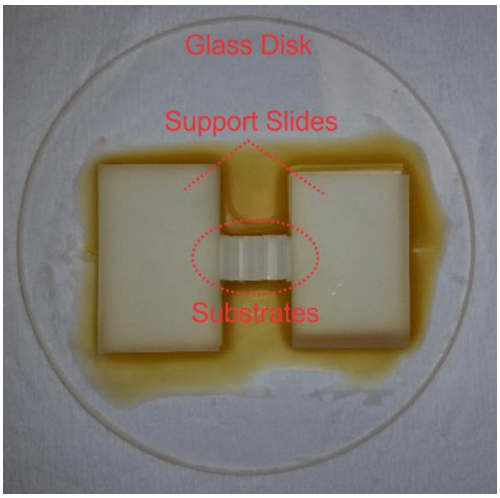

Figure 2.14. Image of the substrates mounted onto the glass disk.

While keeping the disk and substrates heated, a wafer press was used to apply a downward pressure onto the substrate stack for about 5 minutes in order to push out the excess wax from underneath the substrates and support slides. In order to make sure that the planes to be polished were almost perfectly parallel to the surface of the glass disk, I did the following: I let the wax begin to cool, and I used one hand to squeeze the slide stack together (which supported the upright position of the substrate stack) and another hand to apply a downward force onto the substrate stack. I applied these pressures until the wax hardened (~ 1 minute). The glass disk was then ready to be attached to the PP6 jig.

2.4.6. Lapping and Polishing Steps

Once the mounting was completed, it was a matter of simply attaching the glass disk to the PP6 jig and then beginning the lapping process. The process used here is the same for the glass and $LiTaO_3$ samples. For the coarser polishing steps, a glass lapping platform was used. Initially, a 20 µm slurry was used to lap off a few hundred microns of material so that the samples all had the same height and could be polished uniformly. At this stage, I set the lapping platform to rotate at roughly 20 RPM or so, depending on how fast the material was being removed. The substrates were then ready to be processed with finer grit slurries for the polishing phase.

When changing from a coarser to a finer slurry, it is absolutely vital to rinse the samples and all equipment that comes in contact with the slurry with distilled water. Otherwise, residual particles from the previous lapping/polishing stage can scratch the samples, and then you are doomed to start over. Between each stage, the mounted samples were cleaned using distilled water and an ultra-soft soft foam brush in order to lift particles.

The substrates were then polished using a 9 µm slurry, followed by a step with a 1 µm slurry. For both, the 9 µm and 1 µm stages, I set the platform to rotate at 30 RPM for roughly 10 to 15 minutes, and the mechanical arm which supports the jig was swept. For the 1 µm stage, it was necessary to use a steel polishing platform that was covered with a firm polishing pad. The final polishing stage required the use of a special SF1 colloidal silica slurry. This slurry is slightly basic, so the material is removed via a mechanical process from the abrasive silica particles and also from a chemical etch process, resulting in a roughness down to 1 nm. A steel lapping platform covered with a slightly squishy, felt-like pad was used. It was necessary to set the platform to rotate at a speed of 35 RPM for 90 minutes, and the jig was swept with the mechanical arm throughout

the entire duration. Figure 2.15 shows images of the edge surfaces after each of the polishing stages.

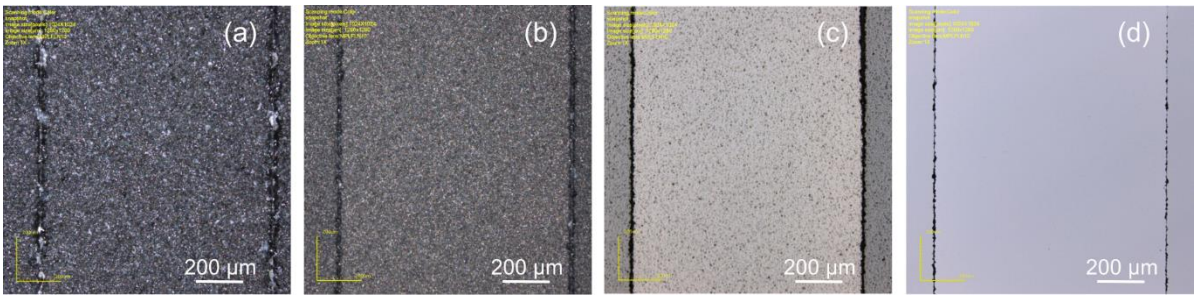

Figure 2.15. Optical microscope images (reflection geometry) of the substrate stack after processing with the (a) 20 µm slurry (b) 9 µm slurry (c) 1 µm slurry and (d) SF1 colloidal silica slurry

2.4.7 Sample Removal and Cleaning

Upon completion of the polishing process, the glass disk was placed on a hot plate in order to melt the wax. I used tweezers to push the corner of each substrate in order to slide it off of the stack. Between the protective resist layer and the lubrication from the hot wax, this worked pretty well.

The substrates were put in a xylene solution and were then heated to a temperature between 105° C and 115° C. The heating was necessary for dissolving the wax into the xylene, and I also found it necessary to put the samples into two to three heated baths for a good cleaning. The substrates were then placed into an acetone bath to dissolve the SPR 220-3.0 photoresist followed by a final rinse in an isopropyl alcohol (IPA) bath. The polished edges of each substrate were observed under a stereo microscope to inspect for any large scale scratches or debris, and a quick inspection of the large-area surfaces were observed under a 10X microscope objective to ensure that they were not scratched during the process. The final substrates were then placed in a “gel

pak" and mailed to Purdue University where Di Wang, a member of both, the Shalaev and Boltasseva labs, performed the metasurface fabrication.

2.5. Spatially-Resolved Orthogonal Pump-Probe Measurements

Here, I present the details of the experiment used to detect the THz-frequency synchrotron radiation generated by an optical pulse accelerating in $LiTaO_3$, as discussed in Ch. 5.

2.5.1 Experimental Setup

An accelerating pulse was generated by illuminating a metasurface with a pulse of 800 nm central wavelength and duration of 100 fs from a regeneratively amplified Ti: Sapphire oscillator of repetition rate 250 kHz. Cylindrical lenses were used to focus the light onto the metasurface, resulting in a spot whose full-width at half maximum (FWHM) dimensions were roughly 300 μm along the *z*-axis and 20 μm along the *y*-axis. We performed a spatially-resolved orthogonal pump-probe experiment to detect the THz synchrotron radiation generated by the accelerating pump pulse. The experimental setup is shown in Figure 2.16.

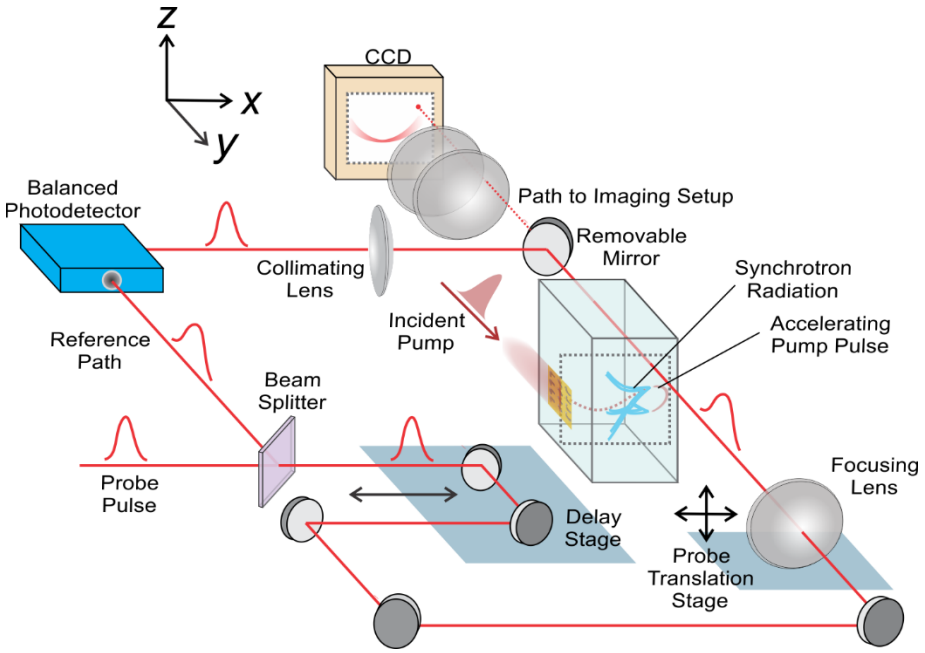

Figure 2.16. Schematic of the spatially-resolved orthogonal pump-probe measurement. The output of a measurement set is an image sequence showing the time-evolution of the time-derivative of the pump pulse intensity and the THz synchrotron radiation field.

The probe pulse was polarized parallel to the optical (*z*) axis of the $LiTaO_3$ crystal, and the accelerating pump had a polarization that rotated in the *x*-*z* plane with propagation. The probe beam was sent through a delay line and then split into a sample path and a reference path. The pulse travelling along the sample path was focused through the 1 mm-wide *x*-*z* plane of the $LiTaO_3$ crystal to a 10-μm- FWHM spot at the plane of the accelerating beam trajectory. The focusing lens was mounted onto a motorized translation stage, allowing for the scanning of the focused probe pulse throughout the plane of acceleration. For phase-sensitive detection, the incident beam was modulated at 2 kHz with a mechanical chopper. Using a standard imaging setup, the accelerating beam and the focused probe beam were first imaged together in order to calibrate the probe's position. The probe beam transmitted through the sample was then directed to a balanced photodetector at which its average intensity was subtracted from that of the reference pulse. The resulting differential signal was analyzed with a lock-in amplifier.

The focused probe pulse was translated throughout a 400×400 μm^2 area in steps of 10 μm. At each position, the pulse was delayed up to 5.2 ps in steps of 53.4 fs. The delay of the probe pulse and the scanning of the probe lens's translation stage was controlled with a single Newport ESP 301 3-axis motion controller and driver. The process of displacing the probe beam, scanning the delay line, and storing the indexed file which contained the lock-in output as a function of delay for each position of the probe focus was entirely automated using a Labview program. Each scan of the delay line took about 60s. Thus, to scan the delay line for 1600 positions of the probe takes about 27 hours – trying to complete such an experiment manually would likely bring an unsightly end to a person. The program which controls the delay line was written years ago by several individuals in the Merlin Lab. Jessica Ames, who received a Ph.D under the mentorship of Ted Norris, took the liberty of modernizing, restructuring, and adding features to this program. Jessica's work made it fairly simple for me to implement code that automated the process of scanning the three stages and indexing/saving the data. In part, because of her work, I was able run a 27 hour experiment with the click of a Labview "GO" button and have a somewhat pleasant life in the meantime. For this, I am eternally grateful.

The width of the pump beam parallel to the probe's propagation direction, that is, the *y*-axis, was 20 μm, which is considerably larger than the non-diffracting focus of the accelerating beam (~ 1 μm). As a result, the THz field was effectively two-dimensional in that its profile did not depend much on the direction parallel to the probe propagation. The interaction length between the probe pulse and the THz field was thus also 20 μm. Such a length was sufficiently long to obtain a reasonable signal and short enough so that it took only the center of the probe pulse 150 fs to pass through the pump and THz fields at any given position. Changes in the pump and THz field during this time duration are very small.

At any given position of the probe focus, a trace showing the differential intensity as a function of delay can contain two types of signals. Figure 2.17 shows an example.

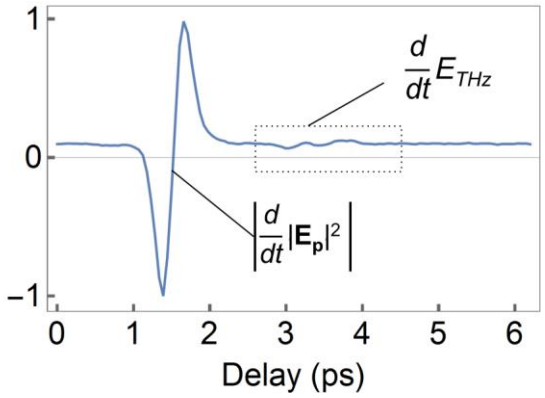

Figure 2.17. Differential intensity as a function of delay at a given position of the probe focus. Signals proportional to the time-derivatives of the pump pulse intensity and THz synchrotron field are measured.

The first type results from the spatial and temporal overlap of the probe and pump pulses, as the probe experiences the Kerr-effect-induced change in refractive index created by the accelerating pump. The resulting signal as a function of delay is proportional to the time-derivative of the pump intensity that passes through the probe focus [59]. The second differential signal results from the $\chi^{(2)}$ - mixing of the probe field with the THz synchrotron field, which creates delay-dependent changes in the transmission spectrum of the probe [58,59]. The delay-dependent differential signal is proportional to the time-derivative of the THz field that passes through the probe focus. The output of a completed measurement is an image sequence, which shows the propagation of the time-derivatives of the pump intensity and the THz synchrotron radiation.

2.5.2 Processing of the Data

The output of a given measurement was an image sequence showing the progression of three features: (1) the unperturbed 800 nm transmitted beam, (2) the accelerating 800 nm pulse, and (3) the THz synchrotron radiation. The experimentally obtained image of these features is shown in Figure 2.18 for a probe delay of 1.76 ps. The THz radiation is easily identified since it propagates at a speed that is three times smaller than that of the 800 nm pulses, consistent with the optical properties of $LiTaO_3$.

In order to generate the contour plots in Ch.5, it was necessary to separate the signals associated with the accelerating pump intensity and the THz field. To that end, the unperturbed transmitted beam, which propagates at 19° with respect to the metasurface normal according to Snell's law, was first digitally removed from the data. The impinging beam has a length that is slightly longer than the length of the metasurface, leading to the presence of two unperturbed pulses in the images. The first pulse results from the portion of the incident beam that impinges directly above the metasurface. This pulse is spatially isolated from the accelerating beam and its pixels were simply removed from the data matrices. The second unperturbed pulse, which passes through the metasurface and overlaps spatially with the accelerating beam, was fit to the time derivative of a Gaussian pulse envelope propagating at an angle of 19° inside the $LiTaO_3$ crystal. The fit was subtracted from the data for each image in the sequence. Pixels of the fit residual, separate from those of the accelerating pulse, were removed as well as the pixels representing the THz field. The remaining points in each matrix compose an image of the time-derivative of the accelerating pump intensity. Using a copy of the data, the pixels associated with the THz synchrotron field were isolated from each matrix in the image sequence. The results were plotted together with the time-derivative of the pump intensity, as shown in Ch 5. A supplementary video

shows the complete image sequence of the pump pulse and THz fields obtained from the experiment alongside theory.

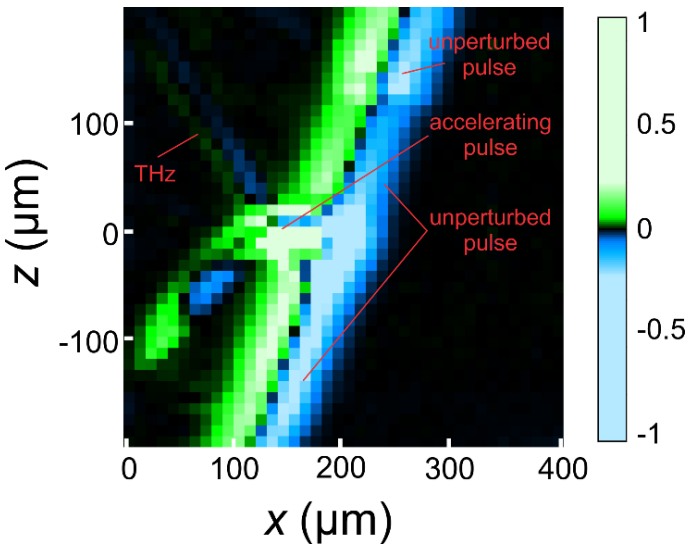

Figure 2.18. Unprocessed image obtained from the orthogonal pump probe measurement for a probe delay of t = 1.76 ps. Processing of the images for each probe delay involved the removal of the unperturbed transmission and then isolating the signals associated with the 800 nm accelerating pump pulse and THz synchrotron radiation.

CHAPTER 3
A WAVELENGTH-SIZED THZ SPECTROMETER BASED ON EXTRAORDINARY TRANSMISSION

"If you can't take a little bloody nose, maybe you ought to go back home and crawl under your bed. It's not safe out here. It's wondrous, with treasures to satiate desires both subtle and gross. But it's not for the timid."

- Q to Captain Jean-Luc Picard in *Star Trek the Next Generation*

This chapter consists of many excerpts of work which has been published in [61]. This project was carried out in collaboration with Jing Zhou, who, at the time, was a postdoctoral fellow of L. Jay Guo in the Electrical Engineering and Computer Science Department at the University of Michigan. Jing performed the fabrication of the slotted plate structures. Both, Prof. Guo and Jing often initiated incredibly insightful discussions concerning this project.

3.1. A Brief Introduction to Extraordinary Transmission

When an electromagnetic wave is incident upon an interface or an obstacle, the ratio of the total power transmitted P_T to the total incident power P_I is defined as the transmission T:

$$T = \frac{P_T}{P_I} \quad (3.1)$$

In the case when the radiation is incident upon an aperture in a conducting screen, it can be useful to define transmission in terms of the incident power P_A that impinges over only the area of the aperture. A precise determination of P_A involves integrating the intensity distribution of the incident beam over the area of the aperture. However, it is often sufficient to define P_A as:

$$P_A = \frac{P_I}{Beam\ Area} \times Aperture\ Area \quad (3.2)$$

This allows us to now define the area-normalized transmission T_N as:

$$T_N = \frac{P_T}{P_A} = T \times \frac{Beam\ Area}{Aperture\ Area} \quad (3.3)$$

In 1944, Hans Bethe showed that when electromagnetic radiation of wavelength λ is incident upon a single aperture of radius $a << \lambda$, T_N is tremendously small, scaling as a^4/λ^4 [62]. In 1998, a study reported observations of $T_N > 1$, for light incident on an array of sub-wavelength-sized holes in a metallic sheet [63]. The case of $T_N > 1$ is often referred to as *extraordinary* transmission, considering that the amount of power transmitted through the aperture exceeds the amount of power that is impinging upon the aperture itself.

Several mechanisms are known to facilitate extraordinary transmission. For the case of the aforementioned hole array depicted in Figure 3.1(a), the excitation of surface plasmon-polariton modes creates transmission enhancements at select frequencies [63], and a similar effect also occurs for metallic gratings with sub-wavelength slits [64]. For a single sub-wavelength slit embedded in a thick conducting plate (Figure 3.1(b)), the coupling to Fabry-Perot resonances allows for enhanced transmission at select frequencies [65,66]. In fact, this structure actually gives perfect transmission ($T = 1$), as discussed in the thesis of Steve Young, a graduate of the Merlin Lab [67]. Figure 3.1(c) shows theoretical results taken from [66] for a rectangular aperture

embedded in a perfectly conducting plate. The excitation of TE waveguide modes allows for transmission enhancements at the TE cutoff frequency.

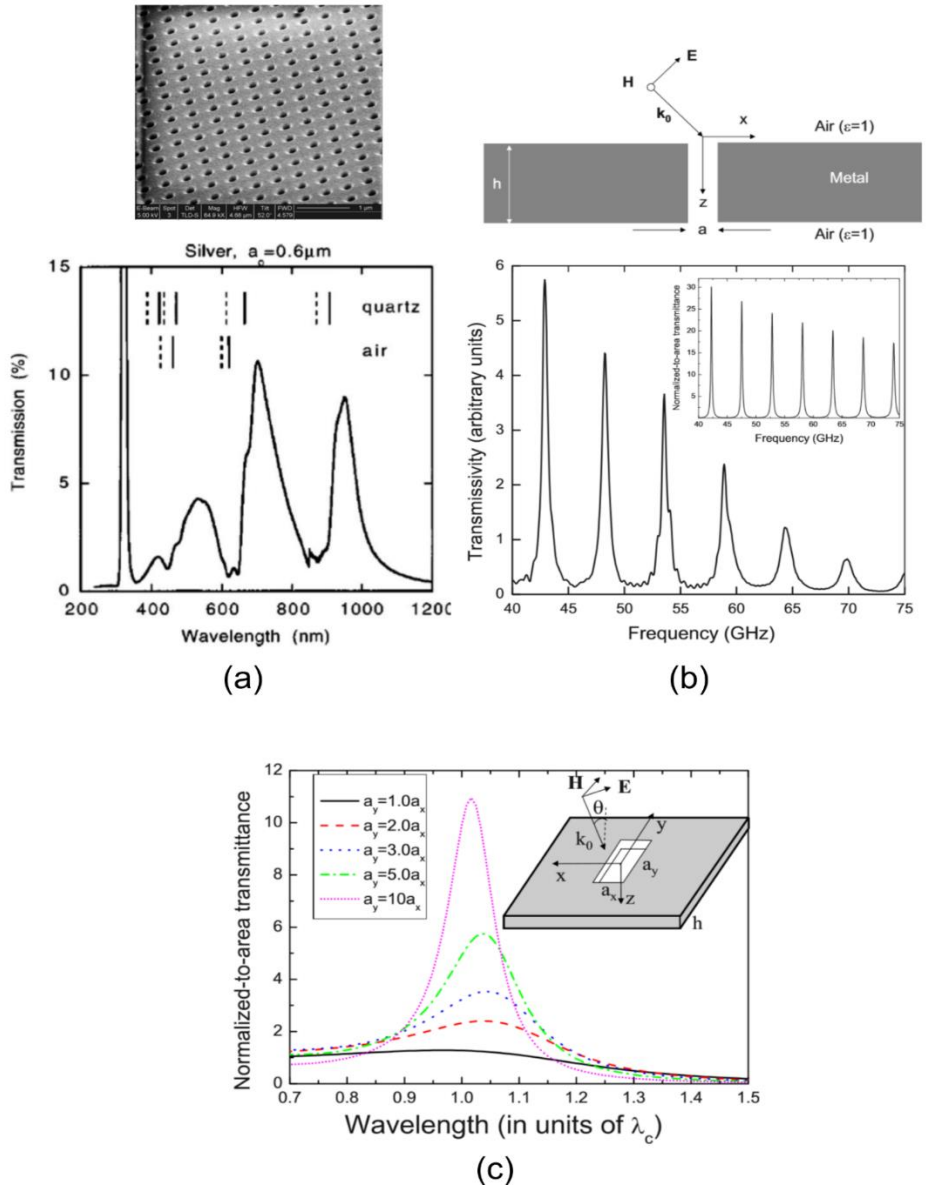

Figure 3.1. Structures shown to exhibit extraordinary transmission; figures are reproduced from [66]. (a) Measured area-normalized transmission (T_n) for an array of circular holes with diameters of 150 nm in a silver film on a quartz substrate. The coupling to SPP modes is responsible for enhanced transmission at the select frequencies. (b) Transmission measurements for a single slit of width 75 μm embedded in a metal plate of thickness 28.2mm. The transmission enhancements for p-polarized light are observed at the frequencies f_m of the Fabry-Perot resonances as determined by $f_m = mc/2h$, (m = 1, 2, 3). (c) Calculated T_n for a single rectangular aperture embedded in a perfectly conducting plate. Excitation of TE waveguide modes with a cutoff wavelength given by

$\lambda_c = 2a_y$ creates strong transmission enhancements for incident wavelengths $\lambda = \lambda_c$ in the case of $a_y \gg a_x$.

All of the aforementioned structures share a commonality in that the extraordinary transmission is exhibited at a few given frequencies which are determined by the coupling of the aperture(s) with a given mode or resonance. As such, these types of structures can be good candidates for spectral filters and spectrometers. In this chapter, I will present a structure which exhibits long-lived and tunable Fabry-Perot like resonances as a viable option for an on-chip THz spectrometer. I will then discuss some preliminary simulations and measurements on another structure that also has potential for THz filtering and spectroscopy applications.

3.3. Principles of the Slotted Waveguide

In this chapter, we show that a pair of parallel copper plates each containing a single sub-wavelength slit holds promise for the development of a highly-compact THz spectrometer. The principles of this structure are derived in [68], and a microwave realization was reported in [69]. As shown for the case of perfectly conducting plates [68], such a system shows an electromagnetic resonance at a frequency slightly below the transverse electric (TE) waveguide cutoff frequency $f_{cut} = c/2d$ where d is the plate separation. This resonance is supported by the slits, and unlike the extended fields of a parallel-plate Fabry-Perot spectrometer, its fields are localized within the plates. For a slit of width a, the frequency of the resonance f_{res} for $a << d$ is given by [68]:

$$f_{res} = (1 - \delta_r) f_{cut} \; ; \; \delta_r \ll 1 \quad (3.4)$$

where

$$\delta_r \approx \frac{\pi}{2}\left[\ln\left(\frac{1.781\pi a}{2\lambda}\right) + \frac{2(\lambda_{cut})^2}{\pi^2 a^2}\right]^{-2} \quad (3.5)$$

Considering that a negligible amount of radiation transmits through a single sub-wavelength-sized aperture [62,68], this aperture-bound resonance is remarkable in that it gives perfect transmission in the absence of conduction losses. For a perfect metal, the resonance quality factor (Q) is determined solely by the radiative losses from the slits, which scale as $Q \propto (\pi\lambda/a)^6$ for the TE configuration [68]. Figure 3.2(a) shows results of finite element method (FEM) simulations for perfectly conducting plates.

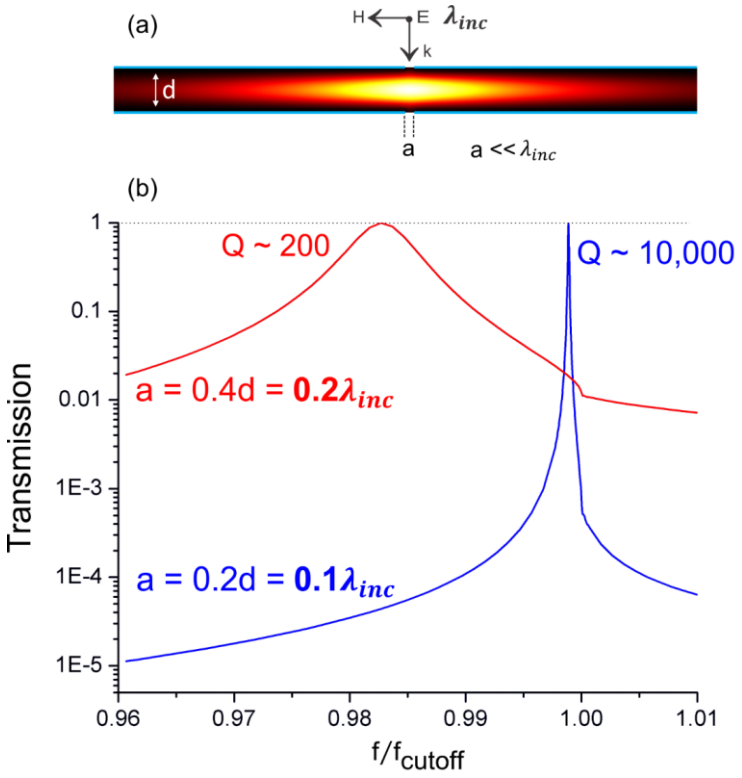

Figure 3.2. (a) Contour plot showing the bound resonance of a pair of perfectly-conducting sub-wavelength-slotted plates when illuminated by TE polarized light. (b) Results for $a = 0.2\lambda_{inc}$ and $a = 0.1\lambda_{inc}$ for perfectly conducting plates. The cusp observed at the waveguide cutoff ($f = 1$) is a result of a Fano interference between the waveguide continuum and the bound resonance.

Higher-order resonances supported by the slits also exist at frequencies near integers of the fundamental Fabry-Perot resonance. However, their coupling to the waveguide continua does not

allow for perfect transmission. We note that these aperture-supported resonances are not excited in the transverse-magnetic (TM) - polarized configuration, for which the transmission spectrum is defined by broad peaks at the Fabry-Perot resonant frequencies [68,65].

3.4. The Slotted Waveguide THz Spectrometer: Design, Simulation, and Results

Our slotted waveguide spectrometer consists of two polymethylpentene (TPX) substrates each containing a copper slotted plate; see Figure 3.3. The slits' width was set at 40 μm because simulations predicted resonance quality factors (Q) greater than 100 and reasonable power transmission (0.01 – 0.1) at frequencies near the peak response of our THz-TDS system, at 1 THz. Samples were fabricated using a thermal evaporator to deposit a 1 μm layer of copper onto the substrates. The deposition was performed while a shadow mask, shaped into the complement of the slotted plate, was attached to each substrate. By mounting the resulting samples onto linear translation stages, we constructed a copper slotted waveguide with an adjustable air gap. An angular kinematic mount was used to achieve parallel alignment.

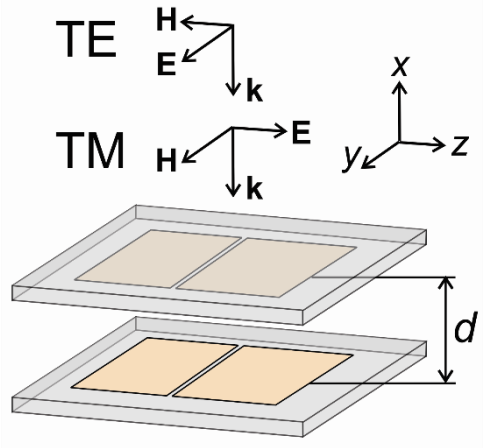

Figure 3.3. Schematic diagram describing the slotted plates. The slits' width is ≈ 40 μm. The plates' dimensions are 5 mm × 7 mm. The thickness of the substrates is 2 mm.

Finite element method calculations were carried out using the software COMSOL 3.5a. In one set of calculations, we consider an incident cylindrical Gaussian beam and solved the two-dimensional (2D) Helmholtz equation using the actual parameters of our Cu-plate structure. The response of the copper was modeled using the Drude formula for the permittivity

$$\epsilon(\omega) = -\frac{\sigma_0 \tau}{\varepsilon_0} + i\frac{\sigma_0}{\varepsilon_0 \omega} \quad (6)$$

with $\sigma_0 = 59.6 \times 10^6$ S/m and $\tau = 25$ fs; this approximation works particularly well in the THz range [53]. We also performed three-dimensional (3D) simulations assuming perfectly conducting plates to account for the finite size of, both, the plates and the illuminated area. Results of the 2D calculations are reproduced in the contour plots of Figure 3.4. TE transmission data is shown in Figure 3.4(a) and (c) for, respectively, the fundamental frequency and the first overtone. Note the field profile between the plates revealing the localized nature of the electromagnetic resonances [68,69]. The corresponding TM plots show the transmission that results from excitation at the corresponding waveguide cut-offs.

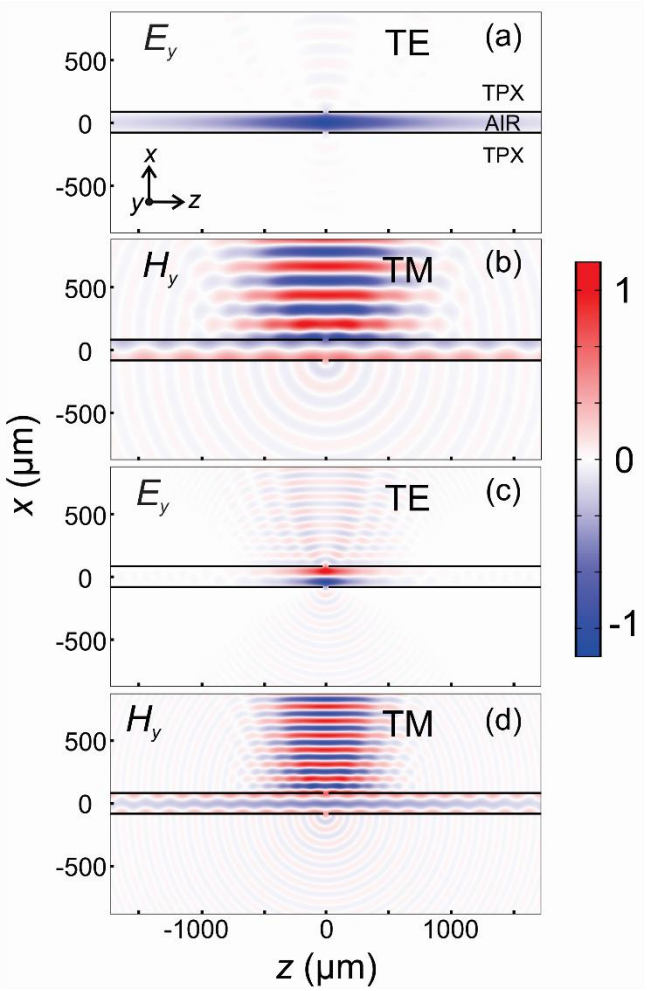

Figure 3.4. Contour plots showing calculated TE and TM field amplitudes at a plate separation of 167μm. The frequencies are (a) ν_{TE1} = 0.8953 THz. (b) ν_{TM1} = 0.8970 THz. (c) ν_{TE2} = 1.778 THz. (d) ν_{TM2} = 1.795 THz.

We measured the transmission of both TE and TM polarized radiation for various plate separations using a THz-TDS setup; see Figure 3.5. THz pulses were generated by focusing the output of a Ti:Sapphire oscillator, tuned to 815nm with a repetition rate of 82MHz, onto a biased photoconductive emitter modulated at 15 KHz. Using parabolic reflectors, the emitted THz pulse was focused onto the slotted plates. The radiation transmitted through the structure was spatially overlapped with a separate near-IR probe pulse from the oscillator, and then focused onto a (110) ZnTe crystal for detection via electro-optic sampling. A mechanical delay line was used to control

the arrival times of the THz and probe pulses at the crystal. The path of the THz radiation was sealed inside a plexiglass enclosure filled with nitrogen gas in order to eliminate absorption by water vapor. Theoretical details of THz-TDS are discussed in Section 2.2.

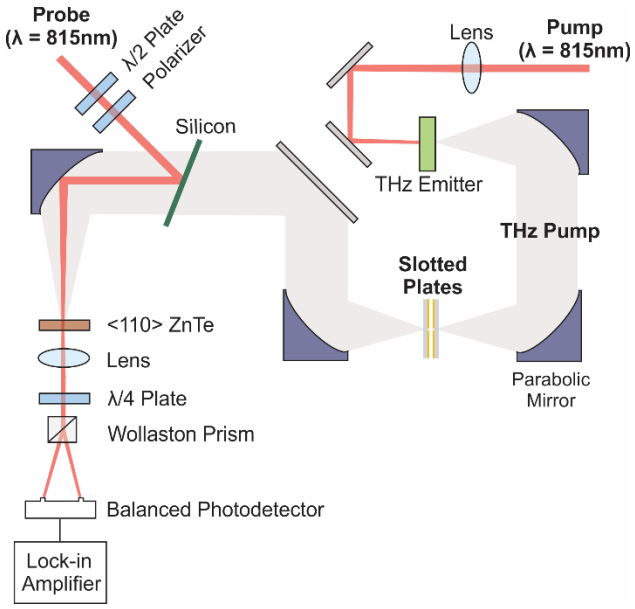

Figure 3.5. THz-TDS System. For details concerning theoretical aspects of the setup, see section 2.2

Figure 3.6(a) and 3.6(b) show experimental THz-TDS traces at a plate separation d = 140 μm and the simulated transmission of the reference THz pulse through the slotted plates at d = 139 μm for the TE and TM geometry, respectively. The experimental plate separations were obtained from the measured resonant frequencies using the Fabry-Perot condition $d = mc/2f_m$ where f_m is the frequency of the resonance of order m and c is the speed of light in vacuum. Theoretical transmission traces were obtained by first fitting the calculated spectra to a sum of lorentzians and then using the fit parameters to generate the temporal traces, after convolution with the reference pulse. Figure 3.6(c) shows the Fourier spectra for both polarizations. Frequency spectra were gained from the experimental time-domain data using a linear prediction method [70,71], which

relies on a singular value decomposition to fit the measured electric field, shown in Figures 3.6(a) and (b), to a sum of decaying sinusoids. These fit parameters were then used to obtain the corresponding Fourier spectra. Since the oscillations extend beyond the measured time window of 15.5 ps, this method is more accurate than a simpler fast Fourier transformation of the traces. The spectrum generated by linear prediction was then normalized to the spectrum of the reference pulse, which we obtained by using a fast Fourier transform.

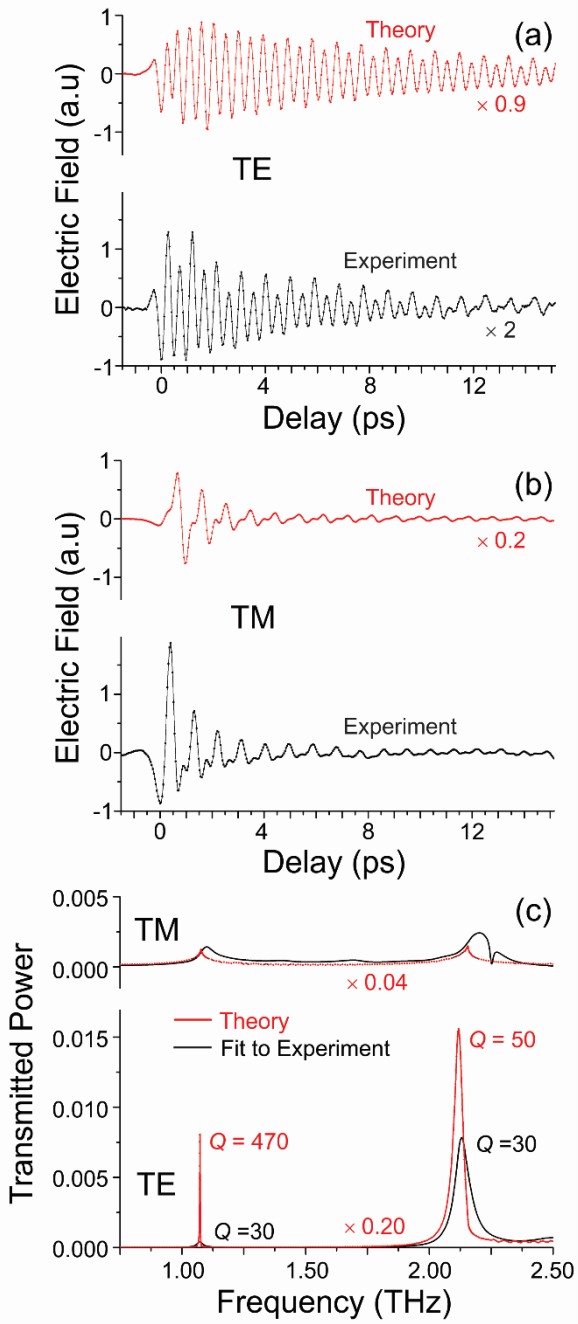

Figure 3.6. Calculated (plate separation d = 139 μm) and measured (d = 140 μm) THz-TDS traces for the TE (a) and TM (b) geometry. The corresponding power spectra are shown in (c).

In Figure 3.7, measured TE spectra are shown for four different plate separations. The peaks have contrasts in the range 10^2-10^3 and their full-width at half maximums (FWHM) are

1 – 2 cm^{-1}. We note that the quality factor increases with plate separation up to ≈ 170 μm, in agreement with simulations. The ulterior decrease observed at larger separations (see the 195 μm trace) is attributed to a slight misalignment in the slotted plates, the effect of which becomes more detrimental with decreasing frequency (see discussion below). We note that Q = 470 at 1.1 THz (simulation, Figure 3.6(c)) corresponds to a FWHM of 0.08cm^{-1}, which is comparable to the resolution of state-of-the-art FTIR systems. For instance, the SPS-300 system (Sciencetech Inc.) has a standard spectral resolution of 0.12cm^{-1}, with a high resolution capability of 0.02cm^{-1}. Thus, the potential of the structure to select a narrow frequency band combined with the evident ability to tune the peak frequencies with plate separation sets our structure as a viable wavelength-size THz spectrometer.

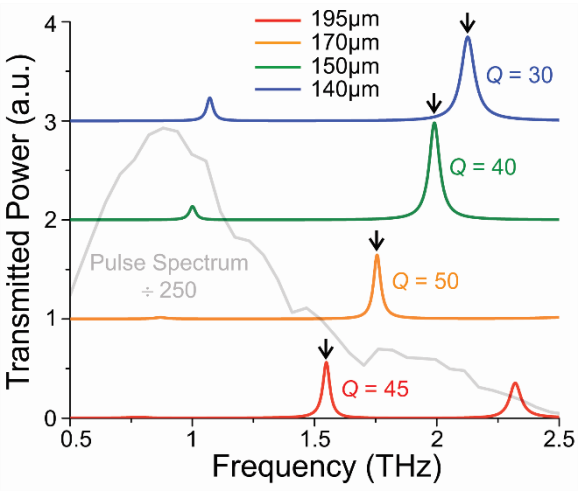

Figure 3.7. Measured TE transmission spectra for various plate separations. Arrows denote the second-order resonance.

The comparison between theory and experiment shows that there are large differences between the calculations and measurements of the peak power transmission. We ascribe these differences to losses associated with the finite size of both the structure and the incident illumination profile.

This assignment is supported by the 3D simulations, which consider a Gaussian beam focused onto a perfectly conducting slotted waveguide. The length of the plates along the slit and the size of the incident beam were the same as those used in the experiments. These simulations give a factor of ~ 5 (~ 25) decrease in the power transmission for the TE (TM) polarization when compared with an infinite structure. Multiplying the power spectra and field amplitudes from the calculations by the respective factors yields peak transmission values that agree reasonably well with the data, as shown in Figure 3.6.

The considerable differences between the measured and theoretical quality factors in Figure 3.6(c) are attributed mainly to imperfect parallel alignment of the plates. Long-lived resonances have fields that extend farther throughout the plates compared to those of shorter-lived resonances and, as such, the plate alignment is more critical for their observation. The localization lengths of the fields can be seen Figure 3.4(a) and (c). 2D simulations show that a deviation as small as 0.1^{o} from parallel alignment decreases the quality factor of the first order resonance (Q = 470) and its peak transmission by factors of 1.7 and 3.5, respectively, whereas the second order resonance (Q = 50) was minimally affected. Increasing the offset angle to 1^{o} reduces the lifetime of the first order resonance by a factor of ~ 10 and its peak transmission by a factor of ~ 20. The reduction in, both, the peak transmission and Q was less than a factor of 1.5 for the second order resonance. Additional results are shown in Figure 3.8.

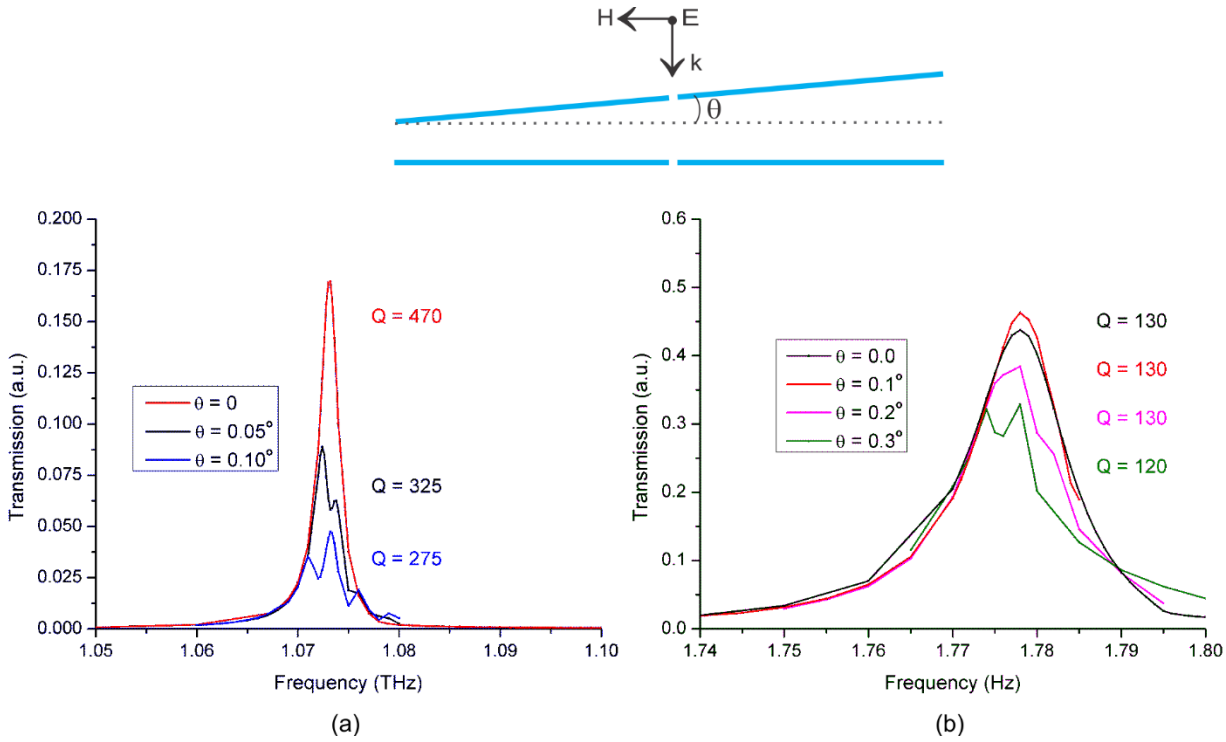

Figure 3.8. FEM simulations of imperfect plate alignment. (a) First order resonance, plate separation = 139 μm. (b) Second order resonance, plate separation = 167 μm. Higher Q resonances are considerably more affected by imperfect plate parallelism since their fields have a greater spatial extent throughout the plates.

3.5. Perfect Transmission Through a Pair of Perfectly Conducting Plates Each Containing a Sub-Wavelength Pinhole

FEM simulations of the transmission of light through a pair of perfectly conducting plates which each contained a circular sub-wavelength aperture were performed. The plates were separated by a distance *d*, and the apertures both had a diameter of $w \ll \lambda_{cut}$, where $\lambda_{cut} = 2d$ is the waveguide cutoff. Results show that this structure exhibits perfect transmission due to a bound resonance at frequency $f = f_{res} = (1 - \xi) f_{cut}$ where $\xi \ll 1$. Unlike the problem with the slotted plates, there is no known analytical solution for the fields transmitted through this structure. Figure 3.9 shows a schematic of the structure and results of the FEM simulations.

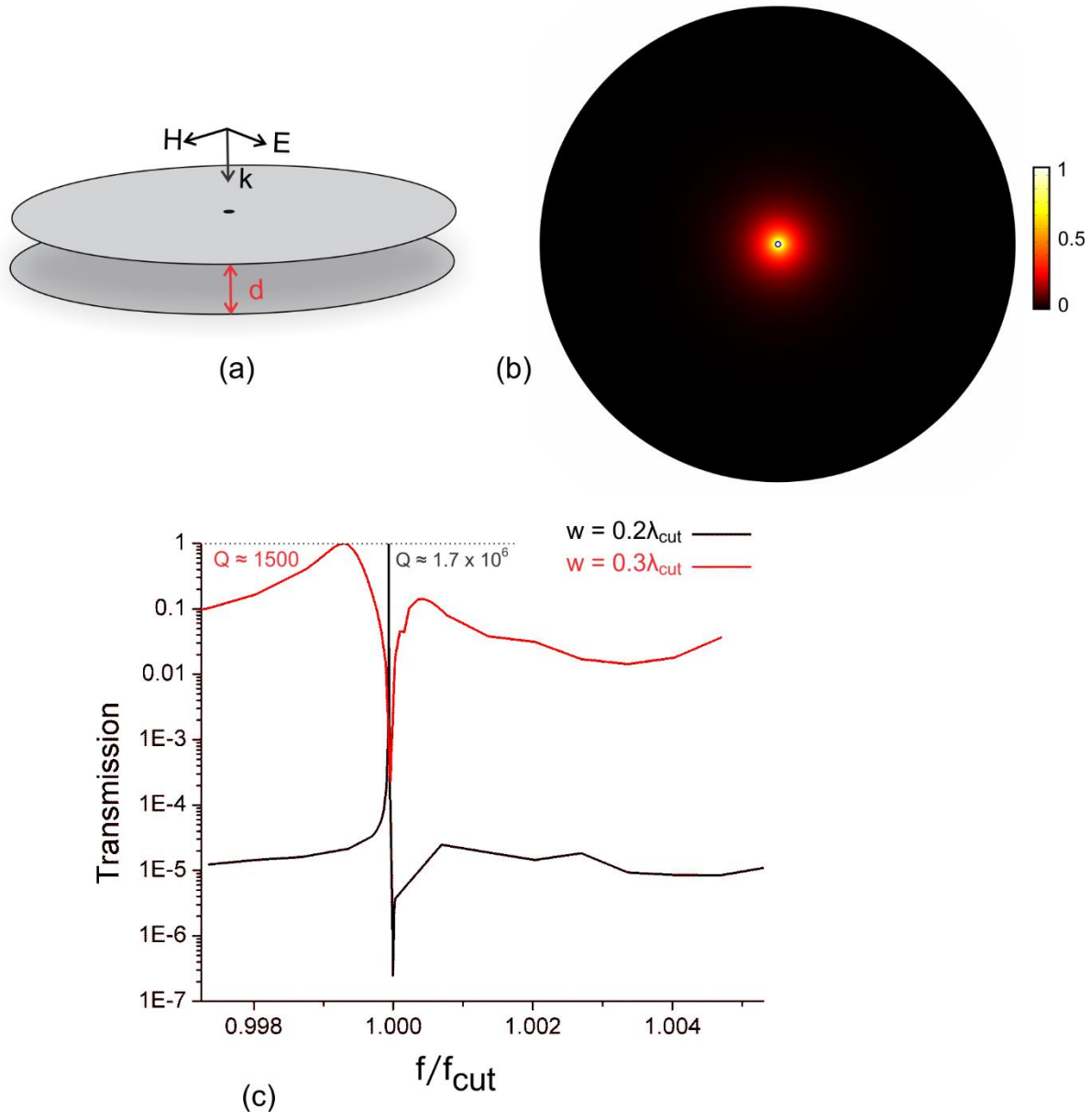

Figure 3.9. (a) Description of the problem: linearly polarized light impinges upon a pair of perfectly conducting plates which each contain a circular aperture of diameter $w \ll \lambda_{cut}$. (b) Contour plot of the field between the plates when illuminated with linearly-polarized light of frequency of $f = f_{res}$. Here, $w = 0.3\lambda_{cut}$. (c) Power transmission spectra obtained from FEM simulations for the cases of $w = 0.3\lambda_{cut}$ and $w = 0.2\lambda_{cut}$. Perfect transmission is observed.

Similar to the case of the perfectly conducting slotted plates, the quality factor is defined solely by the radiative losses from the aperture, resulting in significantly greater quality factors for smaller apertures.

3.6 THz-TDS Experiments on a Pair of Copper Plates Each with a Sub-Wavelength Pinhole

THz-TDS measurements were performed on a pair of thin copper plates which each contained a pinhole of 100 μm diameter. For an incident frequency of 1 THz ($\lambda = 300$ μm), this corresponds to a diameter of 0.33λ. The plates were custom-purchased from Lenox Laser, and the thicknesses of the copper were specified to range between 12 μm and 18 μm. Using a vacuum pen, the plates were gently placed onto two separate aluminum mounts which each contained a thin layer of adhesive. The mounted plates were then installed into the setup shown in Figure 3.5, and transmission measurements were performed for several values of the plate separation *d*. Results are shown in Figure 3.10. Unfortunately, I was unable to obtain FEM results to compare with the measurement. Both, the finite conductivity and thickness of the plates created a problem far too large to solve on a desktop computer, and the HPC cluster at the University of Michigan did not support Comsol at the time of these studies. Thus, solving such a problem serves for future work.

When obtaining the Fourier spectrum, I simply applied a fast Fourier transform (FFT) to the data rather than the linear predictive methods used for the work on the slotted plates. As seen in Figure 3.10(b), there is a spurious low frequency (0.1 – 0.2 THz) signal in the data, and I found that the linear prediction code struggled to fit this. Since the oscillations continue beyond the scan range, the peak width is certainly not resolved by the FFT. However, the point here is to show some experimental validation of the bound resonances predicted by the results shown in Figure

3.9. Based on the FEM results presented for the slits, these resonances are also likely highly sensitive to plate parallelism.

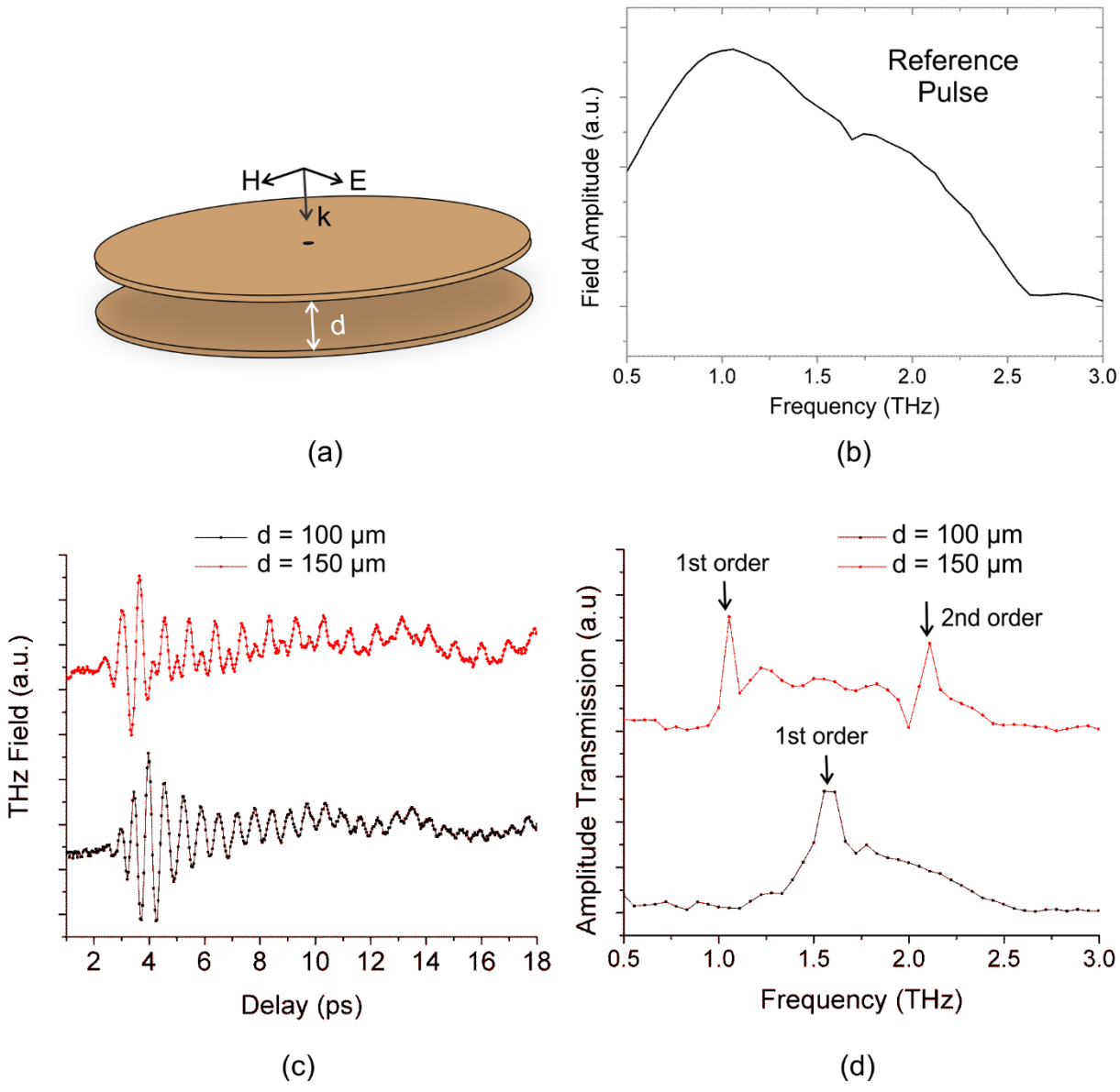

Figure 3.10. THz-TDS measurements on two copper plates each with a pinhole of diameter w = 100 μm separated by an air gap of length d. (a) Schematic describing the structure. (b). Spectrum of the reference pulse used in the measurement. (c). THz-TDS traces for d = 100 μm and d = 150 μm. (d) FFT of the data presented in (c). The peak widths are not resolved; however, the results serve as experimental evidence of the existence of bound resonances.

3.7. Summary

We demonstrated the principles of a sub-wavelength slotted waveguide at THz frequencies by measuring both the TE and TM response of a copper test structure with THz-TDS. We have shown that our structure works as a highly-compact THz spectrometer, and have identified plate parallelism as the main obstacle to ideal performance. In addition, I presented simulations which show that a pair of perfectly conducting plates each with a sub-wavelength-sized pinhole exhibits bound resonances similar to those of the slotted plates and perfect transmission at the resonance frequencies. I verified the existence of these resonances using THz-TDS experiments on a pair of copper plates. In the case of the pinholes, simulations of a structure with finite conductivity and thickness still needs to be accomplished. The next step for experimental work in both cases involves developing methods for achieving near-perfect ($\theta < 0.1$ degrees) parallelization of the plates in order to measure longer-lived resonances.

CHAPTER 4
ACCELERATING LIGHT WITH METASURFACES

"For that one fraction of a second, you were open to options you had never considered. *That* is the exploration that awaits you. Not mapping stars and studying nebula, but charting the unknown possibilities of existence."

- Q to Captain Jean-Luc Picard in *Star Trek: The Next Generation*

This project was carried out in collaboration with Carl Pfeiffer, who completed his thesis under the mentorship of Anthony Grbic in the Electrical Engineering and Computer Science Department at the University of Michigan, and Di Wang, who is currently a student of Vladimir Shalaev and also Alexandra Boltasseva, both of whom are professors in the School of Electrical and Computer Engineering at Purdue University. Carl carried out the metasurface design, and Di performed the fabrication of the metasurface. Several excerpts in this chapter are taken from a manuscript describing our work [72].

4.1. Accelerating Light Beams

Consider the 2D scalar Helmholtz Equation:

$$\left(\frac{\partial^2}{\partial x^2}+\frac{\partial^2}{\partial z^2}+k^2\right)E(x,z)=0 \quad (4.1)$$

where $k = 2\pi n/\lambda$ (n = 1 for vacuum). Upon transformation to polar coordinates, we get:

$$\left(\frac{1}{r}\frac{\partial}{\partial r}\left(r\frac{\partial}{\partial r}\right) + \frac{1}{r^2}\frac{\partial^2}{\partial \theta^2} + k^2\right)E(r,\theta) = 0 \quad (4.2)$$

Now, if we separate variables:

$$E(r,\theta) = E(r)E(\theta) \quad (4.3)$$

$$\left(\frac{\partial^2}{\partial r^2} + \frac{1}{r}\frac{\partial}{\partial r} - \frac{\beta^2}{r^2} + k^2\right)E(r) = 0 \quad (4.4)$$

$$\left(\frac{\partial^2}{\partial \theta^2} + \beta^2\right)E(\theta) = 0 \quad (4.5)$$

The general solution is:

$$E(r,\theta) = [C_1 J_\beta(kr) + C_2 N_\beta(kr)] \times [A_1 exp(i\beta\theta) + A_2 exp(-i\beta\theta)] \quad (4.6)$$

where $J_\beta(kr)$ is the Bessel Function of the first kind of order β and $N_\beta(kr)$ is the Bessel Function of the second kind (or Neumann Function) of order β. As is well-known, Neumann functions diverge at the origin, so we set C_2 = 0 and simply set C_1 = 1. Returning to Cartesian coordinates, the solution becomes:

$$E(z,x) = J_\beta\left(k\sqrt{x^2+z^2}\right)\left[A_1 exp\left(i\beta \times arctan\left(\frac{x}{z}\right)\right) + A_2 exp\left(-i\beta \times arctan\left(\frac{x}{z}\right)\right)\right] \quad (4.7)$$

Figure 4.1 shows the intensity $|E(z,x)|^2$ for $\beta = 393$, $\lambda = 800$ nm, and n =1.

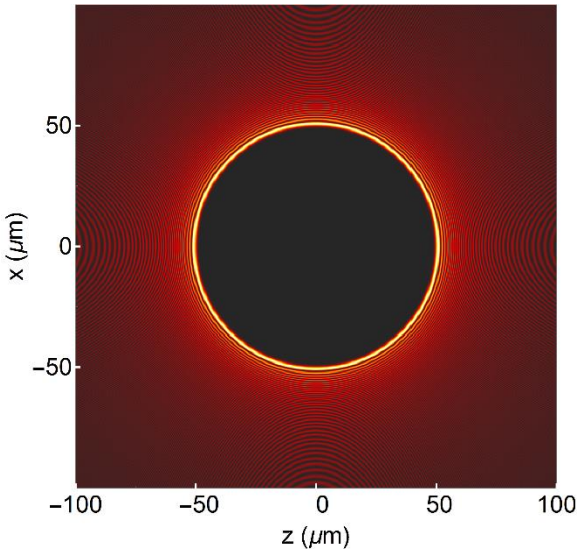

Figure 4.1. Plot of the intensity $|E(z,x)|^2$ associated with eq. (4.7) for n =1, $\beta = 393$, and $\lambda =$ 800 nm. The radius of curvature is R = β/k = 50 μm.

Thus, this solution to the Helmholtz Equation describes a beam that propagates indefinitely along a circular trajectory. The radius of curvature is given by $R = \beta/k$. As can be seen in the phase term of eq. (4.6) or eq. (4.7), the general solution has fields that propagate in both the clockwise and counterclockwise directions. Another essential feature to note is that the Bessel function decays as $1 / (x^2 + z^2)^{1/4}$, which means that the integral of the square of the Bessel Function diverges (or rather, the Bessel Function is not "square-integrable"). Given the formula for electromagnetic energy density:

$$u = \frac{1}{2}(\boldsymbol{E} \cdot \boldsymbol{D} + \boldsymbol{B} \cdot \boldsymbol{H}) \quad (4.8)$$

This means that the amount of energy associated with eqns. 4.6 and 4.7 is infinite, and thus these solutions are not physically-realizable. This is true for all diffraction-free solutions.

Although we can't create in the lab the exact beam shown in Figure 4.1, we *can* generate beams with finite energy that propagate along partial circular trajectories. We accomplish this by introducing a truncated version of the Bessel function. Using the (z,x) coordinate system of Figure

4.1, we designate the field at the center of the circular arc ($z = z_0$) to be the so-called half-Bessel beam [73]:

$$E_{fin}(z_0, x) = exp[\alpha x] J_\beta[-kx + \beta]\Theta\left[-x + \frac{\beta}{k}\right] \quad (4.9)$$

where Θ is the Heaviside function, and α is the truncation parameter for J_β. To find the finite-energy accelerating beam solution $E_{fin}(z, x)$ for arbitrary (z, x) , we use a reverse-propagation method that is presented in detail in section 4.2. A contour plot of $\left|E_{fin}(z, x)\right|^2$ is shown in Figure 4.2(a). Here, the light is incident from the z = 0 plane and is focused into a circular arc, the center of which is located at $z = z_0 = 100$ μm. For $z \gtrsim 150$ μm, the beam diffracts. These are the type of solutions that we focus on generating in this work.

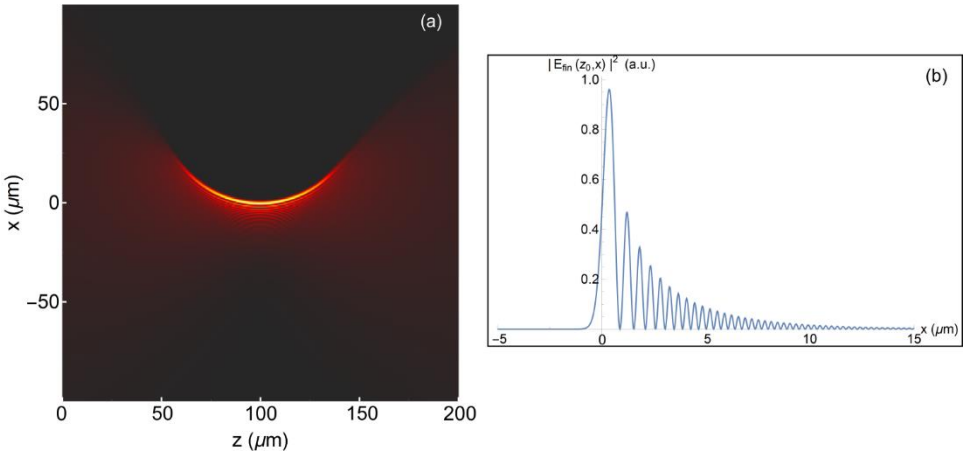

Figure 4.2. (a) Plot of $\left|E_{fin}(z, x)\right|^2$ for a beam with a radius of curvature of 100 μm. Here, z_0= 100 μm, $\alpha = 0.0625$ μm^{-1}, β =393, and λ = 800 nm. (b) Plot of $\left|E_{fin}(z_0, x)\right|^2$

It should be noted that there are several other accelerating solutions to Maxwell's Equations. The first reported solutions were Airy solutions which were shown to exist for the two-dimensional Helmholtz equation (HE) under the paraxial approximation [74]. Their finite-energy realization [75], which was accomplished by using a technique similar to the one above, was the

first demonstration of accelerating light. Subsequently, several other accelerating solutions, including the ones discussed above, have been discovered and realized in practice [76-80]. Some of these solutions are shown in Figure 4.3. It is important to distinguish these accelerating, non-diffractive solutions from the non-diffractive and non-accelerating Bessel and Mathieu beams, which propagate along straight lines [28-30].

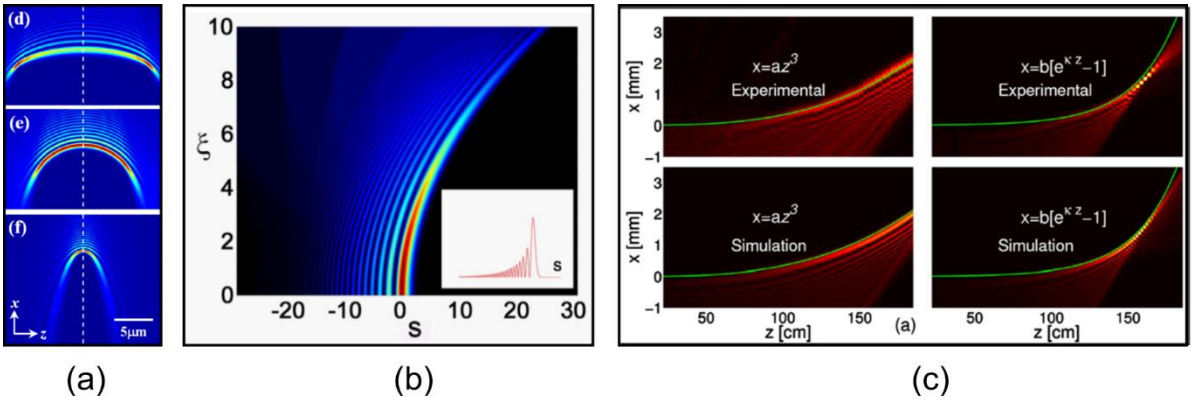

Figure 4.3. Examples of accelerating solutions to Maxwell's equations other than Bessel function solutions. (a) Mathieu beams: solutions to the Helmholtz Equation (HE) when transformed to an elliptical coordinate system, figure taken from [77]. (b) Finite-energy Airy beam; a solution to the HE in the limit of the paraxial approximation, figure taken from [75]. (c) Accelerating beam solutions derived from caustics theory, figure taken from [81].

4.2. Current Methods for Generating Accelerating Beams

The most common method for generating accelerating beams involves using a spatial light modulator (SLM) [73,75,77], although other techniques using phase masks [37,38] and lens aberrations [82] have been demonstrated. SLMs, in particular, are highly limited in their ability to bend light at steep angles because of the large size of their pixels. For light of 800 nm wavelength at normal incidence, the first-order diffraction angles of commercial SLMs range from ≈ 1° to ≈ 15° at best. For instance, the spacing *a* between the centers of two adjacent pixels is either 20 μm or 12.5 μm for the LCOS-SLM models made by Hamamatsu, and 6.4 μm and 3.74 μm for,

respectively, the LETO and GAEA 4K SLMs made by Holoeye Photonics AG. For 800 nm light normally incident upon a slit array of period $d = 2a$, the corresponding first-order diffraction angles are < 7°. Also at 800 nm, the linear series SLM made by Meadowlark Optics have a 1.6 μm pixel spacing, which gives a first-order diffraction angle of nearly 15°.

The problems which result from being unable to bend light at steep angles is illustrated in Figure 4.4. Figure 4.4 (a) shows the intensity of an accelerating beam with a radius of curvature of 100 μm. The interface at which light of normal incidence bends to create the given beam is located at $z = 0$. By inspection, we can see that the light at the interface must bend at a wide range of angles spanning from at least -45° to 45° in order to construct this beam. In other words, the incident light beam must have transverse wavenumbers k_x that span a range of *at least* $k_x = \pm\frac{2\pi}{\lambda}\sin(45)$. We can get a more quantitative picture of the range of transverse wavenumbers required by looking at the magnitude of the Fourier spectrum $E_{fin}(k_x)$ which is found by taking the 1D Fourier Transform over the *x* coordinate:

$$E_{fin}(z, k_x) = \int E_{fin}(z, x) e^{-ikx}\, dx \quad (4.10)$$

For light beams accelerating in vacuum or in a lossless medium, the amplitude spectrum of transverse wavenumbers is invariant of the z-coordinate. Figure 4.4(b) shows a plot of $\left|E_{fin}(z, k_x)\right|^2$ corresponding to the solution in (a).

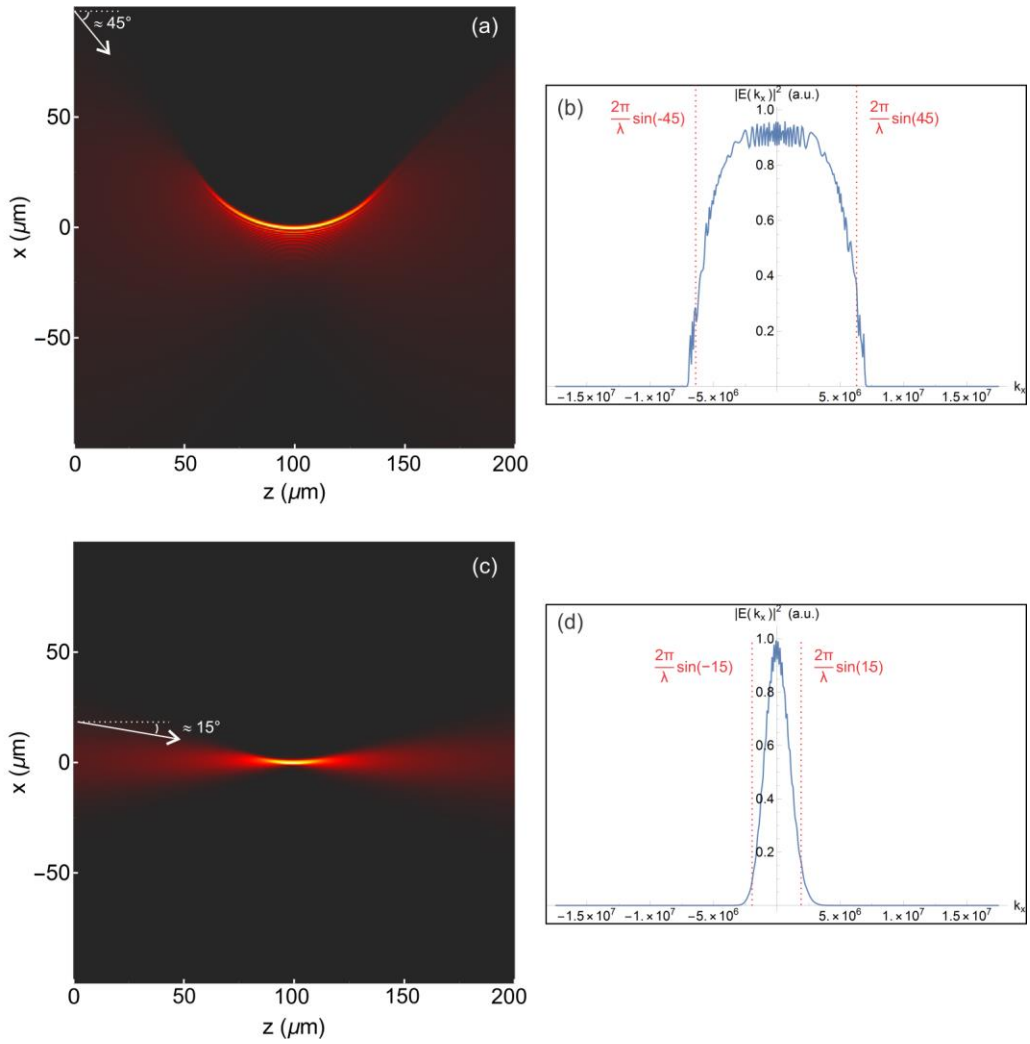

Figure 4.4. (a) The intensity of a beam accelerating in vacuum with parameters R = 50 μm, $\alpha = 0.0625\ \mu m^{-1}$, β =393. To generate such a beam, the light must bend at angles of at least 45°. This can also be seen by looking at (b), the spectrum of transverse wavenumbers k_x. (c) The result of removing the transverse wavenumbers which correspond to bending angles greater than ≈ 15° and (d) the corresponding spectrum of k_x.

Figure 4.4 (c) shows how the solution in (a) transforms when the transverse wavenumbers corresponding to bending angles greater than ≈ 15° are removed. The length of the arc followed by the intensity maximum is considerably less; the solution reduces to a function that resembles that of an ordinary Gaussian beam. This can also be seen in (d), as the spectrum of transverse wavenumbers becomes narrower and appears to resemble a Gaussian distribution. Thus, it is

necessary to be able to bend light at steep angles in order to generate highly circular beams, of any radius. Therefore, when using an SLM to generate accelerating beams, additional lenses must be used to bend the diffracted light at the necessary angles. At a minimum, this extends the size of the setup to many centimeters, preventing the use of accelerating beams for sub-centimeter-sized and on-chip systems. Phase masks have a similar constraint, as the corresponding accelerated-beam setups require additional optics [37,38]. Another limitation, common to all of the aforementioned approaches, arises when an application requires accelerating light inside a material, since Snell's law constrains the ability of light incident from free space to bend at steep angles. The maximum angle at which the light can bend inside a material of index of refraction *n* is given by:

$$\theta_{max} = sin^{-1}\left(\frac{1}{n}\right) \quad (4.11)$$

For glass (n =1.45), $\theta_{max} = 44°$ and for diamond (n = 2.4), $\theta_{max} = 25°$. For nonlinear crystals such as ZnTe and GaP which have $n \sim 3$, $\theta_{max} = 19°$. Standard water and oil immersion optics used to reduce index mismatch add considerable complications to the setup and are less-effective for higher index materials. Thus, in addition to their large size, current setups become further difficult to implement when attempting to accelerate beams in materials, especially in those with high values of the refractive index.

4.3 The Metasurface Approach to Accelerating Light

Here, we demonstrate a broadly applicable, planar optic approach for the acceleration of light inside a material using metasurfaces. The sub-wavelength size and spacing of the metasurface constituents allows for the bending of light at arbitrarily high angles in any medium, lifting the

constraints of conventional optics and eliminating the limitations associated with the aforementioned setups. Metasurfaces have been used to manipulate light for a number of applications, some of which include near-field focusing [83], nonlinear light generation [84-86], ultra-thin holograms [87,88], invisibility cloaks [89], and negative refraction [90,91]. Until now, the metasurface approach has yet to be used for the acceleration of light.

Our metasurfaces consist of gold V-shaped nanoantennas [90,91]. In contrast to dielectric metasurfaces, which often require harsh chemical etches [92] or time-consuming and expensive atomic layer deposition processes [93], the fabrication process for the nanoantennas is easily optimized and can be used on a wide-variety of substrates, making large-scale fabrication for on-chip applications considerably more feasible. Furthermore, dielectric metasurfaces typically have larger unit cell sizes [92,93] which can impose limitations when generating beams with high numerical apertures inside materials.

The nanoantennas are characterized by their arm length L and the angle between the arms, Δ; see Figure (4.5a). These antennas exhibit two so-called symmetric and antisymmetric resonances at, respectively, $\lambda_{eff} \approx 2L$ and $\lambda_{eff} \approx 4L$, where λ_{eff} is an effective wavelength which depends on the vacuum wavelength, the plasma frequency, the antenna cross section, and the surrounding medium [94]. Excitation of the symmetric or antisymmetric resonance alone occurs when the incident field is polarized respectively along the principal S or AS axis, which are perpendicular to each other; see Figure (4.5a). In both cases, the scattered field is polarized along the same direction as that of the incident field, and the scattering phase shift depends on both L and Δ. Because of their large bandwidth [91], both resonances can be simultaneously excited with monochromatic light if the excitation field is polarized along directions other than those of the principal axes. The resulting scattered field has polarization components both perpendicular

(cross-polarized) and parallel to the incident beam. We designed a set of antennas that operates for incident fields of wavelength 800 nm polarized at 45° with respect to both the principal axes. Central to our design is the fact that the phase shift for the cross-polarized configuration can be varied from 0 to π by tuning L and Δ, and a total of 2π phase coverage can be achieved by rotating each antenna in the designed set by 90 degrees [90].

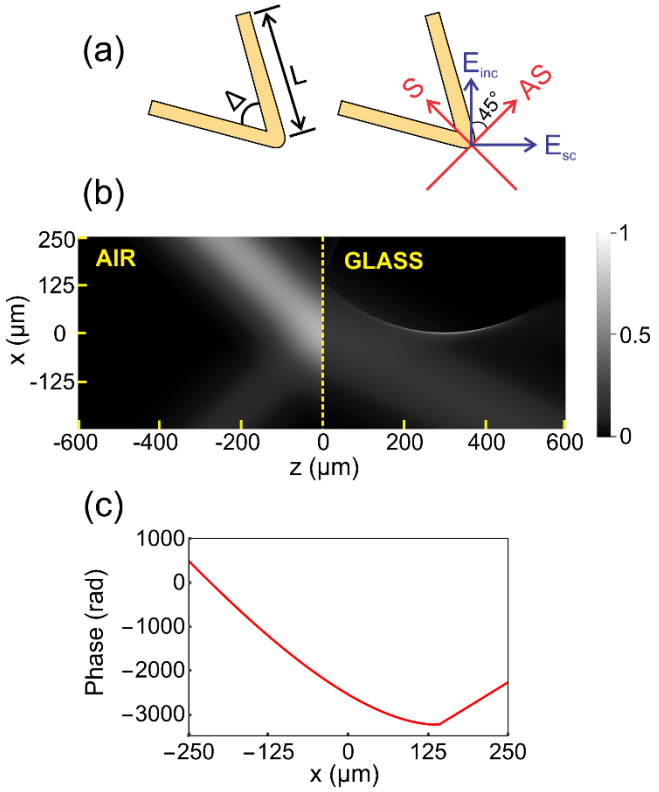

Figure 4.5. (a) Nanoantenna geometry. Incident light polarized at 45° relative to the orthogonal symmetric (S) and antisymmetric (AS) axes results in the excitation of both antenna modes and a cross-polarized scattered field. (b) Two-dimensional contour plot showing the calculated light intensity before and after traversing the metasurface at $z = 0$. Illumination at 45° allows for spatial separation of the unperturbed and the accelerating beam, which is readily observed at $z > 0$. (c) Calculated phase shift produced by the metasurface. The discontinuity in the phase gradient near $x = 135$ μm has a very minor effect on the beam properties

We simulated the scattered field of each antenna under the local periodicity approximation (LPA) [95], which assumes that the response of a single v-antenna is the same regardless of whether it is surrounded by antennas with identical or slightly differing parameters. The LPA assumption was tested by simulating the response of an array designed to refract normally incident light at an angle of 52 degrees. We found that the amount of cross-polarized power transmitted in the desired direction was 40 times greater than for other directions.

The metasurfaces were configured to produce an accelerating beam inside a glass substrate upon illumination with light incident at an angle of 45° from the normal to the glass-vacuum interface. The nanoantennas scatter ~ 5% of the incident power into the cross-polarized accelerating beam whereas ~ 20% of the incident power is reflected. Approximately 50% of the incident power passes through the metasurface unperturbed and is refracted inside the glass according to Snell's law. As illustrated in Fig. 4.5(b), illumination at 45° allows for the spatial separation of the accelerating and unperturbed transmitted beams.

The nanoantenna pattern was designed using back-propagation so that the electric field at the metasurface plane gives the proper field at a distance z_0 = 300 μm from the metasurface, when illuminated with light of frequency $\omega_0/2\pi = 3.75 \times 10^{14}$ Hz. We chose this field $E(z_0, x)$ to be the so-called half-Bessel beam discussed in section 4.1:

$$E(z_0, x) = \exp(\alpha x) J_\beta(-kx + \beta)\, \Theta\left(-x + \frac{\beta}{k}\right) \quad (4.12)$$

Again, z_0 is the coordinate of the accelerating beam center, α is a cut-off parameter, related to the truncation of $J_\beta(-kx + \beta)$, and $\beta = kR$, where $k = nk_0$ is the wavenumber inside the glass of index n, $k_0 = \omega_0/c$ is the wavenumber in vacuum, R is the predetermined radius of curvature of the accelerating beam, and Θ is the Heaviside step function. We use reverse propagation [83] to obtain the field at the metasurface plane (z = 0):

$$E(0,x) = A(0,x)\exp[i\varphi(0,x)] \; = \int G^{-}(z_0, x-x')^{-} E(z_0, x')dx' \quad (4.13)$$

where

$$G^{-}(z_0, x-x')^{-} = H_0^2\left[k\sqrt{{z_0}^2 + (x-x')^2}\right] \quad (4.14)$$

is the appropriate reverse-propagating Green's function for the 2D Helmholtz equation and H_0^2 is the 0th order Hankel function of the first kind. Our calculations show that the amplitude function $A(0,x)$ is approximately Gaussian across the metasurface plane. This allows for a design whereby the accelerating beam is generated solely by phase modulation of an incident Gaussian light source. To account for the angle of incidence of 45°, the phase shift at the metasurface plane must be $\varphi_m(0,x) = \; \varphi_r(0,x) + \varphi(0,x)$ where $\varphi_r(0,x) = k_0(\sqrt{2}/2)(x - \ell/2)$ and ℓ is the length of the metasurface along the *x*-axis. Based on these required phase shifts, the nanoantennas were arranged in a square lattice of spacing 220nm, forming a discretized version of $\varphi_m(0,x)$ on the metasurface plane. An example of a metasurface-induced phase shift is shown in Fig. 4.5(c). Upon illumination, the accelerating beam at arbitrary distances from the metasurface is obtained by reversing Eq. (4.13)

$$E(z,x) = \iint G_0(z, x-x')^{+} E(0,x')dx' \quad (4.15)$$

where

$$G_0(z, x-x')^{+} = H_0^1\left[k\sqrt{z^2 + (x-x')^2}\right] \quad (4.16)$$

is the appropriate forward propagating Green's function and H_0^1 is the 0th order Hankel function of the second kind.

We designed two metasurfaces that generate accelerating beams with radii of curvature of 400 μm and 100 μm, both with α = 0.01 μm^{-1}.The nanoantennas were fabricated with standard electron-beam lithography on ITO-coated glass, followed by electron-beam evaporation of 3 nm

Ti and 30 nm Au and lift-off processes. Optical microscope and SEM images of one of our metasurfaces are shown in Figure 4.6a. To facilitate the imaging of the accelerating beam, one of the edges of the ITO-coated glass slide was polished down to optical quality prior to fabrication using the process described in Section 2.4, and the leading edge of the metasurface was positioned within 1 mm from the edge of the slide.

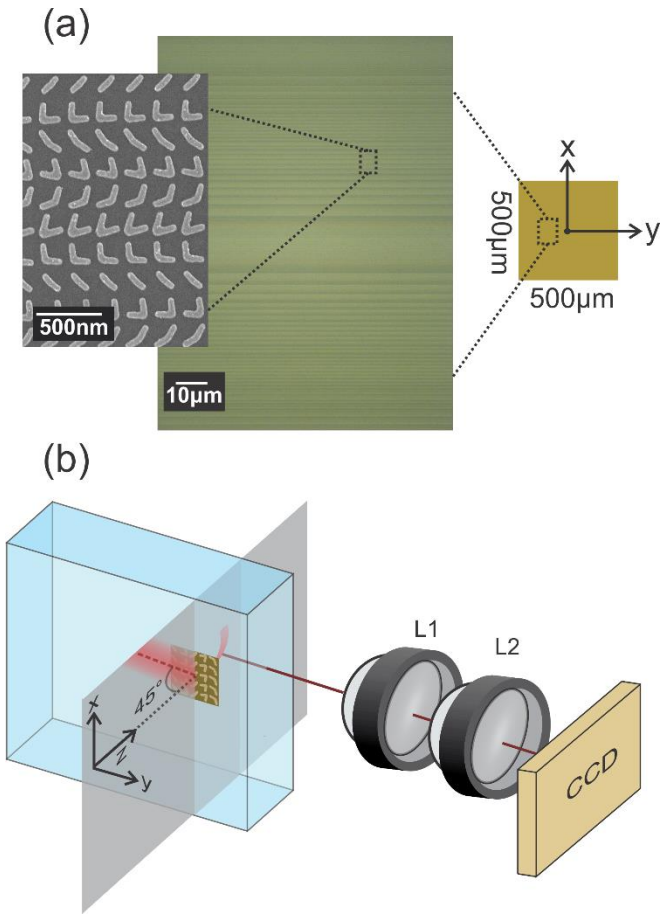

Figure 4.6. Schematics of the experimental setup and images of the metasurface. (a) Optical microscope image (green) showing the large-scale pattern of the antenna array which modulates the incident field along the x-axis. Individual antennas are resolved in the SEM image. (b) Schematics describing the metasurface illumination and set-up used for imaging the accelerating beams. The beam reflected by the metasurface has been omitted. The first lens (L1) collects light from the accelerating beam scattered from defects in the glass and the second lens (L2) images the collected light onto the CCD. The gray area indicates the image plane.

The metasurfaces were illuminated with a mode-locked Ti:Sapphire oscillator which produced pulses of central wavelength 800 nm and bandwidth of 30 nm at a 78 MHz repetition rate. As discussed earlier, the *y*-polarized output from the laser was incident onto the metasurface at an angle of 45 degrees after being loosely focused with a lens, which generated an accelerating beam polarized in the *x*-*z* plane; these axes are defined in Figure 4.6b. We used a standard setup to image the accelerating beam by collecting Rayleigh-scattered light from defects inside the glass. The polarization dependence of the Rayleigh cross-section helped reduce the signal of the *y*-polarized unperturbed transmission in the images. Figure 4.7 shows a comparison between the experimental images of the accelerated beams and their theoretical intensity. The features of the experimental trajectories resolved by the imaging system agree very well with those predicted by simulations.

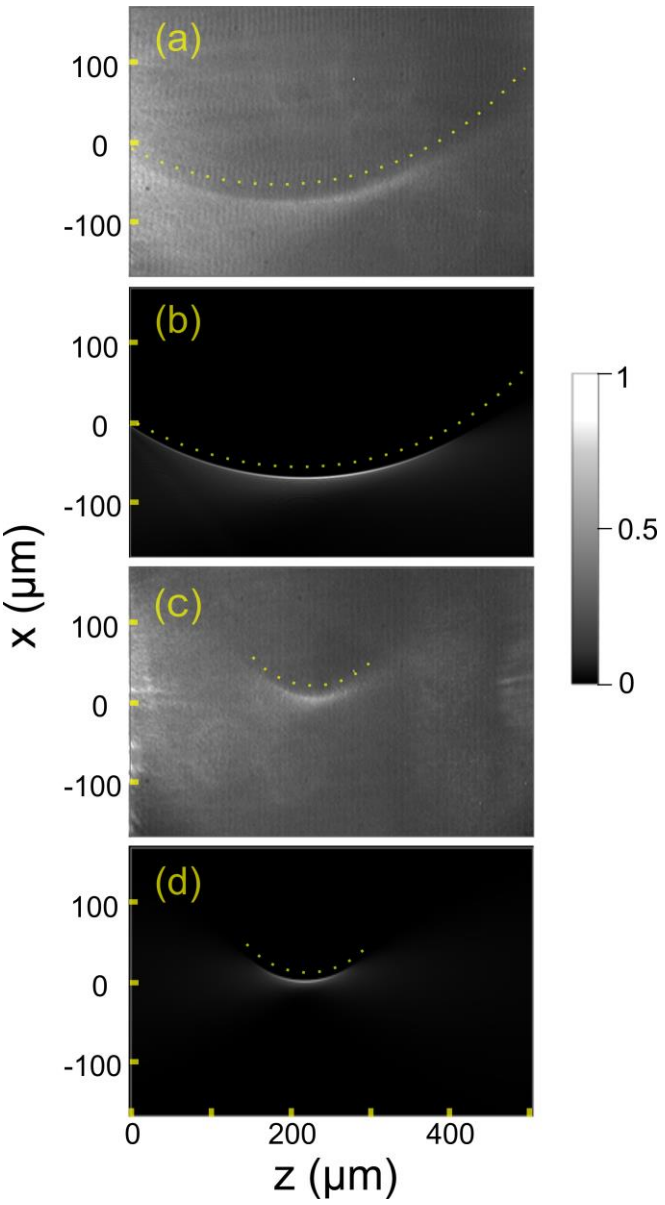

Figure 4.7. Experimental (a), (c) and calculated (b), (d) intensity plots for the 400 μm and 100 μm radius of curvature metasurfaces, respectively. To highlight the beam acceleration, a dotted line was added tracing circular trajectories of the same radius of curvature.

4.4. Accelerating Light Pulses

4.4.1. Introduction

So far, we have examined the nature of accelerating beams for the case of monochromatic light. Admittedly, in the previous section, we illuminate the metasurface with an ultrafast pulse. Of course, the CCD response time is too slow to capture the motion of the accelerating pulse; it measures the time-integrated intensity of the accelerating beam. From Parseval's theorem, we can also think of this image as the integral of the beam intensity over the pulse bandwidth. A quick calculation shows that there are only slight differences between the image of the beam intensity evaluated at the central frequency of the pulse and the image of several trajectories added together over a 30 nm bandwidth. If we had a camera that was fast enough to take snap shots of the accelerating pulse itself (which, we in fact do, as we will see in Chapter 5), then how would such a pulse look? Let's investigate with some calculations.

I should note that the qualitative features of the accelerating pulse propagation are the same for all radii of curvature and for all constant indexes of refraction *n*. Thus, to reduce calculation time, we will investigate the effects of pulse propagation for a beam accelerating in air with a radius of 50 μm.

4.4.2. Calculations of the Accelerating Pulse Produced by the Metasurface

Looking at eq. (4.12), the field designated at the center of the accelerating beam trajectory has a frequency-dependence from the wavenumber $k = \omega n/c$. The metasurface is designed to produce an accelerating field (eq. 4.13) for an illumination frequency $f_0 = \omega_0/2\pi = 3.75 \times 10^{14}$ Hz (design wavelength λ_0 = 800 nm). Rewriting eq. (4.13) gives us:

$$E_{\omega_0}(0,x) = \int G^{-}_{\omega_0}(z_0, x - x')E_{\omega_0}(z_0, x')dz' \qquad (4.17)$$

where $E_{\omega_0}(z_0, x')$ is the field of the "half-Bessel beam" at $\omega = \omega_0$ and $G^{-}_{\omega_0}(z_0, x - x')$ is the reverse propagating Green's function at $\omega = \omega_0$. When illuminating the metasurface with a pulse, we need to determine the accelerating field $E_{met_\omega}(z, x)$ that is produced at each frequency within the bandwidth of the illuminating pulse. This is found by convolving eq. (4.17) with the forward's propagating Green's Function for each illumination frequency ω:

$$E_{met_\omega}(z, x) = \iint G^{+}_{\omega}(z, x - x') E_{\omega_0}(0, x') dx' \qquad (4.18)$$

Figure. 4.8 shows $\left|E_{met_\omega}(z, x)\right|^2$ for three different frequencies near $f_0 = \omega_0/2\pi$. Over the course 40 nm, there are some slight, but clear differences in the trajectory of the intensity maximum. These effects play a role in the shaping of the pulse, as discussed below.

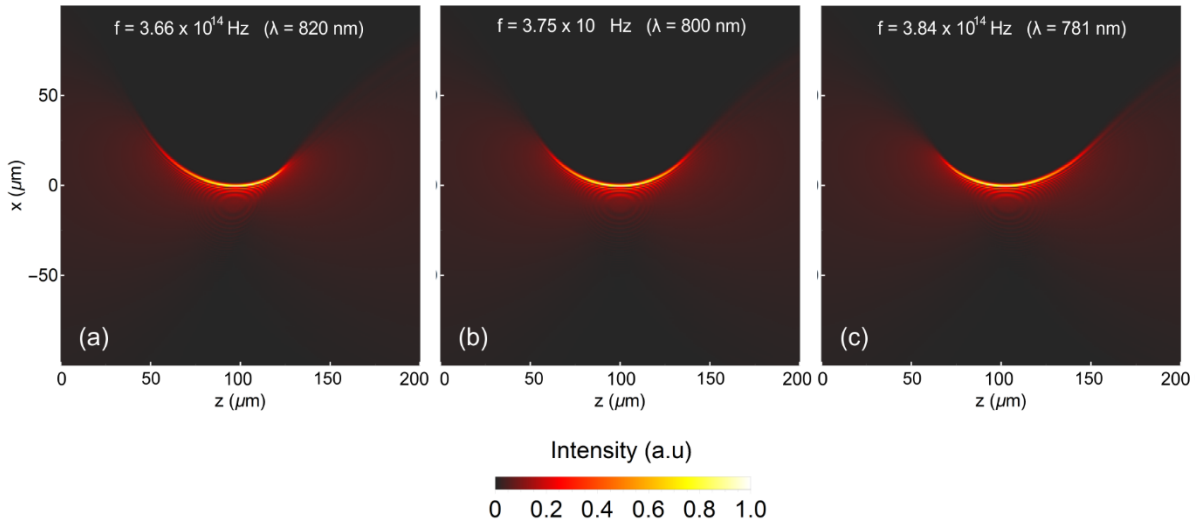

Figure 4.8. Plots of $\left|E_{met_\omega}(z, x)\right|^2$ with parameters z_0= 0, $\alpha = 0.0625$ μm^{-1}, β =393, n =1, and R = β/k =50 μm for three different frequencies.

We assume that the pulse illuminating the metasurface has a Gaussian frequency spectrum given by:

$$E_g(\omega) = \exp\left(\frac{-(\omega-\omega_0)^2}{4a}\right) \quad (4.19)$$

where $a = 2\ln(2)/\tau^2$, and τ is the FWHM of the intensity envelope of the Gaussian pulse. The field of the accelerating pulse in the time-domain, which we will call $E_p(z,x,t)$, is found by multiplying eq. (4.18) with eq. (4.19) and then taking the inverse Fourier transform:

$$E_p(z,x,t) = \int E_{met_\omega}(z,x) \times E_g(\omega) e^{-i\omega t} d\omega \quad (4.20)$$

Figure 4.9 shows plots of $\left|E_p(z,x,t)\right|^2$ for four different propagation times. The pulse has upper (x > 0) and lower (x < 0) branches which exchange positions after the pulse focuses and passes through the center of the arc. The pulse then continues to propagate with a shape that resembles a boomerang.

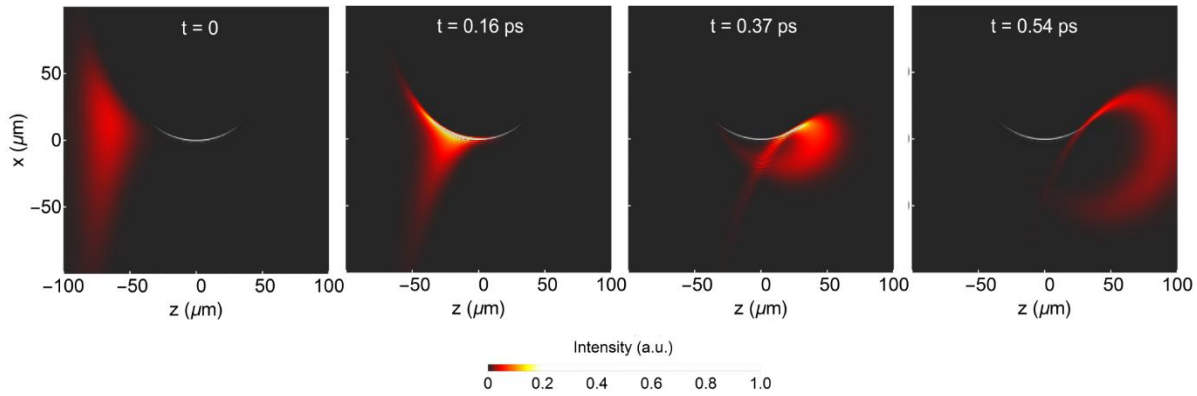

Figure 4.9. Plots of $\left|E_p(z,x,t)\right|^2$ shown with the trajectory of the intensity maximum. The parameters used in the calculation are $\alpha = 0.0625\ \mu m^{-1}$, β =393, n =1, R = β/k =50 μm, and $\tau = 100\ fs$. The qualitative features of the pulse propagation are the same regardless of radius of curvature and index of refraction (in the absence of dispersion). This pulse is thus representative of the type of pulse generated by the metasurface.

4.4.3. Calculations of an "Ideal" Accelerating Pulse

Now, let's take ourselves into a hypothetical space and pretend that we have a device located at z = 0 that can produce the actual finite energy solution $E_\omega(z_0, x)$ for every frequency ω within the bandwidth of the illuminating pulse. In other words, the field produced at z = 0 for each frequency ω is:

$$E_{ideal_\omega}(0, x) = \iint G_\omega^-(z_0, x - x')E_\omega(z_0, x')dx' \quad (4.21)$$

Thus, the field produced for $z > 0$ is:

$$E_{ideal_\omega}(z, x) = \iint G_\omega^+(z, x - x')\, E_\omega(0, x')dz' \quad (4.22)$$

Figure (4.10) shows contour plots of $\left|E_{ideal_\omega}(z, x)\right|^2$. Clearly, changes in the accelerating beam trajectory are negligible over the course of a 40 nm bandwidth.

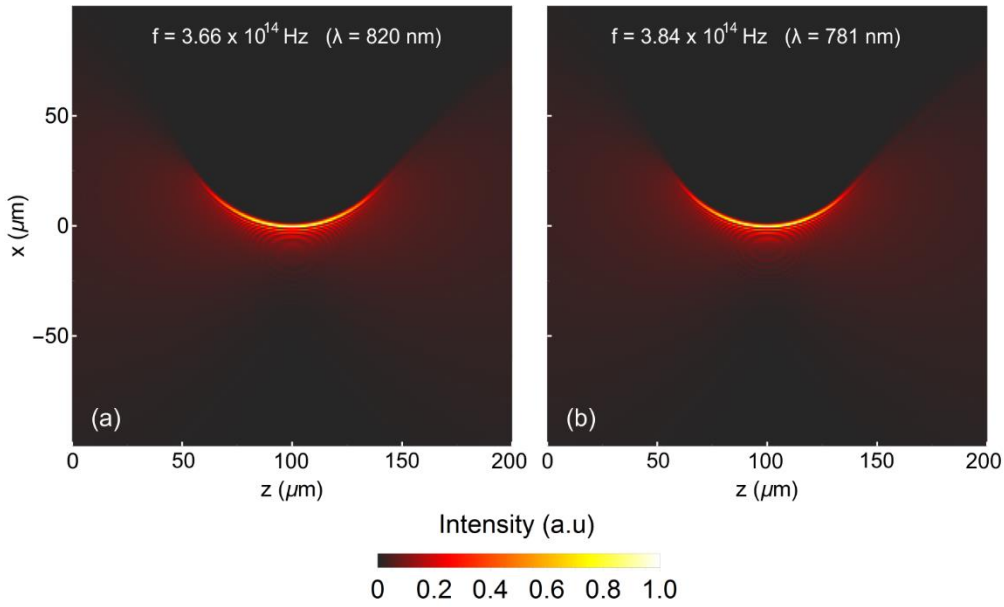

Figure 4.10. Contour plots of $\left|E_{ideal_\omega}(z, x)\right|^2$ with parameters $\alpha = 0.0625\ \mu m^{-1}$, β =393, n =1, and R = β/k =50 μm.

As in 4.3.1, we can find the field of the pulse in the time domain (let's call the field for this pulse $E_{p2}(z,x,t)$) by taking the inverse Fourier transform of the accelerating beam spectrum $E_{ideal_\omega}(z,x)$ multiplied by the Gaussian pulse spectrum $E_g(\omega)$:

$$E_{p2}(z,x,t) = \int E_{ideal_\omega}(z,x,\omega) \times E_g(\omega) e^{-i\omega t} d\omega \quad (4.23)$$

Figure 4.11 shows contour plots of $\left|E_{p2}(z,x,t)\right|^2$ at different propagation times overlapped with the trajectory of the intensity maximum at 800 nm. The resulting pulse looks as if we plotted the beam intensity for a single frequency and then propagated a Gaussian time window across the plot, which contrasts from the behavior of the pulse shown in Fig. (4.9). By looking at the plots for t = 0.16 ps and t = 0.32 ps, we can see that the pulse in Fig. (4.11) maintains a tight focus for a longer part of the beam trajectory compared to the pulse shown in Fig. (4.9). This can be beneficial for experiments in nonlinear optics such as those discussed in the next chapter. Generating these types of pulses is something to consider for future work.

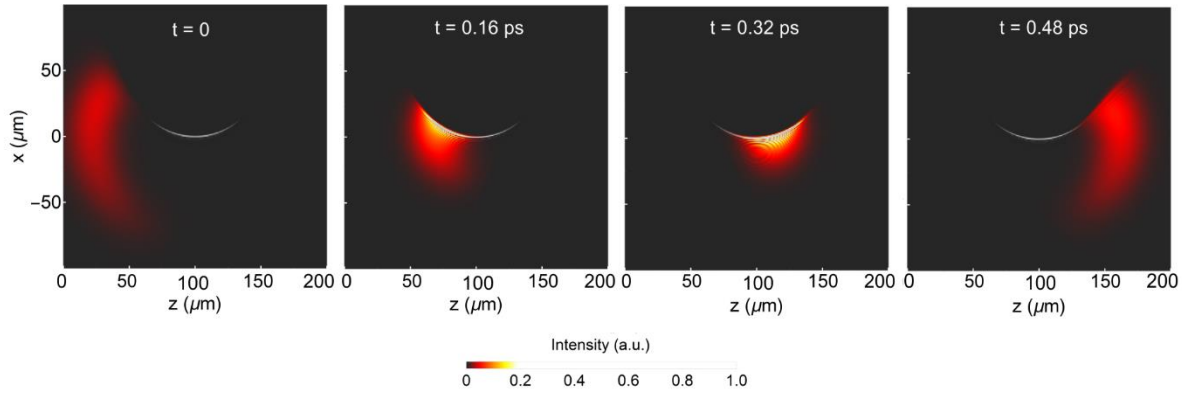

Figure 4.11. Plots of $\left|E_{p2}(z,x,t)\right|^2$ with parameters $\alpha = 0.0625$ μm^{-1}, β =393, n =1, nm, R = β/k =50 μm, and $\tau = 100\ fs$.

4.5. Summary

We accelerated light inside a material using a single planar optic. Our metasurfaces have an unrestricted ability to bend light, and simple tunings of their design can produce beams with radii of curvature ranging from several to thousands of wavelengths. This highly versatile method opens new opportunities for the integration of accelerating beams into on-chip photonic systems and for advanced studies of accelerating light in materials. One such opportunity will be discussed in the next chapter in which we use an accelerating pulse to generate synchrotron radiation in a nonlinear crystal.

We also investigated the propagation of two types of accelerating pulses. The first, and most relevant case, is the type of pulse produced by the metasurface. Calculations show that the propagation of this pulse has distinct features that are the result of minor changes in the beam trajectory over the course of the pulse bandwidth. The second pulse that was considered is the pulse that would be produced if we had a device at $z = 0$ that could produce the actual half-Bessel solution at each frequency within the bandwidth of the illuminating pulse. In this case, the change in beam trajectory over the course of the pulse bandwidth is negligble, which results in a pulse with a shape that is distinct from the actual pulse produced by the metasurface.

CHAPTER 5
SYNCHROTRON RADIATION FROM AN ACCELERATING LIGHT PULSE

"Like a space ship with an uncanny velocity, we'll break the barrier of light if put to the test"

The Republic Tigers, *"Feelin' the Future"*

It has been a remarkable privilege to work with Di, Carl, and their mentors. The success of the projects in Chapters 4 and 5 would not have been possible without the talent and dedication of everyone involved. As in Chapter 4, Carl performed the metasurface design, and Di performed the fabrication. This chapter contains a considerable amount of text from a manuscript that is currently under review for publication [96].

5.1. Introduction

Synchrotron radiation, the emission from a relativistic charge moving along a circular trajectory, was first observed in 1947 [97]. Until the 1960s, synchrotrons were used to accelerate electrons exclusively for experiments in particle physics, and the radiation losses were studied primarily because they were an impediment to achieving high electron energies [98,99,100]. Presently, there exist large-scale synchrotrons that produce high intensity X-rays used to perform experiments for a myriad of studies, including those in marine biology, [101] environmental

science, [102] condensed matter physics, [103,104] and neuroscience [105]. Synchrotron radiation has also been observed at radio frequencies from accelerating polarization currents created by capacitor arrays [106] and is produced by astrophysical phenomena such as radio galaxies and supernovae [107].

Here, we present the first observation of synchrotron radiation resulting from the acceleration of a light pulse. A metasurface was used to guide a pulse of 800 nm central wavelength and 100 fs duration along a hundred micron-scale circular arc inside a $LiTaO_3$ crystal. As it mixes with itself through the second-order susceptibility of the crystal, the accelerating light pulse generates both second harmonic and difference-frequency nonlinear polarizations. As in the case of a charge distribution traversing a circular trajectory in vacuum, the moving nonlinear polarizations emit synchrotron radiation. We measure the emission from the difference-frequency polarization, which is in the THz range. This demonstration of synchrotron radiation over a scale of 100 μm is the smallest to date.

To truly appreciate the synchrotron radiation emitted by a dipole distribution accelerating in $LiTaO_3$, we should first gain some understanding of the radiation emitted by a single charge moving at a constant speed along a circular trajectory. There are a couple of ways to do this. One way is to use a finite-difference time-domain (FDTD) program to solve Maxwell's equations for a very small charge distribution moving along a circular trajectory. This is the quickest way, and I will present some results from such simulations in this chapter. Another way to accomplish this is to solve the Lienerd-Wiechert potentials for a moving charge and generate image sequences that show the time-evolution of the electric field. Although a bit more laborious, I found the latter method to be fairly insightful.

5.2. Liénard-Wiechert Potentials for the Field Radiated by a Moving Charge

The Liénard-Wiechert potentials are electric scalar and magnetic vector potentials for a single moving charge and are valid for all charge velocities and trajectories. They were derived independently by Liénerd (1898) and Wiechert (1900), and they can be found in almost all textbooks on electromagnetism.

Let's start with Maxwell's Equations. Here, we assume that a moving charge distribution is present either in air ($\mu_r = 1, \epsilon_r = 1$) or in a dielectric ($\mu_r = 1, \epsilon_r > 1$).

$$\nabla \cdot \boldsymbol{E} = \frac{\rho}{\epsilon_0 \epsilon_r} \quad (5.1)$$

$$\nabla \cdot \boldsymbol{B} = 0 \quad (5.2)$$

$$\nabla \times \boldsymbol{E} = -\frac{\partial \boldsymbol{B}}{\partial t} \quad (5.3)$$

$$\nabla \times \boldsymbol{B} = \mu_0 \boldsymbol{J} + \mu_0 \epsilon_0 \frac{\partial}{\partial t} \epsilon_r \boldsymbol{E} \quad (5.4)$$

where ρ and $\boldsymbol{J}$ are respectively the free charge and current densities. The fields $\boldsymbol{E}$ and $\mathbf{B}$ are related to the electric scalar potential φ and magnetic vector potential $\mathbf{A}$ by

$$\boldsymbol{E} = -\nabla\varphi - \frac{\partial A}{\partial t} \quad (5.5)$$

$$\mathbf{B} = \nabla \times \mathbf{A} \quad (5.6)$$

If we insert (5.6) into (5.4) and (5.5) into (5.1), then we obtain the wave equations for respectively, $\boldsymbol{A}$ and φ:

$$-\nabla^2 \boldsymbol{A} + \frac{\epsilon}{c^2} \frac{\partial^2 \boldsymbol{A}}{\partial t^2} + \nabla \left(\nabla \cdot \boldsymbol{A} + \frac{\epsilon}{c^2} \frac{\partial \varphi}{\partial t} \right) = \mu_0 \boldsymbol{J} \quad (5.7)$$

$$-\nabla^2 \varphi - \frac{\partial}{\partial t} \nabla \cdot \boldsymbol{A} = \frac{\rho}{\epsilon_0 \epsilon_r} \quad (5.8)$$

Using the Lorenz gauge:

$$\nabla \cdot \boldsymbol{A} + \frac{\epsilon}{c^2}\frac{\partial \varphi}{\partial t} = 0 \quad (5.9)$$

(5.7) and (5.8) become:

$$\nabla^2 \boldsymbol{A} + -\frac{\epsilon}{c^2}\frac{\partial^2 \boldsymbol{A}}{\partial t^2} = -\mu_0 \boldsymbol{J} \quad (5.10)$$

$$\nabla^2 \varphi - \frac{\epsilon}{c^2}\frac{\partial^2 \varphi}{\partial t^2} = -\frac{\rho}{\epsilon_0 \epsilon_r} \quad (5.11)$$

The solutions to these inhomogeneous wave equations are found by convolving the source term on the right-hand side of the wave equation with the Green's Function for *m*-dimensional (*m* = 1, 2, or 3) space. Let's assume we are working in 3D space:

$$\boldsymbol{A}(\boldsymbol{r}, t) = -\frac{\mu_0}{4\pi}\iint G(\boldsymbol{r} - \boldsymbol{r}', t - t')\,\boldsymbol{J}(\boldsymbol{r}', t')dr'dt' \quad (5.12)$$

$$\varphi(\boldsymbol{r}, t) = -\frac{1}{4\pi\epsilon_0\epsilon_r}\iint G(\boldsymbol{r} - \boldsymbol{r}', t - t')\,\rho(\boldsymbol{r}', t')dr'dt' \quad (5.13)$$

where

$$G(\boldsymbol{r} - \boldsymbol{r}', t - t') = \frac{\delta\left(t - t' - |\boldsymbol{r} - \boldsymbol{r}'|\frac{n}{c}\right)}{|\boldsymbol{r} - \boldsymbol{r}'|} \quad (5.14)$$

is the Green's function for an outgoing wave in 3D space and $n = \sqrt{\epsilon_r}$ is the refractive index. The coordinate $\boldsymbol{r}'$ defines the position of the charge at a time t'. The radiation emitted by a charge at position $\boldsymbol{r}'$ and time t' is observed at a given position $\boldsymbol{r}$ at a later time $t = t' + |\boldsymbol{r} - \boldsymbol{r}'|\frac{n}{c}$. Thus, t' is known as the *retarded time* and *t* is the *observation time*. Causality requires that $t > t'$

We will continue by following an approach presented in [108]. For a single charge q moving along a trajectory $\boldsymbol{r_0}(t')$ with velocity $\boldsymbol{v}(t')$ the charge and current densities are:

$$\rho(\boldsymbol{r}', t') = q\delta(\boldsymbol{r}' - \boldsymbol{r_0}(t')) \quad (5.15)$$

$$j(\boldsymbol{r}', t') = q\boldsymbol{v}(t')\delta(\boldsymbol{r}' - \boldsymbol{r_0}(t')) \quad (5.16)$$

Substituting these expressions into (5.12) and (5.13) gives us:

$$\boldsymbol{A}(\boldsymbol{r},t) = -\frac{q\mu_0}{4\pi}\iint \frac{\delta\left(t-t'-|\boldsymbol{r}-\boldsymbol{r}'|\frac{n}{c}\right)}{|\boldsymbol{r}-\boldsymbol{r}'|}\,\boldsymbol{v}(t')\delta(\boldsymbol{r}'-\boldsymbol{r_0}(t'))dr'dt' \quad (5.17)$$

$$\varphi(\boldsymbol{r},t) = -\frac{q}{4\pi\epsilon_0\epsilon_r}\iint \frac{\delta\left(t-t'-|\boldsymbol{r}-\boldsymbol{r}'|\frac{n}{c}\right)}{|\boldsymbol{r}-\boldsymbol{r}'|}\,\delta(\boldsymbol{r}'-\boldsymbol{r_0}(t'))dr'dt' \quad (5.18)$$

integrating over r':

$$\boldsymbol{A}(\boldsymbol{r},t) = -\frac{q\mu_0}{4\pi}\int \boldsymbol{v}(t')\frac{\delta\left(t-t'-|\boldsymbol{r}-\boldsymbol{r_0}(t')|\frac{n}{c}\right)}{|\boldsymbol{r}-\boldsymbol{r_0}(t')|}dt' \quad (5.19)$$

$$\varphi(\boldsymbol{r},t) = -\frac{q}{4\pi\epsilon_0\epsilon_r}\int \frac{\delta\left(t-t'-|\boldsymbol{r}-\boldsymbol{r_0}(t')|\frac{n}{c}\right)}{|\boldsymbol{r}-\boldsymbol{r_0}(t')|}dt' \quad (5.20)$$

To carry out the integration over t', we use the formula:

$$\delta(f(x)) = \sum_i \frac{\delta(x-x_i)}{\left|\left(\frac{df}{dx}\right)_{x=x_i}\right|} \quad (5.21)$$

where x_i is the i^{th} root of the equation $f(x)=0$. Thus, the delta functions in (5.19) and (5.20) become:

$$\delta\left(t-t'-|\boldsymbol{r}-\boldsymbol{r_0}(t')|\frac{n}{c}\right) = \sum_i \frac{\delta(t-t_i')}{\left|1-\frac{n}{c}\left[\frac{\boldsymbol{v}(t_i')\cdot(\boldsymbol{r}-\boldsymbol{r}_0(t_i'))}{|\boldsymbol{r}-\boldsymbol{r}_0(t_i')|}\right]\right|} \quad (5.22)$$

where t_i' is the i^{th} root of the equation

$$t' = t-|\boldsymbol{r}-\boldsymbol{r_0}(t')|\frac{n}{c} \quad (5.23)$$

.

The Liénard-Wiechert potentials are then given by:

$$\boldsymbol{A}(\boldsymbol{r},t) = -\frac{q\mu_0}{4\pi}\sum_i \frac{\boldsymbol{v}(t_i')}{\left|\boldsymbol{r}-\boldsymbol{r}_0(t_i')\right| \times \left|1-\frac{n}{c}\left[\frac{\boldsymbol{v}(t_i')\cdot(\boldsymbol{r}-\boldsymbol{r}_0(t_i'))}{\left|\boldsymbol{r}-\boldsymbol{r}_0(t_i')\right|}\right]\right|} \quad (5.24)$$

$$\varphi(\boldsymbol{r},t) = -\frac{q}{4\pi\epsilon_0\epsilon_r}\sum_i \frac{1}{\left|\boldsymbol{r}-\boldsymbol{r}_0(t_i')\right| \times \left|1-\frac{n}{c}\left[\frac{\boldsymbol{v}(t_i')\cdot(\boldsymbol{r}-\boldsymbol{r}_0(t_i'))}{\left|\boldsymbol{r}-\boldsymbol{r}_0(t_i')\right|}\right]\right|} \quad (5.25)$$

Equations (5.24) and (5.25) are valid for both $v < c/n$ and $v > c/n$. For $v < c/n$, for any trajectory $\boldsymbol{r}_0(t')$, there is only one solution to (5.23). Thus, the field observed at a given position at a time t consists of the emission from the charge at a *single* retarded time t'. This is not the case for $v > c/n$. When $v > c/n$, (5.23) can have several solutions which also satisfy $t' < t$. This means that emissions from the charge at several retarded times contribute to the field observed at a given position and time t. I will illustrate this by plotting solutions to (5.23) for a charge undergoing circular motion. Here, we will assume that the charge rotates in the counter-clockwise direction. The corresponding trajectory is:

$$\boldsymbol{r_0}(t') = R(-\cos(\omega t')\,\hat{\boldsymbol{x}} - \sin(\omega t')\,\hat{\boldsymbol{y}}) \quad (5.26)$$

where $\omega = v/R$. Assuming that the observation point lies in the plane of the circular trajectory (z = 0), then inserting (5.26) into (5.23) gives us:

$$t' = t - \frac{c}{n}[x^2 + y^2 - 2R(-x\cos(\omega t') - y\sin(\omega t') + R^2)]^{1/2} \quad (5.27)$$

This equation is transcendental; thus we need to plot both sides together in order to find the solutions. Figure 5.1 shows plots of (5.27) for three different charge speeds. The points at which the curves intersect give the retarded times t_i' that contribute to the radiation observed at time *t* for a given observation point. As shown in (a), there is a contribution from only one retarded time

when $v < c/n$. As shown in (b) and (c), multiple retarded times can contribute to the radiation observed at t when $v > c/n$.

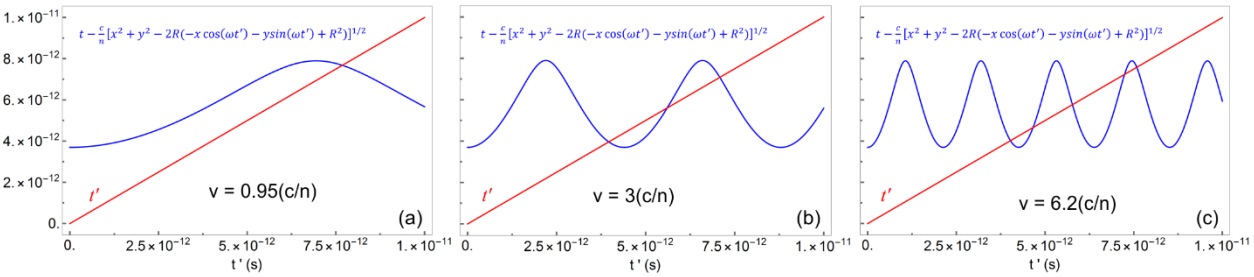

Figure 5.1. Plots of the right-hand side (blue) and left hand-side (red) of (5.27) for a charge moving along a trajectory defined by (5.26) with R = 25 μm and in a medium with n = 6.3. The observation point is located at (x, y) = (0, 100 μm), and the observation time is $t = 1 \times 10^{-11}$ s.

5.3. Images of the Synchrotron Field Resulting From a Single Charge: $v < c / n$

To generate images of the fields for a charge moving along a circular trajectory, it is first necessary to find the values of t' which satisfy (5.27) for each observation (x,y) point at a given time t. This was done numerically; the code is attached in the appendixes. Then, each value of t' is inserted into (5.24) and (5.25), and fields are found according to (5.5). Results are shown in Figure 5.2 for a single charge propagating in vacuum for different values of $v < c$.

In Figure 5.2(a) where v = 0.25c, the electron is propagating in the non-relativistic regime, which occurs when the quantity $\gamma = (1 - n^2\, v^2/c^2)^{-1/2} \approx 1$. At a given instant, the charge emits radiation into a large range of solid angles.

For $\gamma > 1$, the relativistic Doppler effect plays a role in the shaping of the radiation pattern as $v/c \to 1$. We begin to see relativistic effects in Figure 5.2(b) for $v = 0.5c$ ($\gamma = 1.15$), and of course, they are very prominent in Figure 5.2(c) for $v = 0.95c$ ($\gamma = 3.2$). At a given instant, the

radiation from the charge is emitted strongly in the direction parallel to the electron's instantaneous velocity and is concentrated within a narrow solid angle.

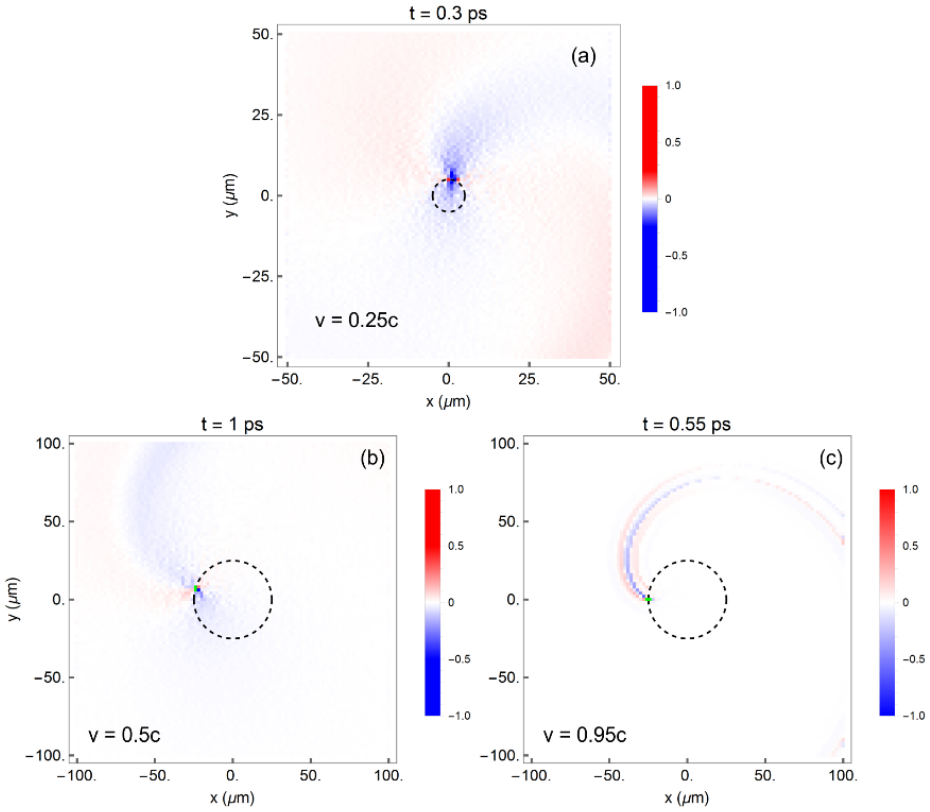

Figure 5.2. Plots of the x-component of the synchrotron electric field as obtained by solving the Liénard-Wiechert potentials for an electron travelling along a circular trajectory in vacuum (n =1). The electron position is indicated by a green dot. (a) R = 5 μm, v = 0.25c. (b) R = 50 μm v = 0.5c. (c) R = 50 μm v = 0.95c

5.4. Images of the Synchrotron Field Resulting From a Single Charge: $v > c / n$

Before getting into the physics, I should first note that in this section, I present contour plots which show results from two different methods for finding the synchrotron field for a charge moving with v > c/n. The first is the code that I wrote to solve the Liénard-Wiechert potentials which was used in the last section. The second method used a finite-difference time-domain program (COMSOL 4.3b) to calculate the fields resulting from a tiny circulating charge distribution. The two methods produce qualitatively similar results. However, I found that the code

I wrote required very high resolution when solving the potentials for $v > c/n$, and it therefore took quite a long time to run. This is likely related to the fact that the radiation spectrum for $v > c/n$ is not truncated for the case of a single charge (we will see this in section 5.5). The FTDT simulations are much faster at generating images of the radiation field for several observation times when compared to the code I wrote.

When a charge is moving along a circular trajectory in a medium of $n > 1$ and $v > c/n$, the Cerenkov effect changes the radiation pattern considerably. First observed by P. A. Cerenkov and later derived by Tamm and Frank, Cerenkov radiation results when a charge's velocity v exceeds the phase velocity of light c/n in a medium of index n. For a charge travelling along a linear trajectory, the radiation is emitted into a cone subtended by an angle given by $\alpha = \pi/2 - \theta_c$, where θ_c is the angle between the propagation direction of the radiation and the velocity of the charge which is determined by $\cos(\theta_c) = (c/nv)$. An example is shown Figure 5.3.

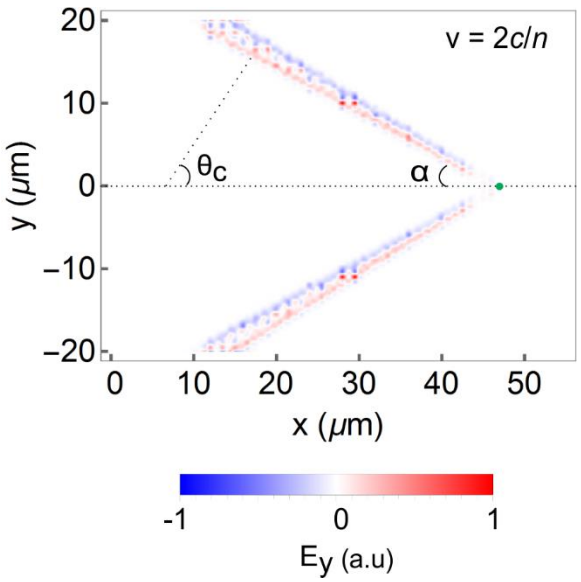

Figure 5.3. Cerenkov radiation from a charge moving along a trajectory parallel to the x-axis at a speed of $v = 2c/n$. The position of the charge is shown with a green dot. For $v = 2c/n$, $\theta_c = 60°$. The plot was generated by solving the Liénard-Wiechert potentials for a moving charge and finding the corresponding fields.

The Cerenkov effect causes the radiation pattern from a charge moving along a circular trajectory of radius R to have both inner ($x^2 + y^2 < R^2$) and outer ($x^2 + y^2 > R^2$) branches, which is illustrated in Figure 5.4 for different velocities of $v > c/n$. Note that only the latter exists for the case of $v < c/n$ discussed in the previous section.

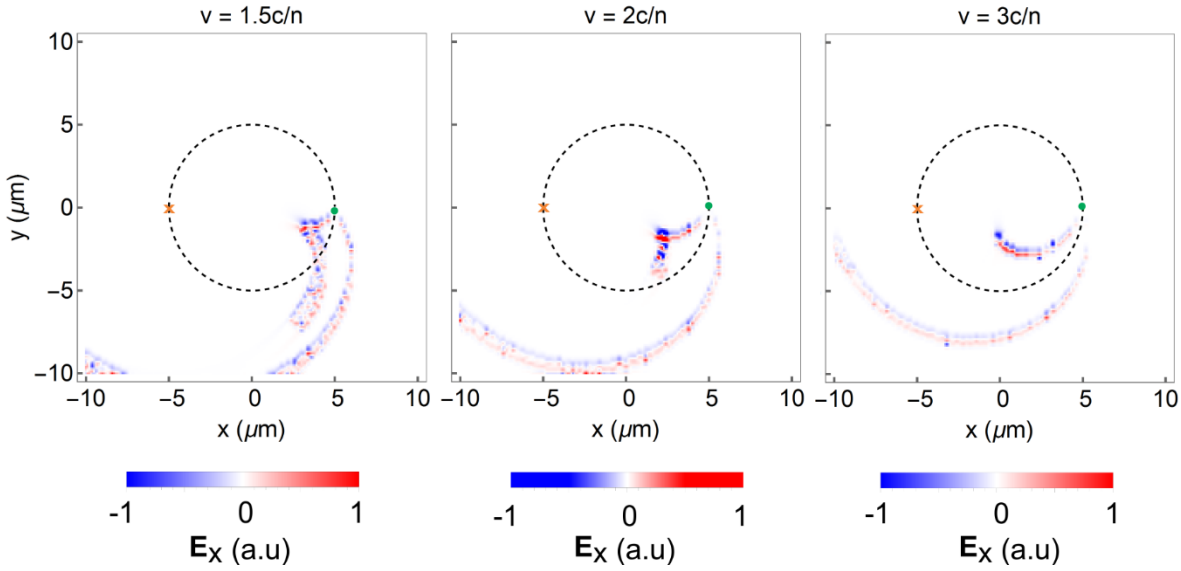

Figure 5.4. Contour plots of the x-component of the emitted field found by solving the Liénard-Wiechert potentials for a charge moving counter-clockwise along a circular trajectory of R = 5 μm in a medium of n = 3.2. The starting position of the charge is (x, y) = (- 5 μm, 0), as marked by the orange "x". All three images show the synchrotron field at the instant when the charge, denoted by the green dot, completes one half of a revolution.

Figure 5.5 shows results of FDTD simulations of a tiny charge distribution which makes 1.5 revolutions around a circular path at a speed of v = 3c/n and an angular speed of ω_0. Once the particle makes one-half of a revolution, we see the formation of a cusp, or bunching together of the electric field, in the inner radiation branch. This feature has been noted in a number of works and is characteristic of superluminal synchrotron radiation [108,109]. The cusp revolves at the

same angular velocity as the electron ($\omega_0 = v/R$), but with a speed of c/n; thus, it travels along a smaller circular trajectory given by $R' = c/n\omega_0$. Once the electron fails to maintain its trajectory, the cusp loses its formation and diffracts.

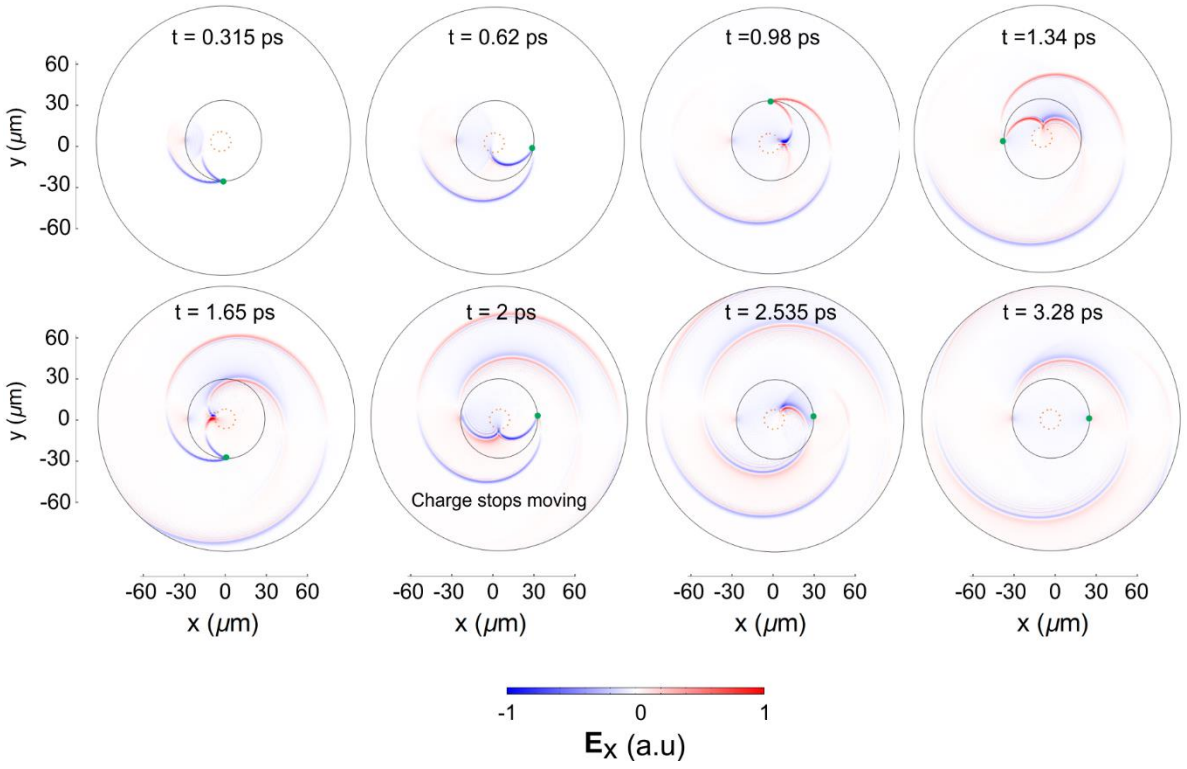

Figure 5.5. Simulations of a charge moving counterclockwise along a circular trajectory of R = 30 μm in a medium with n = 6.3. The charge begins moving at t = 0, and its starting position is (x,y) = (-30 μm, 0). The cusp begins to form at t = 0.62 ps and rotates along the orange dotted trajectory of radius $R' = c/n\omega_0$ = 10 μm. The charge stops moving at $t \approx 2$ ps, causing the cusp to lose its shape and diffract for $t > 2$ ps.

5.5. The Synchrotron Radiation Spectrum for a Single Charge

In $LiTaO_3$, the nonlinear polarization generated by an 800 nm pulse propagates at approximately three times the phase velocity of light for frequencies below the lowest-lying transverse optical (TO) phonons of A_1- and E-symmetry [110]. As a result, the spectrum of the synchrotron radiation at these frequencies will exhibit the superluminal-type character discussed

in the preceding section. Consider a single electron of charge q that makes an infinite number of revolutions about a circular path of radius R. The expression for the power emitted into the mth harmonic of the revolution frequency $\omega_0 = v/R$, is given by [111]:

$$P_m = \frac{q^2 v}{c^2} m w_0{}^2 \left(2J'_{2m}\left(\frac{2mvn}{c}\right) + \left(1 - \frac{c^2}{n^2 v^2}\right) \int_0^{\frac{2mvn}{c}} J_{2m}(x)dx \right) \quad (5.28)$$

where J_{2m} and J'_{2m} are, respectively, the Bessel Function and its derivative, both of order $2m$, c is the speed of light in vacuum, and n is the index of refraction. This expression is valid for both $v < c/n$ and $v > c/n$. For light polarized parallel to the optic axis of $LiTaO_3$, $n = 6.3$ at frequencies considerably below that of the lowest-lying A_1-type TO phonon, at 6 THz [110]. Figure 5.6 shows the calculated discrete power spectra for emission from a charge at both subluminal and superluminal speeds in a medium with $n = 6.3$. When $v > c/n$, the radiated power increases with frequency whereas for $v < c/n$, the emission spectrum exhibits a cutoff at a critical frequency frequency $\omega_c = \frac{3}{2}\omega_0(1 - v^2 n^2/c^2)^{-3/2}$ [112] beyond which the radiation power is negligible. For speeds considerably greater than c/n, the radiated power increases substantially. As shown in Figure 5.6, the power radiated at a given frequency for $v = 3c/n$ is several orders of magnitude larger than that at a nearby frequency for $v = 0.95c/n$.

The calculated spectra for an electron revolving in a medium with $n = 6.3$ and $v = 3c/n$ for three paths of different radii are shown in the inset of Figure 5.6. The values for the electron velocity and light speed are similar to those in our experiments on $LiTaO_3$. The fact that the radiation involves a few discrete frequencies suggests that light-produced synchrotron THz radiation could be useful as a means to obtain on-chip continuous wave THz sources. Furthermore, synchrotron emission from a nonlinear accelerating polarization can serve as a new method for

generating coherent light at any frequency and in any medium at which conventional phase-matching with the nonlinear polarization is poor, such as at frequencies immediately above the Reststrahlen band in crystals such as ZnTe or GaP, or at second harmonic frequencies.

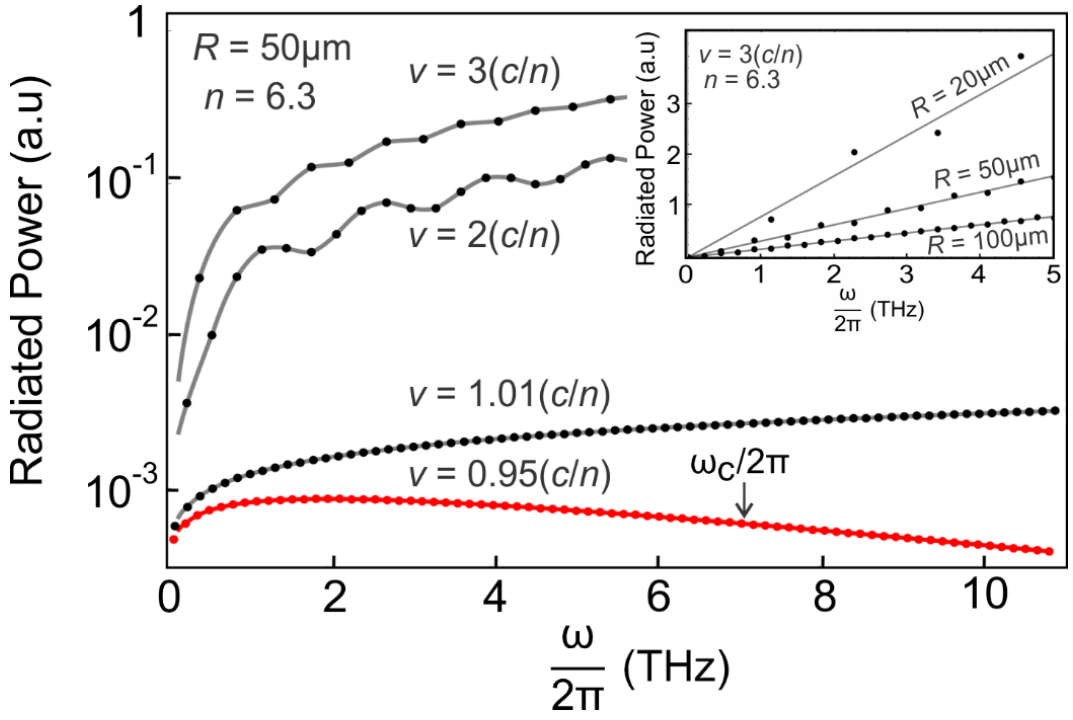

Figure 5.6. Calculated power radiated by a charge moving in a circle of radius R = 50 μm, at speeds below and above c/n , in a medium with n = 6.3 (note the logarithmic scale). Emission is at integer multiples of the fundamental frequency $\omega_0 = v/r$. At subluminal speeds, the emitted power drops rapidly for frequencies greater than the critical angular frequency ω_C . Inset: Results for $v = 3c/n$ and three different radii (linear scale). For speeds $v >> c/n$, the power emitted into harmonics behaves linearly with slope given by $(q^2 v/c^2)(1 - c^2/v^2 n^2)\omega_0$. The curves and lines are guides for the eye.

5.6. Synchrotron Radiation From a Nonlinear Polarization Accelerating in $LiTaO_3$

To calculate THz synchrotron field generated in our experiments, we must solve Maxwell's equations for the nonlinear polarization that is produced by the accelerating 800 nm pulse. The

field $\boldsymbol{E}_p(x,z,t)$ of the 800 nm pulse generated by the metasurface was calculating using the procedure presented in sections 4.3 and 4.4. For $LiTaO_3$, the refractive index n = 2.156 was taken to be constant over the bandwidth of the 800 nm pulse. For the 100 fs pulse used in the experiments, dispersive effects can be neglected. Note the interchange of the x and z coordinates between the notations used in Chapter 4 and Chapter 5.

The synchrotron electric field due to an accelerating difference frequency nonlinear polarization is found by solving the following nonlinear wave equation:

$$\left(\frac{\partial^2}{\partial x^2}+\frac{\partial^2}{\partial z^2}\right)E_s(x,z,t)-\frac{\epsilon}{c^2}\frac{\partial^2}{\partial t^2}E_s(x,z,t)=\frac{1}{c^2}\frac{\partial^2}{\partial t^2}P_{NL}(x,z,t)\approx\frac{1}{c^2}\frac{\partial^2}{\partial t^2}\chi_2\left|\boldsymbol{E}_p\right|^2 \quad (5.29)$$

where $E_s(x,z,t)$ is the electric field of the synchrotron radiation, $P_{NL}(x,z,t)$ is the nonlinear polarization, χ_2 is the second order nonlinear susceptibility, ϵ is the permittivity, and c is the speed of light in vacuum. Assuming an $e^{-i\Omega t}$ time dependence, the nonlinear wave equation valid for each frequency Ω is:

$$\left(\frac{\partial^2}{\partial x^2}+\frac{\partial^2}{\partial z^2}\right)E_s(x,z,\Omega)+\frac{\epsilon(\Omega)\Omega^2}{c^2}E_s(x,z,\Omega)=-\frac{\chi_2\Omega^2}{c^2}P_{NL}(x,z,\Omega) \quad (5.30)$$

where:

$$P_{NL}(x,z,\Omega)=\int P_{NL}(x,z,t)e^{i\Omega t}dt=\chi_2\int\left|\boldsymbol{E}_p(x,z,t)\right|^2e^{i\Omega t}dt \quad (5.31)$$

Using measured parameters from [110], the permittivity for light polarized parallel to the optic axis of $LiTaO_3$ is:

$$\epsilon_f=\varepsilon_\infty+\sum_j\frac{C_j\Omega_j^2}{\left(\Omega_j^2-\Omega^2-i\gamma_j\Omega\right)} \quad (5.32)$$

where Ω_j is the frequency of the jth A_1-type TO phonon in $LiTaO_3$; C_j and γ_j are respectively the corresponding oscillator strength and damping coefficient, and ε_∞ is the high frequency

permittivity. We solve eq. (5.31) for each frequency Ω within the bandwidth of the nonlinear polarization using a Green's Function technique. The solution is:

$$E_s(x,z,\Omega) = -\frac{\chi_2 \Omega^2}{c^2} \iint G_\Omega(x-x',z-z')^+ P_{NL}(x',z',\Omega) dz' dx' \quad (5.33)$$

where

$$G_\Omega(x-x',z-z')^+ = H_0^1\left[\frac{\Omega\sqrt{\epsilon(\Omega)}}{c}\sqrt{(x-x')^2+(z-z')^2}\right] \quad (5.34)$$

The synchrotron field as a function of time is finally found by taking the Inverse Fourier Transform of eq. 5.33:

$$E_s(x,z,t) = \int E_s(x,z,\Omega) e^{-i\Omega t} d\Omega \quad (5.35)$$

All convolution integrals were evaluated using the convolution theorem:

$$\int f(t') H(t-t') dt' = \int \hat{f}(\omega) \hat{H}(\omega) e^{-i\omega t} d\omega \quad (5.36)$$

where

$$\hat{f}(\omega) = \int f(t) e^{i\omega t} dt \quad (5.37)$$

$$\hat{H}(\omega) = \int H(t) e^{i\omega t} dt \quad (5.38)$$

All Fourier transforms and Inverse Fourier transforms were evaluated numerically using Fast Fourier Transform (FFT) and Inverse Fast Fourier Transform (IFFT) algorithms in Mathematica. The code is attached in the appendices.

5.7 Metasurface Design and Fabrication

We designed a plasmonic nanoantenna metasurface to accelerate light of wavelength 800 nm along a circular arc with a radius of curvature of 100 μm inside the $LiTaO_3$ crystal. The design

process follows the same procedure as the one presented in Section 4.3. In order to reduce the spatial overlap between the unperturbed and accelerating beams, the nanoantennas were arranged to produce an accelerating beam with a designated half-Bessel field at its trajectory center when illuminated at an angle of incidence of 45°. A contour plot showing the incident and scattered intensities for illumination with a single wavelength of 800 nm is shown in Fig. 5.7 (a).

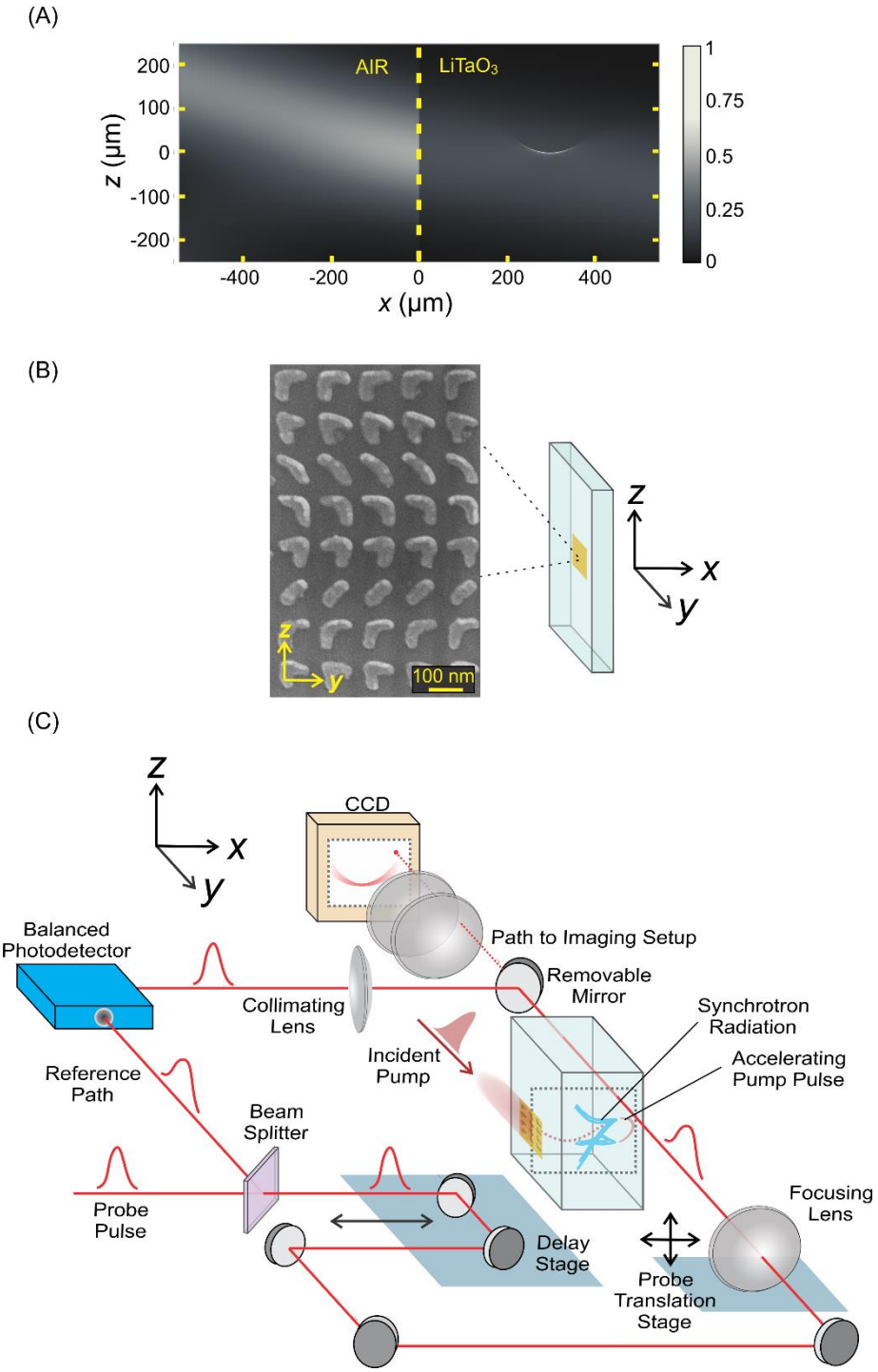

Figure 5.7. (a) Contour plot showing the intensity of the incident and scattered field from the metasurface, located at $x = 0$. The reflected beam intensity is roughly 5 times smaller than that of the incident beam. (b) Scanning electron microscope image of a section of the nanoantenna array fabricated onto the $LiTaO_3$ substrate. To facilitate the imaging of the accelerating beam, the leading edge of the metasurface was positioned ≈1 mm away from the edge of the substrate. The array was aligned to obtain an accelerating beam in the *x*-*z* plane, in accordance with the contour plot shown

in (a). The pattern repeats periodically along the *y*-axis; the width of the accelerating beam parallel to this axis is determined by the width of the incident beam. (c) Schematic of the orthogonal pump-probe setup. The output of a measurement set is an image sequence showing the time-evolution of the time-derivatives of the pump pulse intensity and the THz synchrotron radiation field.

Prior to the metasurface fabrication, a 7 mm x 15 mm rectangle was cut from a double-side-polished $LiTaO_3$ wafer of 1 mm thickness, resulting in a substrate with dimensions 13 mm × 1 mm × 7 mm parallel to respectively the *z*, *x*, and *y* directions as defined in Fig. 5.7b. The optic axis of $LiTaO_3$ is parallel to the *z* axis. The shorter 7 mm length was necessary so that a tightly-focused probe pulse could propagate parallel to the crystal's y-axis and pass through the 1 mm-wide sides without obstruction. To facilitate both imaging and orthogonal pump-probe measurements, all four of the sides of the $LiTaO_3$ crystal with 1 mm width were polished down to optical quality. Details concerning the preparation and polishing of the substrate are described in Section 2.4. The 500 μm x 500 μm metasurface was then fabricated onto the processed $LiTaO_3$ substrate using an electron-beam lithography and lift-off technique A schematic describing the positioning of the metasurface and a scanning electron microscope image of the nanoantennas are shown in Figure 5.7(b).

The fabrication of the nanoantennas was carried out by Di Wang at Purdue University. 150 nm of poly(methylmethacrylate) (PMMA) was spin-coated onto the $LiTaO_3$ substrate, followed by deposition of 5 nm of chromium (Cr) to serve as a charge distribution layer for electron-beam lithography (EBL), which was used to define the nanoantenna pattern in the positive PMMA resist. Following the completion of EBL, the Cr was removed in CR-16 Chrome Etch. The PMMA was then developed in a 1:3 methyl isobutyl ketone: isopropanol (MIBK:IPA) solution. Finally, 3 nm of titanium followed by 30 nm of gold were electron-beam evaporated. The PMMA was lifted-off using acetone and IPA, leaving the gold nanoantenna pattern on the $LiTaO_3$ substrate.

5.8. Imaging Accelerating Beams in $LiTaO_3$

In order to carry out the measurements discussed in the following sections, it was essential to be able to image the accelerating beams generated by the metasurface. The imaging setup, which is integrated into the orthogonal pump-probe setup discussed below, is shown in Figure 5.7(c). It is the same setup that was used to image the accelerating beams in the glass substrates in Chapter 4. However, imaging the accelerating beams produced inside the $LiTaO_3$ crystals proved to be considerably more challenging than the imaging of the beams inside the glass substrates. First, the nanoantennas fabricated onto the $LiTaO_3$ substrates were not as ideal as those fabricated onto the glass substrates, see Figure 5.8 for comparison. This likely reduced the efficiency of the scattering of the incident light into the accelerating beam.

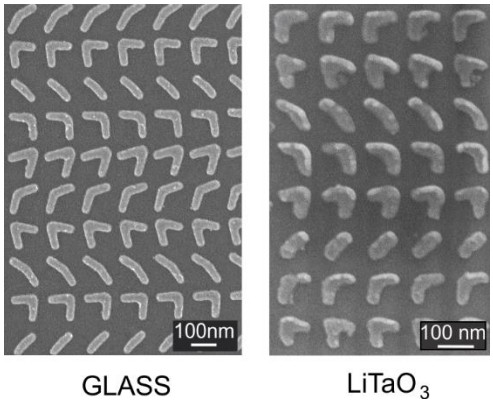

Figure 5.8. Scanning electron microscope images of the nanoantennas fabricated onto glass and $LiTaO_3$ substrates.

Another problem I encountered was the presence of "crack"-like structures that were illuminated whenever a beam of any type passed through the $LiTaO_3$ crystal, see Figure 5.9(a). I have never positively identified these structures, but I assume they are some type of defect. I conducted some preliminary pump-probe measurements with a non-accelerating pump in a standard differential transmission geometry. I performed the measurements on areas inside the

crystal that had both large and small densities of cracks, and I found no difference in the results as can be seen in Figure 5.9(b). Thus, the presence of these cracks makes imaging inside the crystal more difficult, but they do not seem to have a detrimental effect on the generation and detection of THz radiation.

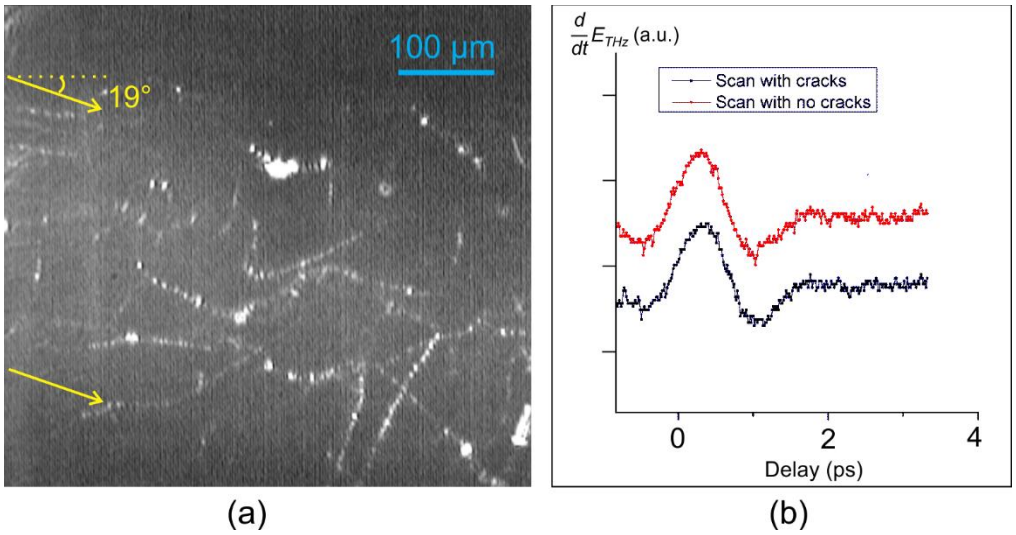

Figure 5.9. (a) Image of an 800 nm beam passing through the $LiTaO_3$ crystal at angle of 19° to the normal of the air-$LiTaO_3$ interface. When illuminated, crack-like structures are seen inside the crystal. (b) Results of a pump-probe measurement on different areas of a $LiTaO_3$ crystal. The presence of cracks does not affect the measurement of the difference-frequency THz radiation.

Although obnoxious, the aforementioned problems were not the primary hurdle I had to overcome in order to obtain images of accelerating beams in $LiTaO_3$. As mentioned earlier, to produce the necessary rectangular substrates, I cut pieces from a 2" $LiTaO_3$ wafer using a dicing saw at the Lurie Nanofabrication Facility. The cut left a roughness on the order of at least a few microns, so I polished both 1 mm-thick *x*-*z* planes of the crystal down to optical quality in order be able to image the accelerating beam through the side of the crystal, as in Chapter 4. However, when I illuminated the metasurface, the CCD showed an image of constant brightness – I could not even image the unperturbed transmission passing through the metasurface. Using an index

card, I was able to observe a specular unperturbed beam emerging *from* the crystal, which suggested that I should have been able to observe a specular beam *inside* the crystal with the camera. When I observed the substrate from afar using the IR viewer, the top and bottom crystal edges were glowing brightly. This indicated to me that higher-order diffraction from the metasurface was striking the two remaining rough crystal edges (the *x*-*y* planes), resulting in an amount of Rayleigh scatter that created a dynamic far too large for the camera to observe the accelerating beam. In retrospect, I did not encounter these problems when taking the first images of accelerating beams produced by metasurfaces in the glass substrates, as the scribing and cleaving process I used to cut the ITO-glass substrates left optically smooth (although not flat) edges which produced a negligible amount of diffuse scattering. Figure 5.10 shows IR viewer images of the substrates while the metasurfaces are illuminated.

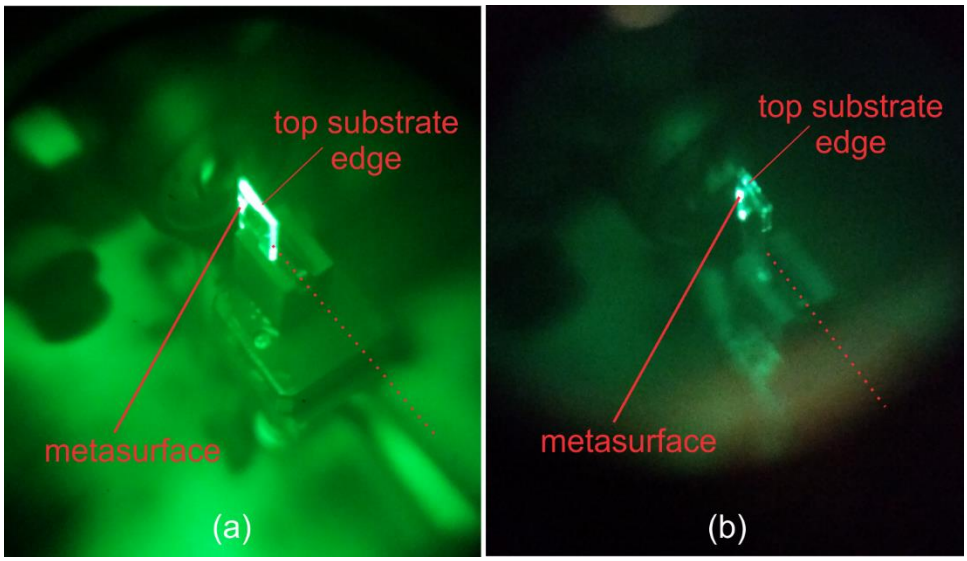

Figure 5.10. Images of the substrates while the metasurfaces are illuminated, as seen through an IR viewer. The two edges of the substrate which are polished lie normal to the red dotted lines. (a) $LiTaO_3$ substrate with unpolished top and bottom edges (the bottom edge is not seen in the photo). The diffuse scattering from these edges creates a large background inside the sample which makes it impossible to image specular beams inside the substrate (b) Glass substrate

with optically smooth top and bottom edges. In this case, there is very little diffuse scatter from the top and bottom edges of the substrate, making it possible to image the accelerating beams.

Thus, it was necessary to polish all four of the 1 mm-thick substrate edges in order to be able to image accelerating beams in the $LiTaO_3$ crystals. Upon completion of this arduous task, I was able to eliminate the unwanted scattering shown in Figure 5.10(a). Images of beams accelerating inside $LiTaO_3$ are shown in Figure 5.11.

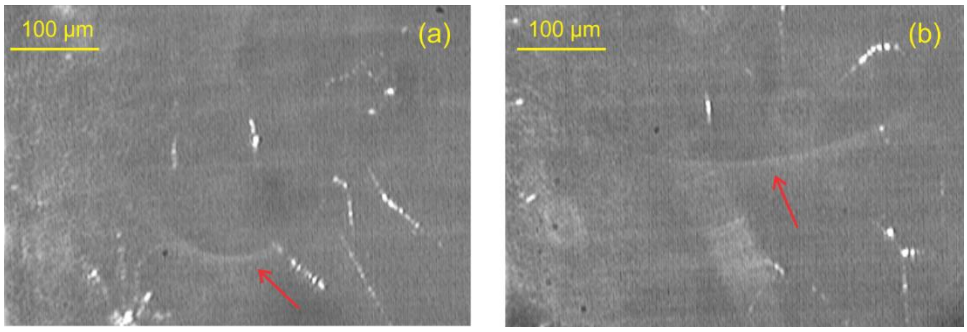

Figure 5.11. Images of metasurface-produced accelerating beams in $LiTaO_3$ with radii of curvature of (a) 100 μm and (b) 400 μm.

5.9. Spatially-Resolved Orthogonal Pump Probe Measurements of the Accelerating Light Pulse and Resulting Synchrotron Radiation

The accelerating pulse was generated by illuminating the metasurface with a pulse of 800 nm central wavelength and duration of 100 fs from a regeneratively amplified Ti: Sapphire oscillator operating at the repetition rate of 250 kHz. We performed a spatially-resolved pump-probe experiment in the differential transmission geometry to detect the THz radiation generated by the accelerating pulse. The experimental setup is shown in Figure 5.7(c). The probe pulse is polarized parallel to the optical (z) axis while the polarization of the accelerating pump lies in the x-z plane and rotates as the pulse propagates. The probe beam directed to the sample was focused

to a spot of diameter 10 μm FWHM (full-width-half-maximum) in the plane of the accelerating beam trajectory. The probe's focusing lens was mounted onto a motorized translation stage, allowing for the translation of the focal spot throughout the acceleration plane. To calibrate the position of the probe, the accelerating and focused probe beams were first imaged together using the imaging setup. The transmitted probe was then directed to a balanced photodetector at which its average intensity was subtracted from that of the reference beam. The focal spot was translated throughout a $400 \times 400\ \mu m^2$ area of the accelerating beam plane in steps of 10 μm. At each position, the arrival time of the probe pulse was delayed in steps of 53.4 fs, and the corresponding differential intensity trace was recorded. The output of a completed measurement is an image sequence showing the propagation of the time-derivatives of the 800 nm pump pulse intensity and THz synchrotron field. Further details concerning the experiment and the processing of the data are presented in Section 2.5.

Figure 5.12 (a)-(c) displays contour plots of calculations of the accelerating pump pulse at different positions along the beam trajectory. The plots were generated by evaluating the expression for $\left|\boldsymbol{E}_p\right|^2$ and taking the time derivative of the intensity envelope. Figure 5.12(d) shows an image of the accelerating beam trajectory obtained from the pump-probe measurement. In all images, the portion of the incident pulse which passes through the metasurface unperturbed was removed. This pulse also generates a negligible amount of THz radiation. The processing of the data is described in Section 2.5.

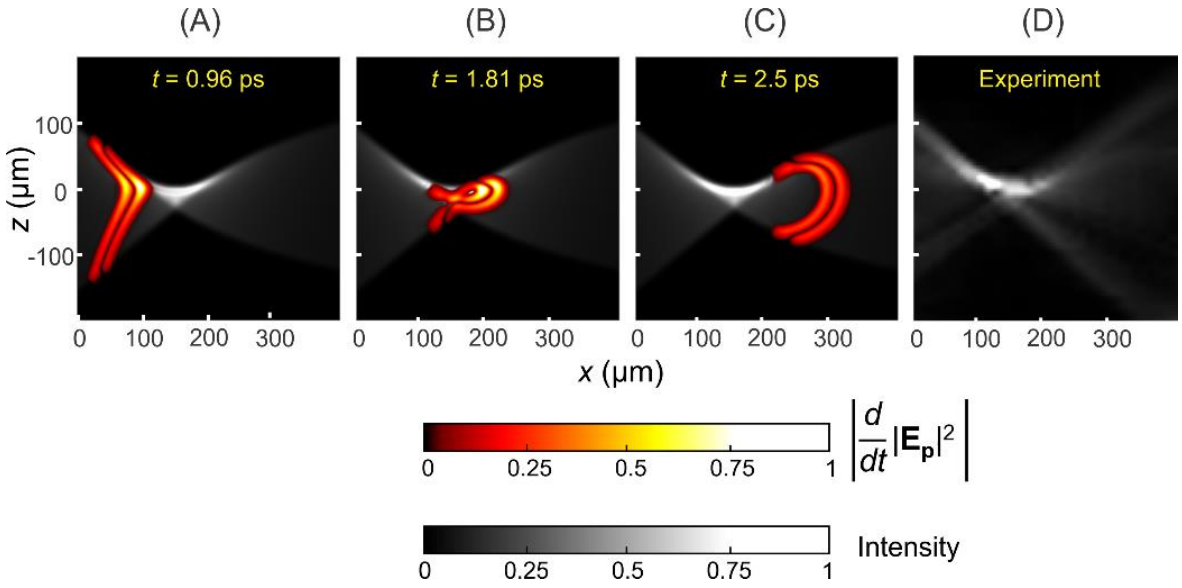

Figure 5.12 Accelerating pump pulse. (A) – (C) Contour plots showing the calculated magnitude of the time derivative of the pump-pulse intensity, $\left|\mathbf{E}_{\mathrm{P}}\right|^2$, and the intensity for continuous wave excitation at 800 nm. To compare with the experimental data, results were numerically convolved with a Gaussian function with 10 μm FWHM. (D) Image of the accelerating beam trajectory obtained by adding the series of experimental traces for $\left|d\left|\mathbf{E}_{\mathrm{P}}\right|^2/dt\right|$.

Figure 5.13 shows contour plots of the time-derivatives of the THz electric field and pump intensity for four different arrival times of the probe with corresponding theory. The contour plots for the theory were generated by taking the time derivatives of the solution to eq. 5.35 and the calculated accelerating pulse intensity. The two-dimensional matrix for each plot was then convolved with a Gaussian function of 10 μm FWHM to account for the size of the probe's focal spot. The complete image sequence showing the time-evolution of the pump pulse and synchrotron field is presented in the supplementary media.

Consistent with the optical properties of $LiTaO_3$, the 800 nm pulse propagates at a speed that is approximately three times greater than that for the THz synchrotron field. Both theoretical and measured THz fields show the presence of inner $(\rho < 100\ \mu\mathrm{m})$ and outer $(\rho > 100\ \mu\mathrm{m})$

radiation branches, typical of synchrotron radiation for $v > c/n$; $\rho = (x^2 + z^2)^{1/2}$. As discussed in section 5.4, another feature of superluminal speeds is the formation of a cusp in the inner radiation branch [113,114]. Simulations of a single charge revolving in a circular trajectory show that the cusp begins to form considerably after the charge makes one half of a revolution. The 800 nm pulse in the experiment completes between one quarter and one half of a revolution, resulting in a slight cusp in the inner synchrotron radiation branch that can be seen in Figure 5.13 at t = 4.01 ps near (x, z) = (200 μm, 100 μm).

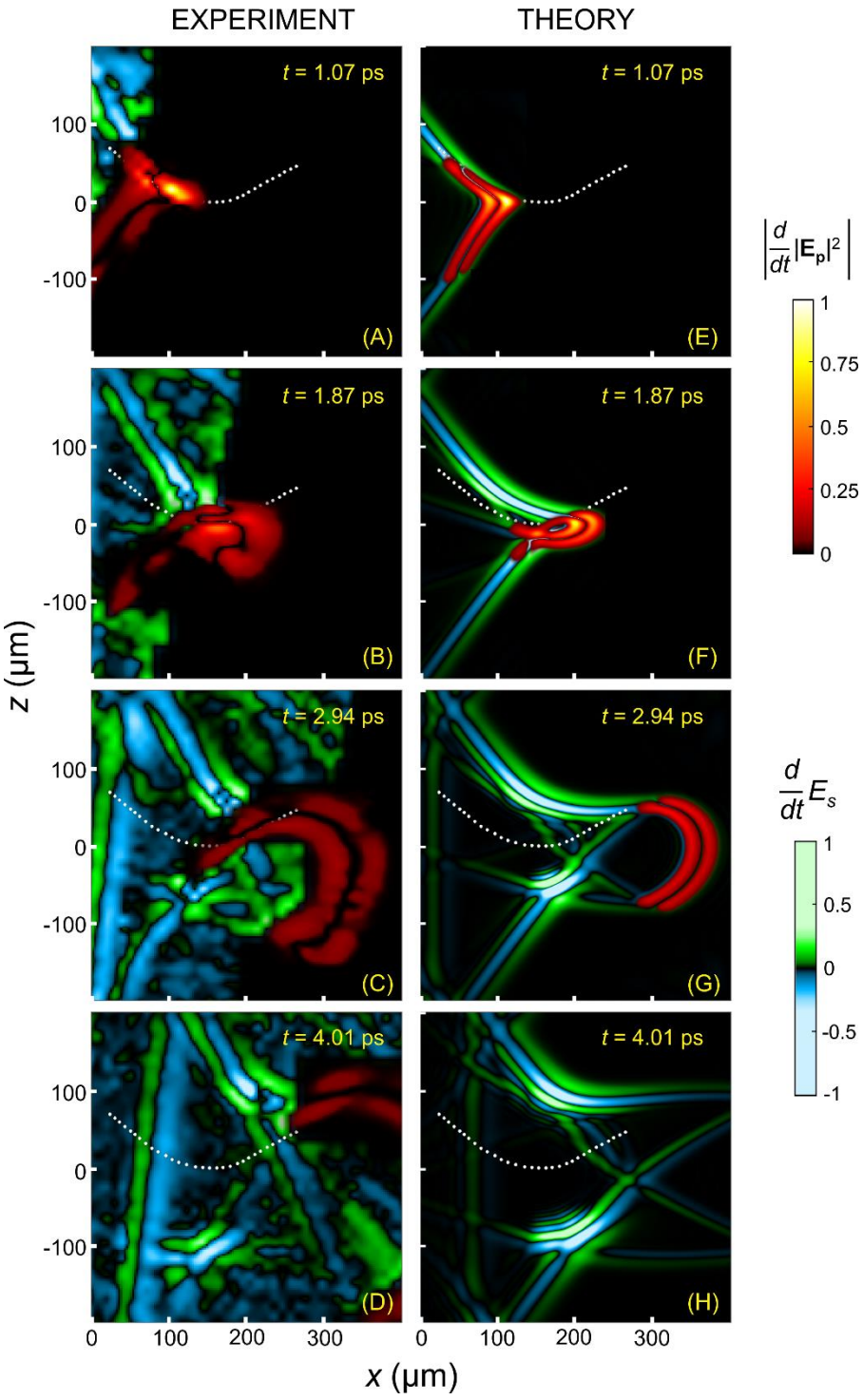

Figure 5.13. Synchrotron radiation from the accelerating pulse. (A) – (D) Contour plots showing results of the orthogonal pump-probe measurements. The signal proportional to the time-derivatives of the pump intensity $|\mathbf{E}_P|^2$ and that of the THz field, E_S, were isolated and plotted on

separate scales. (E) - (G) Contour plots of the theoretical $\left| d\left|\mathbf{E}_{\mathrm{P}}\right|^2 / dt \right|$ and E_S. The dashed-white curve is the trajectory derived from calculations of the pump intensity.

5.10. Summary

We present the first demonstration of synchrotron radiation from an accelerating nonlinear polarization. The 100 μm scale over which the radiation is produced is the smallest to date, and the superluminal speed of the polarization increases the radiated power considerably. These results are the first step towards the realization of on-chip monochromatic synchrotron radiation. The orthogonal pump-probe measurement outputs an image sequence which shows the evolution of both, the accelerating pump pulse and the resulting synchrotron radiation. This method for imaging THz fields and the intensities of optical pulses can certainly be extended to other materials and excitation geometries.

CHAPTER 6
CONCLUSION

"The vagabond who's rappin' at your door,

is standing in the clothes that you once wore.

Strike a match and go start anew,

'cause it's all over now, Baby Blue."

- Bob Dylan, "*It's All Over Now, Baby Blue"*

In each of the studies presented in this work, we used a metamaterial device to dramatically alter the properties of ordinary light beams. In Chapter 3, we learned of a structure that, for a few frequencies, can perfectly transmit light through two consecutive sub-wavelength apertures, despite the transmission through a single sub-wavelength aperture being remarkably small. We measured the aperture-bound resonances at THz frequencies and obtained data which showed that the slotted plates hold promise for on-chip THz spectrometers. In Chapter 4, we used metasurfaces to generate highly-curved beams over hundred-micron length scales inside glass, something that cannot be achieved with conventional optics systems. This allowed for the acceleration of a laser pulse over a hundred micron-scale circular arc in $LiTaO_3$ and subsequently, the first observation of synchrotron radiation generated from a nonlinear polarization. This generation of synchrotron radiation over a scale of 100 μm is the smallest to date.

The physics that is demonstrated when performing experiments with metamaterials is interesting and remarkable in its own right. Nevertheless, this ability to control light with a single compact optic is accompanied with the prospect of on-chip THz spectrometers, micron-scale platforms for accelerating light, and chip-sized synchrotrons for continuous-wave THz generation. The promise of such applications generates a strong interest in metamaterials from the broader scientific community, thus providing additional incentives for their further study and development. As such, I will now provide some directions for future investigation.

6.1. The On-Chip THz Slotted Waveguide Spectrometer: Future Directions

The resonance lifetimes observed in THz-TDS experiments were considerably less than those predicted by theory, which we attribute largely to imperfections in the plates' alignment. Future work involving the precise parallelization of the plates (< 0.1°) and the subsequent characterization of the resonances is the next step towards the development of a polished spectrometer. One way to achieve precise plate alignment is to simply fix the plate separation by fabricating the slotted plates onto a substrate of pre-determined thickness and flatness. In this case, care must be taken to choose a low-loss substrate; high resistivity float zone silicon could be an appropriate choice.

6.2. Future Directions for Metasurface-Produced Accelerating Light

The V-Antennas were chosen as the metasurface constituent, in part, because these metasurfaces are one of the simplest to fabricate. As discussed in both, Chapter 4 and Chapter 5, a considerable portion (~ 50 %) of the light that impinges upon the V-antenna metasurfaces passes

through the metasurface unperturbed. This could be eliminated by using a Huygens metasurface as an alternative. Huygens metasurfaces [115,116] present an advantage over the V-antennas in that they allow control of the phase of both, cross-polarized and co-polarized scattered fields. Unlike the V-antenna arrays, which only provide control of the electric polarization, Huygens metasurfaces grant also manipulation of the magnetic response [115,116]. This leads in particular to a significant reduction in the intensity of the unperturbed transmitted and reflected co-polarized beams. However, the design required for control of the magnetic response at near-infrared wavelengths involves stacks of patterned metallic sheets [116], which adds complexity to the fabrication process.

6.3. Future Directions for Light-Produced Synchrotron Radiation.

In order to realize highly-monochromatic on-chip THz synchrotron radiation, it is necessary that the light pulse completes many revolutions about a circular trajectory. One possible method for achieving this is to couple a sub-ps pulse to the whispering gallery modes [117-119] of a bulk nonlinear crystal shaped into a sphere, disk, or toroid with dimensions of a hundred microns or less. Light coupled to such modes can make well over 10^6 round trips along a circular trajectory [117-119]. Thus, the proposed structure has the potential to function as an on-chip synchrotron and thus a source of highly-monochromatic THz radiation.

APPENDIX

A.1. Script Used to Calculate the Accelerating Light Pulse and Resulting Synchrotron Radiation in $LiTaO_3$

This script is written for execution in Mathematica. As the matrices involved are quite large, the script was submitted to run under the Mathematica module supported by the high performance computing cluster (HPC) at the University of Michigan. For the input parameters shown below, the script required 300 GB of RAM to successfully run, and it finished execution after roughly 24 hours.

This script has three main parts. First, it calculates the accelerating pulse intensity produced by the metasurface, the time-averaged accelerating beam intensity for each frequency of the incident pulse, and the nonlinear polarization for each frequency within the THz bandwidth. 3D matrices corresponding to each of these quantities are then stored to file.

Second, it uses the accelerating pulse intensity to calculate the real and imaginary components of the THz synchrotron field. These matrices are then stored to file.

Finally, the script convolves the accelerating pulse intensity and the real part of the THz synchrotron field with a Gaussian function of full-width of half maximum of ~ 10 μm to account for the focal size of the experimental probe pulse. In addition, it averages the pulse and synchrotron field over the 150 fs it takes for the probe pulse to pass through the fields. This, however, is a small effect compared to the loss in resolution due to the 10 μm focal spot of the probe. The results are stored to file.

```
LaunchKernels[1]

xmax=250.2*10^-6;
xmin=-250.02*10^-6;
xstep=-0.18*10^-6;
xlength=Length[Table[0,{x,xmax,xmin,xstep}]];

zmax=250*10^-6;
zmin=-299.82*10^-6;
zstep=0.18*10^-6;
zlength=Length[Table[0,{z,zmin,zmax,zstep}]];

fmin=3.6563*10^14;
fmax=3.8437*10^14;
fstep=0.00075*10^14;
flength=Length[Table[0,{f,fmin,fmax,fstep}]];

If[OddQ[flength],
 f1=(flength-1)/2;
 f2=(flength+1)/2;,
 f1=flength/2;
 f2=flength/2;]

If[OddQ[xlength],
 x1=(xlength-1)/2;
 x2=(xlength+1)/2;,
 x1=xlength/2;
 x2=xlength/2;]

If[OddQ[zlength],
 z1=(zlength-1)/2;
 z2=(zlength+1)/2;,
 z1=zlength/2;
 z2=zlength/2;]

z0=-300*10^-6;
w0=125*10^-6;
gauss[x_]:=Exp[-x^2/w0^2]
```

```
g=Table[gauss[x],{x,xmax,xmin,xstep}];

Print["1"]

lambda=800*10^-9;
alpha=0.01/lambda;
beta=N[1693];
k[f_]:=2.156*2*Pi*f/3/10^8;
k0[f_]:=2*Pi*f/3/10^8;
tau=100*10^-15;
a0=2*Log[2]/tau^2;
f0=3.75*10^14;
Spec[f_]:=Exp[-(2*Pi*f-2*Pi*f0)^2/(4*a0)]
phase[x_,f_]:=Exp[-I*k0[f]*(x-xmax)*Sin[(Pi/180)*(0)]]

phasetab=Table[phase[x,f],{x,xmax,xmin,xstep},{f,fmin,fmax,fstep}];

GFun[z_,x_,f_]:=I*HankelH2[0,k[f]*(x^2+z^2)^(1/2)]
GFunback[z_,x_,f_]:=-I*HankelH1[0,k[f]*(x^2+(z-z0)^2)^(1/2)]

Spectrum=Table[Spec[f],{f,fmin,fmax,fstep}];

GFun2D=Parallelize[Table[GFun[z0,x,3.75*10^14],{x,xmax,xmin,xstep}]];
acc2d=Table[0,{x,xmax,xmin,xstep},{f,fmin,fmax,fstep}];
FinAcc[x_,f_]:=Exp[alpha*x]*UnitStep[-x+beta/k[f]]*BesselJ[beta,-
k[f]*x+beta]

FinAcc1D=Parallelize[Table[FinAcc[x,3.75*10^14],{x,xmax,xmin,xstep}]];

acc2d=InverseFourier[Fourier[FinAcc1D[[1;;All]]]*Fourier[GFun2D[[1;;All]]]
];
acc2d=Join[Take[acc2d[[1;;All]],-(x1)],Take[acc2d[[1;;All]],(x2)]];

Print["2"]
SessionTime[]

a=Table[0,{x,xmax,xmin,xstep},{z,zmin,zmax,zstep},{f,fmin,fmax,fstep}];

Print["3"]
SessionTime[]

For[i = 1; i2 = zmin, i <= zlength, i++; i2 += zstep,
For[l = 1; f3 = fmin, l <= flength, l++; f3 += fstep,
a[[1 ;; All, i, l]] = InverseFourier[Fourier[acc2d[[1 ;;
All]]*phasetab[[1;;All,l]]]*Spectrum[[l]]*Fourier[Table[GFunback[i2, x,
f3], {x, xmax, xmin, xstep}]]];
a[[1 ;; All, i, l]] =Join[Take[a[[1 ;; All, i, l]], -(x1)],Take[a[[1 ;;
All, i, l]], (x2)]];]];

Print["3a"]
SessionTime[]

Clear[GFunback]
Clear[acc2d]
```

```
Clear[phasetab]
Clear[Spectrum]

INT =4;
cnew = Abs[a[[1;;All;;INT,1;;All;;INT,1;;All]]]^2;
Put[cnew,"Pump_at_each_frequency_100umROC_IdealAccBeam_tau100fs_full_image
_phase=0.dat"]
Clear[cnew]
Print["4a"]
SessionTime[]

b=Table[0,{x,xmax,xmin,xstep},{z,zmin,zmax,zstep},{f,fmin,fmax,fstep}];

Print["4b"]
SessionTime[]

For[i=1,i<=zlength,i++,
For[j=1,j<=xlength,j++,
b[[j,i,1;;All]]=Abs[InverseFourier[a[[j,i,1;;All]]]]^2;
b[[j,i,1;;All]]=Join[Take[b[[j,i,1;;All]],-f1],Take[b[[j,i,1;;All]],f2]];
a[[j,i,1;;All]]=Fourier[b[[j,i,1;;All]]];]];

Print[5]
SessionTime[]

bnew = b[[1;;All;;INT,1;;All;;INT,1;;All]];
Clear[b]

Put[bnew,"PumpPulse_Intensity_100umROC_IdealAccBeam_tau100fs_full_image_ph
ase=0.dat"]

Print["5b"]

anew = a[[1;;All;;INT,1;;All;;INT,1;;All]];
Clear[a]
SessionTime[]

Put[anew,"FFTofPulseIntensity_100umROC_IdealAccBeam_tau100fs_full_image_ph
ase=0.dat"]
SessionTime[]

Print[7]

GFun3tab = Get["THzGreenFunction_with_dispersion.dat"];

Print[8]
SessionTime[]

dpdt= Table[(2*Pi*f)^2,{f,-(fmax-fmin)/2,(fmax-fmin)/2,fstep}];
dpdtF = Join[Take[dpdt,-f1],Take[dpdt,f2]];

Print[10]
```

```
GFun3tabF = Table[0,{x,xmax,xmin,xstep*INT},{z,zmin,zmax,zstep*INT},{f,-
(fmax-fmin)/2,(fmax-fmin)/2,fstep}];

Print[11]

xlength = Length[Table[0,{x,xmax,xmin,xstep*INT}]];
zlength = Length[Table[0,{z,zmin,zmax,zstep*INT}]];

If[OddQ[xlength],
x1 = (xlength-1)/2;
x2 = (xlength+1)/2;,
x1 = xlength/2;
x2 = xlength/2;]

If[OddQ[zlength],
z1 = (zlength-1)/2;
z2 = (zlength+1)/2;,
z1 = zlength/2;
z2 = zlength/2;]

For[i=1,i<=zlength,i++,
For[j=1,j<=xlength,j++,
GFun3tabF[[j,i,1;;All]]=Join[Take[GFun3tab[[j,i,1;;All]],-
f1],Take[GFun3tab[[j,i,1;;All]],f2]];]];

Print[12]

For[i=1,i<=zlength,i++,
For[l=1,l<=flength,l++,
anew[[1;;All,i,l]]=Fourier[anew[[1;;All,i,l]]];]];

Print[13]

For[j=1,j<=xlength,j++,
For[l=1,l<=flength,l++,
anew[[j,1;;All,l]]=Fourier[anew[[j,1;;All,l]]];]];

Print[14]

For[j=1,j<=xlength,j++,
For[l=1,l<=flength,l++,
GFun3tabF[[j,1;;All,l]]=Fourier[GFun3tabF[[j,1;;All,l]]];]];

Print[15]

For[i=1,i<=zlength,i++,
For[l=1,l<=flength,l++,
GFun3tabF[[1;;All,i,l]]=Fourier[GFun3tabF[[1;;All,i,l]]];]];

Print[16]

For[i=1,i<=zlength,i++,
For[j=1,j<=xlength,j++,
For[l=1,l<=flength,l++,
```

```
anew[[j,i,l]]=GFun3tabF[[j,i,l]]*anew[[j,i,l]]*dpdtF[[l]];]]];

Print[17]

For[j=1,j<=xlength,j++,
For[l=1,l<=flength,l++,
anew[[j,1;;All,l]]=InverseFourier[anew[[j,1;;All,l]]];]];

Print[18]

For[i=1,i<=zlength,i++,
For[l=1,l<=flength,l++,
anew[[1;;All,i,l]]=InverseFourier[anew[[1;;All,i,l]]];
anew[[1;;All,i,l]]=Join[Take[anew[[1;;All,i,l]],-
(x1)],Take[anew[[1;;All,i,l]],(x2)]];]];

Print[19]

For[i=1,i<=zlength,i++,
For[j=1,j<=xlength,j++,
anew[[j,i,1;;All]]=InverseFourier[anew[[j,i,1;;All]]];]]

Print[20]

Put[Re[anew],"THz_Field_100umROC_IdealAccbBeam_full_image_with_dispersion_
phase=0_RealPart.dat"]
Put[Im[anew],"THz_Field_100umROC_IdealAccbBeam_full_image_with_dispersion_
phase=0_ImagPart.dat"]

SessionTime[]

pumppulse = bnew[[1;;All,1;;All,140;;240]];
THz = Re[anew[[1;;All,1;;All,140;;240]]];

Clear[bnew]
Clear[anew]

Print[1]

THzTDer = Table[0,{x,1,695,1},{z,1,764,1}];
PumpTDer =  Table[0,{x,1,695,1},{z,1,764,1}];

Print[2]

For[j=1,j<=695,j+=1,
For[i=1,i<=764,i+=1,
THzInt= ListInterpolation[THz[[j,i,1;;All]]];
THzTDer[[j,i]]= Table[Derivative[1][THzInt][t],{t,1,101}];]]

Print[3]

For[j=1,j<=695,j+=1,
For[i=1,i<=764,i+=1,
PumpInt= ListInterpolation[pumppulse[[j,i,1;;All]]];
```

```
PumpTDer[[j,i]]= Table[Derivative[1][PumpInt][t],{t,1,101}];]]

Print[4]

start = 2;
end = 100;
THzTAvg = ToExpression["x"<>ToString[#]]&/@Range[end-start+1];
PumpTAvg = ToExpression["x"<>ToString[#]]&/@Range[end-start+1];

Print[5]

For[p=start;p1=1, p<=end, p+=1;p1+=1,
THzTAvg[[p1]]=Sum[THzTDer[[1;;All,1;;All,p]],{p,p-1,p+1,1}];
PumpTAvg[[p1]]=Sum[PumpTDer[[1;;All,1;;All,p]],{p,p-1,p+1,1}];]

Print[6]

PSF = Table[Exp[-2*(x^2+z^2)/(8.5^2)],{x,250.2,-250.02,-0.18*4},{z,-
299.82,250,0.18*4}];

Print[7]

THzTAvgAndConv = ToExpression["x"<>ToString[#]]&/@Range[end-start+1];
PumpTAvgAndConv = ToExpression["x"<>ToString[#]]&/@Range[end-start+1];

Print[8]

For[t1=1,t1<=(end-start+1),t1+=1,
THzTAvgAndConv[[t1]] =
ListConvolve[PSF,THzTAvg[[t1]][[1;;All,1;;All]],{{347,417},{347,417}}];
PumpTAvgAndConv[[t1]]=ListConvolve[PSF,PumpTAvg[[t1]][[1;;All,1;;All]],{{3
47,417},{347,417}}];
Print[t1];
Print[SessionTime[]];]

Print[9]

Put[PumpTAvgAndConv,"Pump_Pulse_SpaceAndTime_Convolved.dat"]
Put[THzTAvgAndConv,"ReTHz_SpaceAndTime_Convolved.dat"]

Print[10]
```

A.2. Script for Generating Green's Function Matrix (input for script in A.1.)

The script below generates the Green's Function matrix necessary for calculating the THz synchrotron field. The output of this script serves as the input for the previous script. This script was executed on the HPC cluster.

```
LaunchKernels[12]

xmax = 250.2*10^-6;
xmin = -250.02*10^-6;
xstep = -0.18*10^-6;
xlength = Length[Table[0,{x,xmax,xmin,xstep}]];

zmax = 250*10^-6;
zmin = -299.82*10^-6;
zstep = 0.18*10^-6;
zlength = Length[Table[0,{z,zmin,zmax,zstep}]];

fmin = 3.6563*10^14;
fmax = 3.8437*10^14;
fstep =0.00075*10^14;
flength = Length[Table[0,{f,fmin,fmax,fstep}]];

If[OddQ[flength],
f1 = (flength-1)/2;
f2 = (flength+1)/2;,
f1 = flength/2;
f2 = flength/2;]

If[OddQ[xlength],
x1 = (xlength-1)/2;
x2 = (xlength+1)/2;,
x1 = xlength/2;
x2 = xlength/2;]

If[OddQ[zlength],
z1 = (zlength-1)/2;
z2 = (zlength+1)/2;,
z1 = zlength/2;
z2 = zlength/2;]

z0 = -300*10^-6;
INT = 4;

(*k[f_]:=6.3*2*Pi*f/3/10^8*)
(*GFun3[x_,z_,f_]:=-I*HankelH1[0,k[f]*(x^2+(z-z0)^2)^(1/2)]*)

epsInf=4.527;
epsDC=37.6;
fTO1=6*10^12;
fTO2 = 10.71*10^12;
```

```
fTO3 = 17.88*10^12;
fTO4 = 19.71*10^12;
fTO5 = 22.8*10^12;
gamma1 = 8.4*10^11;
gamma2 = 3.3*10^11;
gamma3 = 5.4*10^11;
gamma4 = 1.68*10^12;
gamma5 = 1.32*10^12;
C1=30;
C2=0.005;
C3 =2.66;
C4=0.34;
C5=0.02;
epsilon[f_]:=epsInf+C1*(fTO1)^2/((fTO1)^2-(f)^2-
I*gamma1*f)+C2*(fTO2)^2/((fTO2)^2-(f)^2-I*gamma2*f)+C3*(fTO3)^2/((fTO3)^2-
(f)^2-I*gamma3*f)+C4*(fTO4)^2/((fTO4)^2-(f)^2-
I*gamma4*f)+C5*(fTO5)^2/((fTO5)^2-(f)^2-I*gamma5*f)
k[f_]:=epsilon[f]^(1/2)*2*Pi*f/3/10^8
GFun3[x_,z_,f_]:=-I*HankelH1[0,k[f]*(x^2+(z-z0)^2)^(1/2)]

Print[9]

GFun3tab =
Parallelize[Table[GFun3[x,z,f],{x,xmax,xmin,xstep*INT},{z,zmin,zmax,zstep*
INT},{f,-(fmax-fmin)/2,(fmax-fmin)/2,fstep}]];

Print[10]

Put[GFun3tab,"THzGreenFunction_with_dispersion.dat"]

Print[11]
```

A.3. Script for Evaluating the Liénard-Wiechert Potentials

This script evaluates the Liénard-Wichert potentials for a charge moving along a circular trajectory and finds the corresponding terms for the radiated electric field. It is written for execution in Mathematica, which can be carried out on a PC. The electric and magnetic vector potential contributions to the electric field are stored to separate files.

```
LaunchKernels[1]

R=25*10^-6;
n=6.3
```

```
c=3*10^8/n;
w =6*c/R;
q=1.6*10^-19;
μ0= 4*Pi*10^-7;
ϵ0 = 8.85*10^-12;
r[x_,y_,t1_]:=(x^2+y^2-2*R*(-x*Cos[w*t1]-y*Sin[w*t1])+R^2)^(1/2)
vx[x_,y_,t1_]:= R*w*Sin[w*t1]
vy[x_,y_,t1_]:=-R*w*Cos[w*t1]
nv[x_,y_,t1_]:= ((x+R*Cos[w*t1])*R*w*Sin[w*t1]-
(y+R*Sin[w*t1])*R*w*Cos[w*t1])/r[x,y,t1]
ϕ[x_,y_,t1_]:=q/(4*Pi*ϵ0*n^2 )/(r[x,y,t1]*(1-1/c*nv[x,y,t1])*r[x,y,t1]*(1-
1/c*nv[x,y,t1]))^(1/2)
Ax[x_,y_,t1_]:=(q*μ0/(4*Pi))*vx[x,y,t1]/(r[x,y,t1]*(1-
1/c*nv[x,y,t1])*r[x,y,t1]*(1-1/c*nv[x,y,t1]))^(1/2)
Ay[x_,y_,t1_]:=(q*μ0/(4*Pi))*vy[x,y,t1]/(r[x,y,t1]*(1-
1/c*nv[x,y,t1])*r[x,y,t1]*(1-1/c*nv[x,y,t1]))^(1/2)
charge[x_,y_,t1_]:=Exp[-(x-R*Cos[w*t1])^2/(2^2)]*Exp[-(y-
R*Sin[w*t1])^2/(2^2)]*(vx[x,y,t1]+vy[x,y,t1])

g[t1_]:=(x^2+y^2-2*R*(-x*Cos[w*t1]-y*Sin[w*t1])+R^2)
f[t1_]:=c^2*(t^2-2*t*t1+t1^2)

xmin =-50*10^-6;
xmax = 50*10^-6;
xstep = 0.5*10^-6;

ymax=50*10^-6;
ymin = -50*10^-6;
ystep = -0.5*10^-6;

tmin = 0.025*10^-12;
tmax = 0.55*10^-12;
tstep = 0.025*10^-12;


phiC=
Table[0,{y,ymax,ymin,ystep},{x,xmin,xmax,xstep},{t,tmin,tmax,tstep}];
AxC=
Table[0,{y,ymax,ymin,ystep},{x,xmin,xmax,xstep},{t,tmin,tmax,tstep}];
AyC =
Table[0,{y,ymax,ymin,ystep},{x,xmin,xmax,xstep},{t,tmin,tmax,tstep}];

For[t=tmin;a=1,t<=tmax,t+=tstep;a++,
For[x=xmin;i=1,x<=xmax,x+=xstep;i++,
phiI =0;
AxI=0;
AyI=0;
For[y=ymax;j=1,y>=ymin,y+=ystep;j++,
phiI =0;
AxI=0;
AyI=0;
For[t1=0*10^-12,t1<t,t1+=0.0025*10^-12,
If[Abs[g[t1]-f[t1]]/((g[t1]+f[t1])/2)<0.1,
phiI=phiI+ϕ[x,y,t1];
```

```
AxI=AxI+Ax[x,y,t1];
AyI= AyI+Ay[x,y,t1]]];
phiC[[j,i,a]]=phiI;
AxC[[j,i,a]]=AxI;
AyC[[j,i,a]]=AyI;]];
Print[t]]

phiCInt=ListInterpolation[phiC[[1;;All,1;;All,1;;Length[phiC[[1,1,1;;All]]
]]]];

AxCInt =
ListInterpolation[AxC[[1;;All,1;;All,1;;Length[phiC[[1,1,1;;All]]]]]];

AyCInt =
ListInterpolation[AyC[[1;;All,1;;All,1;;Length[phiC[[1,1,1;;All]]]]]]


Eϕx=Table[Derivative[0,1,0][phiCInt][y,x,t],{y,1,Length[phiC[[1;;All,1,1]]
]},{x,1,Length[phiC[[1,1;All,1]]]},{t,1,Length[phiC[[1,1,1;;All]]]}]/xstep
;
Eϕy=Table[Derivative[1,0,0][phiCInt][y,x,t],{y,1,Length[phiC[[1;;All,1,1]]
]},{x,1,Length[phiC[[1,1;All,1]]]},{t,1,Length[phiC[[1,1,1;;All]]]}]/ystep
;
Axdt=Table[Derivative[0,0,1][AxCInt][y,x,t],{y,1,Length[phiC[[1;;All,1,1]]
]},{x,1,Length[phiC[[1,1;All,1]]]},{t,1,Length[phiC[[1,1,1;;All]]]}]/tstep
;
Aydt=Table[Derivative[0,0,1][AyCInt][y,x,t],{y,1,Length[phiC[[1;;All,1,1]]
]},{x,1,Length[phiC[[1,1;All,1]]]},{t,1,Length[phiC[[1,1,1;;All]]]}]/tstep
;

Put[Eϕx,"EphiX.dat"]

Put[Eϕy,"EphiY.dat"]

Put[Axdt,"AxDt.dat"]

Put[Aydt,"AyDt.dat"]
```

BIBLIOGRAPHY

[1] A. Pinczuk, Jagdeep Shah, and P. A. Wolff, Phys. Rev. Lett. **47**, 1487 (1981).

[2] P. Padmanabhan, S. M. Young, M. Henstridge, S. Bhowmick, P. K. Bhattacharya, and R. Merlin, Phys. Rev. Lett. **113**, 027402 (2014).

[3] F. Huang, B. Schulkin, H. Altan, J. F. Federici, D. Gary, R. Barat, D. Zimdars, M. Chen, and D. B. Tanner, App. Phys. Lett. **85**, 5535 (2004).

[4] L. Chu and Y. Lee, J. Chem. Phys. **126**, 134311 (2007).

[5] M. C. Beard, W. T. Lotshaw, T. M. Korter, and E. J. Heilweil, J. Phys. Chem. A **108**, 9348 (2004).

[6] M. Tonouchi, Nat. Photon. **1**, 97 (2007).

[7] E. Pickwell and V. P. Wallace, J. Phys. D: Appl. Phys. **39**, R301 (2006).

[8] J. F. Federici, B. Schulkin, F. Huang, D. Gary, R. Barat, F. Oliveira, and D. Zimdars, Semicond. Sci. Technol. **20**, S266 (2005).

[9] A. Dobroiu, C. Otani, and K. Kawase, Meas. Sci. Technol. **17**, R161 (2006).

[10] C. Kulesa, IEEE Trans. THz Sci. Technol. **1**, 232 (2011).

[11] P.H. Siegel, IEEE Trans. Antennas Propag. **55**, 2957 (2007).

[12] G. J. Stacey, IEEE Trans. THz. Sci. Technol. **1**, 241 (2011).

[13] B. C. Smith, *Fundamentals of Fourier Transform Spectroscopy* (CRC Press 2011).

[14] M. van Exter, Ch. Fattinger, and D. Grischkowsky, Opt. Lett. **14**, 1128 (1989).

[15] A. Dreyhaupt, S. Winnerl, T. Dekorsy, and M. Helm, Appl. Phys. Lett. **86**, 121114 (2005).

[16] R. J. B. Dietz, N. Vieweg, T. Puppe, A. Zach, B. Globisch, T. Gobel, P. Leisching, and M. Schell, Opt. Lett. **39**, 6482 (2014).

[17] D. H. Auston, K. P. Cheung, J. A. Valdmanis, and D. A. Kleinman, Phys. Rev. Lett. **53**, 1555 (1984).

[18] I. D. Vugmeyster, J. F. Whitaker, and R. Merlin, App. Phys. Lett. **101**, 181101 (2012).

[19] I-Chen Ho, X. Guo, and X. C. Zhang, Opt. Express **18**, 2872 (2010).

[20] E. Matsubara, M. Nagai, and M. Ashida, J. Opt. Soc. Am. B **30**, 1627 (2013).

[21] A. Roggenbuck, H. Schmitz, A Deninger, I. Cámara Mayorga, J. Hemberger, R. Güsten, and M. Grüninger, New J. Phys. **12**, 043017 (2010).

[22] A. J. Deninger, A. Roggenbuck, S. Schindler, and S. Preu, J. Infrared Milli. Terahz Waves **36**, 269 (2014).

[23] P. A. George, W. Hui, F. Rana, B. G. Hawkins, A. E. Smith, and B. J. Kirby, Opt. Express **16**, 1577 (2008).

[24] T. Ohkubo, M. Onuma, J. Kitagawa, and Y. Kadoya, App. Phys. Lett. **88**, 212511 (2006).

[25] D. M. Mittleman, R. H. Jacobsen, R. Neelamani, R. G. Baraniuk, and M. C. Nuss, Appl. Phys. B **67**, 379 (1998).

[26] Y. Hsieh, S. Nakamura, D. G. Abdelsalam, T. Minamikawa, Y. Mizutani, H. Yamamoto, T. Iwata, F. Hindle, and T. Yasui, Sci. Rep. **6**, 28114 (2016).

[27] D. L. Woolard, E. R. Brown, A. C. Samuels, J. O. Jensen, T. Globus, B. Gelmont, and M. Wolski, in *2003 IEEE MTT-S International Microwave Symposium Digest* (IEEE, 2003), p. 763.

[28] J. Durnin and J. J. Miceli, Jr., Phys. Rev. Lett. **58**, 1499 (1987).

[29] J. Durnin, J. Opt. Soc. Am. A **4,** 651 (1987).

[30] C. A. Dartora, M. Zamboni-Rached, K.Z. Nóbrega, E. Recami, and H. E. Hernández-Figueroa, Opt. Commun. **222**, 75 (2003).

[31] E. Hecht, *Optics* (Pearson, San Francisco, 2002), 4th ed., pp. 107-109.

[32] E. Hecht, *Optics* (Pearson, San Francisco, 2002), 4th ed., pp. 273-276.

[33] P. Zhang, J. Prakash, Z. Zhang, M. S. Mills, N. K. Efremidis, D. N. Christodoulides, and Z. Chen, Opt. Lett. **36**, 2883 (2011).

[34] J. Baumgartl, M. Mazilu, and K. Dholakia, Nat. Photonics **2,** 675 (2008).

[35] A. Mathis, F. Courvoisier, L. Froehly, L. Furfaro, M. Jacquot, P. A. Lacourt, and J. M. Dudley, Appl. Phys. Lett. **101**, 071110 (2012).

[36] P. Rose, F. Diebel, M. Boguslawski, and C. Denz, App. Phys. Lett. **102**, 101101 (2013).

[37] P. Polynkin, M. Kolesik, J. V.Moloney, G. A. Siviloglou, D. N.Christodoulides, Science **324**, 229 (2009).

[38] P. Polynkin, M. Kolesik, and J. Moloney, Phys. Rev. Lett. **103**, 123902 (2009).

[39] T. Ellenbogen, N. Voloch-Bloch, A. Ganany-Padowicz and A. Arie, Nat. Phot. **3**, 395 (2009).

[40] F. Diebel, B. M. Bokić, D. V. Timotijević, D. M. Jović Savić, and C. Denz, Opt. Exp. **23**, 24351 (2015).

[41] I. Dolev, I. Kaminer, A. Shapira, M. Segev, and A. Arie, Phys. Rev. Lett. **108**, 113903 (2012).

[42] D. Abdollahpour, S. Suntsov, D. G. Papazoglou, and S. Tzortzakis, Phys. Rev. Lett. **105**, 253901 (2010).

[43] A. Salandrino and D. N. Christodoulides, Opt. Lett. **35,** 2082 (2010).

[44] P. Zhang, S. Wang, Y. Liu, X. Yin, C. Lu, Z. Chen, and X. Zhang, Opt. Lett. **36**, 3191 (2011).

[45] A. Minovich, A. E. Klein, N. Janunts, T. Pertsch, D. N. Neshev, and Y. S. Kivshar, Phys. Rev. Lett. **107,** 116802 (2011).

[46] L. Li, T. Li, S. M. Wang, C. Zhang, and S. N. Zhu, Phys. Rev. Lett. **107**, 126804 (2011).

[47] I. Dolev, I. Epstein, and A. Arie, Phys. Rev. Lett. **109,** 203903 (2012).

[48] I. Epstein and A. Arie, Phys. Rev. Lett. **112,** 023903 (2014).

[49] Palik, E. D., *Handbook of optical constants of solids* (San Diego, Academic Press, 1998).

[50] A. S. Weling, B. B. Hu, N. M. Froberg, and D. H. Auston, App. Phys. Lett **64**, 137 (1994).

[51] A. Nahata, A. S. Weling, and T. F. Heinz, Appl. Phys. Lett. **69**, 2321 (1996).

[52] D. H. Auston and M. C. Nuss, IEEE Journ. Quant. Elec. **24**, 184 (1988).

[53] Lee, Yun-Shik, *Principles of Terahertz Science and Technology* (Springer, New York, 2009).

[54] A. Dreyhaupt, S. Winnerl, M. Helm, and T. Dekorsy, Opt. Lett. **31**, 1546 (2006).

[55] Boyd, R. W. *Nonlinear Optics*, 3rd ed. (Academic Press, San Diego, 2008).

[56] Q. Wu and X.-C. Zhang, Appl. Phys. Lett. **70**, 1784 (1997).

[57] C. A. Werley, Q. Wu, K.-H. Lin, C. Ryan Tait, A. Dorn, and K. A. Nelson, J. Opt. Soc. Am. B **27**, 2350.

[58] Y. Yan, E. B. Gamble Jr., and K. A. Nelson, J. Chem. Phys. **83,** 5391 (1985).

[59] J. K. Wahlstrand and R. Merlin, Phys. Rev. B **68,** 054301 (2003).

[60] Greg Garrett, Ph.D Thesis, University of Michigan, 2001.

[61] M. Henstridge, Jing Zhou, L. Jay Guo, and R. Merlin, Appl. Phys. Lett. **111**, 063503 (2017).

[62] H. A. Bethe, Phys. Rev. **66**, 163 (1944).

[63] T. W. Ebbesen, H. J. Lezec, H. F. Ghaemi, T. Thio, and P. A. Wolff, Nature, **391**, 667 (1998).

[64] J. A. Porto, F.J. Garcia-Vidal, and J. B. Pendry, Phys. Rev. Lett. **83**, 2845 (1999).

[65] Y. Levitan, IEEE Trans. Micro. Theor. Tech. **36**, 44 (1988).

[66] F. J. Garcia-Vidal, L. Martin-Moreno, T. W. Ebbesen, and L. Kuipers, Rev. Mod. Phys. **82**, 729 (2010).

[67] Steven M. Young, Ph.D Thesis, University of Michigan, 2006.

[68] R. Merlin, Phys. Rev. X **2**, 031015 (2012).

[69] S. M. Young, C. Pfeiffer, A. Grbic, and R. Merlin, App. Phys. Lett. **103**, 041104 (2013).

[70] H. Barkhuijsen, R. de Beer, W. M. M. J. Bovée, and D. van Ormondt, J. Magn. Reson. **61**, 465 (1985).

[71] F. W. Wise, M. J. Rosker, G. L. Millhauser, and C. L. Tang, IEEE J. Quantum Electron. **QE-23**, 1116 (1987).

[72] M. Henstridge, C. Pfeiffer, D. Wang, A. Boltasseva, V. Shalaev, A. Grbic, and R. Merlin, arXiv:1803.01769 [physics.optics] (6 March 2018). Also accepted for publication in *Optica*.

[73] P. Zhang, Y. Hu, D. Cannan, A. Salandrino, T. Li, R. Morandotti, X. Zhang, and Z. Chen, Opt. Lett. **37**, 2820 (2012).

[74] G. A. Siviloglou and D. N. Christodoulides, Opt. Lett. **32**, 979 (2007).

[75] G. A. Siviloglou, J. Broky, A. Dogariu, and D. N. Christodoulides, Phys. Rev. Lett. **99**, 213901 (2007).

[76] I. Kaminer, R. Bekenstein, J. Nemirovsky, and M. Segev, Phys. Rev. Lett. **108,** 163901 (2012).

[77] P. Zhang, Y. Hu, T. Li, D. Cannan, X. Yin, R. Morandotti, Z. Chen, and X. Zhang, Phys. Rev. Lett. **109**, 193901 (2012).

[78] L. Froehly, F. Courvoisier, A. Mathis, M. Jacquot, L. Furfaro, R. Giust, P. A. Lacourt, and J. M. Dudley, Opt. Express **19**, 16455 (2011).

[79] F. Courvoisier, A. Mathis, L. Froehly, R. Giust, L. Furfaro, P. A. Lacourt, M. Jacquot, and J. M. Dudley, Opt. Lett. **37**, 1736 (2012).

[80] A. Mathis, F. Courvoisier, R. Giust, L. Furfaro, M. Jacquot, L. Froehly, and J. M. Dudley, Opt. Lett. **38**, 2218 (2013).

[81] E. Greenfield, M. Segev, W. Walasik, and O. Raz, Phys. Rev. Lett. **106** 213902 (2011).

[82] D. G. Papazoglou, S. Suntsov, D. Abdollahpour, and S. Tzortzakis, Phys. Rev. A **81**, 061807(R) (2010).

[83] A. Grbic, L. Jiang, R. Merlin, Science **320,** 511 (2008).

[84] G. Li, S. Chen, N. Pholchai, B. Reineke, P. Wing Han Wong, E. Yue Bun Pun, K. Wai Cheah, T. Zentgraf, and S. Zhang, Nature **14**, 607 (2015).

[85] Y. Yang, W. Wang, A. Boulesbaa, I. I. Kravchenko, D. P. Briggs, A. Puretzky, D. Geohegan, and J. Valentin, Nano Lett. **15**, 7388 (2015).

[86] J. Lee, M. Tymchenko, C. Argyropoulos, P. Chen, F. Lu, F. Demmerle, G. Boehm, M. Amann, A. Alù, and M. A. Belkin, Nature **511**, 65 (2014).

[87] G. Zheng, H. Mühlenbernd, M. Kenney, G. Li, T. Zentgraf, and S. Zhang, Nat. Nano. **10**, 308 (2015).

[88] X. Ni, A. V. Kildishev, and V. M. Shalaev, Nat. Comm. **4**, 2807 (2013).

[89] X. Ni, Z. J. Wong, M. Mrejen, Y. Wang, and X. Zhang, Science **349**, 1310 (2015).

[90] N. Yu, P. Genevet, M. A. Kats, F. Aieta, J. Tetienne, F. Capasso, and Z. Gaburro, Science **334**, 333 (2011).

[91] X. Ni, N. K. Emani, A. V. Kildishev, A. Boltasseva, and Vladimir M. Shalaev, Science **335**, 427 (2012).

[92] M. Khorasaninejad, F. Aieta, P. Kanhaiya, M. A. Kats, P. Genevet, D. Rousso, and F. Capasso, Nano Lett. **15**, 5358 (2015).

[93] M. Khorasaninejad, W. T. Chen, R. C. Devlin, J. Oh, A. Y. Zhu, and F. Capasso, Science **352**, 1190 (2016).

[94] L. Novotny, Phys. Rev. Lett. **98**, 266802 (2007).

[95] D. M. Pozar, S. D. Targonski, and H. D. Syrigos, IEEE Trans. Antennas Propag. **45,** 287 (1997).

[96] M. Henstridge, C. Pfeiffer, D. Wang, A. Boltasseva, V. Shalaev, A. Grbic, and R. Merlin, "Synchrotron Radiation from an Accelerating Light Pulse," submitted for publication.

[97] F. R. Elder, A. M. Gurewitsch, R. V. Langmuir, H. C. Pollock, Phys. Rev. **71**, 829 (1947).

[98] D. Iwanenko and I. Pomeranchuk, Phys. Rev. **65**, 343 (1944).

[99] J. P. Blewett, Phys. Rev. **69**, 87 (1945).

[100] J. P. Blewett, J. Synchrotron Rad. **5,** 135 (1998).

[101] T. Mass, A. J. Giuffre, Chang-Yu Sun, C. A. Stifler, M. J. Frazier, M. Neder, N. Tamura, C. V. Stan, M. A. Marcus, and P. U. P. A. Gilbert, Proc. Natl. Acac. Sci. **114**, E7670 (2017).

[102] A. N. Kravchenko , W. C. Negassa, A. K. Guber, B. Hildebrandt, T. L. Marsh, M. L. Rivers, Soil Sci. Soc. Am. J. **78**, 1924 (2014)

[103] S. Kumar, J. P. Strachan, A. L. D. Kilcoyne, T. Tyliszczak, M. D. Pickett, C. Santori, G. Gibson, R. S. Williams, Appl. Phys. Lett. **108**, 073102 (2016);

[104] S. Moser, Y. Nomura, L. Moreschini, G. Gatti, H. Berger, P. Bugnon, A. Magrez, C. Jozwiak, A. Bostwick, E. Rotenberg, S. Biermann, M. Grioni, Phys. Rev. Lett. **118**, 176404 (2017).

[105] E. L. Dyer, W. G. Roncal, J. A. Prasad, H. L. Fernandes, D. Gürsoy, V. De Andrade, K. Fezzaa, X. Xiao, J. T. Vogelstein, C. Jacobsen, K. P. Körding, and N. Kasthuri, eNeuro, **4**, .0195-17.2017 (2017).

[106] A. Ardavan, W. Hayes, J. Singleton, H. Ardavan, J. Fopma, and D. Halliday, J. Appl. Phys. **96**, 4614 (2004); 96, 7760(E)(2004).

[107] V. L. Ginzburg, S. I. Syrovatskii, Annual Review of Astronomy and Astrophysics **3**, 297 (1965).

[108] B. M. Bolotovskiĭ, V. P. Bykov, Sov. Phys. Usp. **33,** 477 (1990).

[109] H. Ardavan, Phys. Rev. E **58**, 6659 (1998).

[110] A. S. Barker Jr., A. A. Ballman and J. A. Ditzenberger, Phys. Rev. B **2**, 4233 (1970).

[111] V. P. Zrelov, *Cherenkov Radiation in High-Energy Physics*, (Israel Program for Scientific Translations, Jerusalem, 1970), p. 31.

[112] see e.g. J. D. Jackson, *Classical Electrodynamics* (Wiley, New York, ed. 3, 1999), p. 679.

[113] B. M. Bolotovskiĭ and V. P. Bykov, Sov. Phys. Usp. **33,** 477 (1990) [Usp. Fiz. Nauk **160**, 141 (1990)].

[114] H. Ardavan, Phys. Rev. E **58**, 6659 (1998).

[115] C. Pfeiffer and A. Grbic, Phys. Rev. Lett. **110,** 197401 (2013).

[116] C. Pfeiffer, N. K. Emani, A. M. Shaltout, A. Boltasseva, V. M. Shalaev, and A. Grbic, Nano. Lett. **14**, 2491 (2014).

[117] M. Cai, O. Painter, and K. J. Vahala, Phys. Rev. Lett. **85,** 74 (2000).

[118] S. C. Hagness, D. Rafizadeh, S. T. Ho, and A. Taflove, Journ. Light. Tech. **15**, 2154 (1997).

[119] V. S. Ilchenko, A. A. Savchenkov, A. B. Matsko, and L. Maleki, Phys. Rev. Lett. **92**, 043903 (2004).